

Dissertation zur Erlangung des Doktorgrades
der Fakultät für Chemie und Pharmazie
der Ludwig-Maximilians-Universität München

Horizontal material transfer from healthy to mutant photoreceptors after partial rescue in a retinitis pigmentosa mouse model



Michelle Carmen Jentsch

aus

Heilbronn, Deutschland

2023

Erklärung

Diese Dissertation wurde im Sinne von § 7 der Promotionsordnung vom 28. November 2011 von Frau Prof. Dr. Susanne Friederike Koch betreut.

Eidesstattliche Versicherung

Diese Dissertation wurde eigenständig und ohne unerlaubte Hilfe erarbeitet.

München, den 28.03.2023

M. Jentsch

.....
(Michelle Carmen Jentsch)

Dissertation eingereicht am 28.03.2023

1. Gutachterin: Prof. Dr. Susanne Friederike Koch
2. Gutachter: Prof. Dr. Martin Biel

Mündliche Prüfung am 11.05.2023

Für meine Familie

Table of contents

List of figures	I
List of tables	III
Abbreviations	IV
Summary.....	VII
1 Introduction.....	1
1.1 The mammalian eye	1
1.1.1 Anatomy of the eye	1
1.1.2 Retinal layers.....	2
1.1.3 Photoreceptors	4
1.1.4 Visual phototransduction.....	5
1.1.5 Phosphodiesterase 6	7
1.1.6 Vasculature of the eye.....	7
1.1.7 Retinal pigment epithelium.....	8
1.2 Retinitis pigmentosa.....	10
1.2.1 Genetic alterations	10
1.2.2 Disease progression.....	10
1.2.3 Retinal remodeling.....	12
1.2.4 Current therapies.....	12
1.3 Material transfer in the retina.....	13
1.3.1 Biogenesis and composition of extracellular vesicles	14
1.3.2 Role of extracellular vesicles in retinal health and disease.....	16
1.4 Retinitis pigmentosa mouse models	17
1.4.1 <i>Pde6b</i> ^{STOP/STOP} mouse line as model for retinitis pigmentosa.....	17
1.4.2 Cre-Lox recombination.....	18
1.4.3 <i>Pde6b</i> ^{STOP/STOP} , <i>Pax6aCre</i> , <i>ROSA</i> mouse line.....	19
2 Aim of the thesis	21

3	Material and methods.....	22
3.1	Material	22
3.1.1	Buffers and solutions	22
3.1.2	Chemicals	23
3.1.3	Consumables.....	25
3.1.4	Commercial kits.....	27
3.1.5	Technical devices.....	27
3.2	Biological Systems	28
3.2.1	Cell culture.....	28
3.2.2	Mice	28
3.3	Methods.....	29
3.3.1	Polymerase chain reaction.....	29
3.3.2	Tissue preparation	33
3.3.3	Retinal explants	34
3.3.4	Immunofluorescence.....	35
3.3.5	Fluorescence <i>in situ</i> hybridization.....	37
3.3.6	Immunohistochemistry.....	37
3.3.7	Imaging	38
3.3.8	Quantitative analysis.....	38
3.3.9	Correlative light-electron microscopy	41
3.3.10	Flow cytometry.....	42
3.3.11	Small extracellular vesicles.....	43
3.3.12	Extraction of DNA and RNA.....	45
3.3.13	Quantitative real-time PCR.....	46
3.3.14	Immunoblotting	48
3.3.15	Electroretinogram recordings.....	50

4	Results.....	51
4.1	Effect of healthy rods on neighboring mutant rods after partial rescue.....	51
4.1.1	Depletion of PDE6B in <i>Pde6b</i> ^{ST/ST} mice	51
4.1.2	Mosaic Cre expression under Pax6 α promotor.....	52
4.1.3	Formation of an ONL gradient due to stepwise PDE6B expression in tdTomato-positive photoreceptors.....	54
4.1.4	Stepwise Pde6b RNA expression in tdTomato-positive photoreceptors	58
4.1.5	Postnatal absence of Pax6 α Cre recombinase in photoreceptors	60
4.1.6	Indications for genetic heterogeneity of <i>Pde6b</i> after partial rescue	64
4.2	Effect of partial rescue on retinal remodeling.....	65
4.2.1	Restoration of visual function after partial rescue	65
4.2.2	Partial preservation of central bipolar and horizontal cell dendrites after partial rescue.....	67
4.2.3	Partial rescue of photoreceptors prevents blood vessel remodeling	69
4.2.4	Rescue of peripheral photoreceptors prevents overall RPE remodeling.....	74
4.3	Horizontal material transfer via small EVs.....	78
4.3.1	Characterization of isolated small EVs	78
4.3.2	Indications for transport of PDE6B protein, RNA and DNA.....	80
4.3.3	Small EV-mediated transfer could not be confirmed.....	83
5	Discussion.....	86
5.1	Successful non-invasive rescue of RP mice	86
5.2	Possibility of low-level postnatal Cre expression	88
5.3	Potential ongoing central vasculature remodeling after partial rescue.....	89
5.4	Crucial role of the RPE in retinal rescue	90
5.5	Small EVs as most likely mediator of horizontal material transport.....	91
6	References	94
7	Publication	110
8	Acknowledgements	111

List of figures

Figure 1: Anatomy of the eye in human and mice.....	2
Figure 2: Composition of the multilayered retina with Bruch's membrane and choroid.....	3
Figure 3: Photoreceptor composition and cone distribution	5
Figure 4: Visual phototransduction cascade under dark and light condition	6
Figure 5: Functions of the RPE	9
Figure 6: Fundus and vision during progression of retinitis pigmentosa.....	11
Figure 7: Biogenesis of extracellular vesicles and exosome composition.....	15
Figure 8: <i>Pde6b^{STOP}</i> mice as model for retinitis pigmentosa	18
Figure 9: Partial rescue by expression of <i>Pax6αCre</i>	20
Figure 10: Preparation of the eye	33
Figure 11: Schematic representation of cell eccentricity and solidity	40
Figure 12: FACS gating strategy using the negative control.....	43
Figure 13: Isolation of small EVs.....	44
Figure 14: ERG recording and response	50
Figure 15: Loss of PDE6B results in progressive photoreceptor degeneration in <i>Pde6b^{ST/ST}</i> mice	52
Figure 16: Expression of Cre recombinase in the temporal and nasal periphery of <i>Pde6b^{ST/ST} Pax6αCre ROSA^{nT-nG}</i> mice	53
Figure 17: Stepwise PDE6B expression in tdTomato-positive photoreceptors.....	55
Figure 18: PDE6B expression in tdTomato-positive photoreceptors is more elevated in 48-week-old mice.....	56
Figure 19: Progression of a gradient in the outer nuclear layer thickness and cone length.....	58
Figure 20: Stepwise expression of <i>Pde6b</i> RNA in tdTomato-positive photoreceptors.....	59
Figure 21: <i>Pde6b</i> RNA in FAC-sorted tdTomato and PDE6B double-positive photoreceptors	60
Figure 22: Absence of <i>Pax6αCre</i> recombinase protein in adult mice.....	61
Figure 23: Absence of <i>Pax6αCre</i> recombinase RNA in the outer nuclear layer	62
Figure 24: Absence of <i>Pax6αCre</i> recombinase RNA in FAC-sorted cells	63
Figure 25: Genetic heterogeneity of <i>Pde6b</i> in FAC-sorted cells	64
Figure 26: Partial rescue of scotopic and mesopic retinal function in <i>Pde6b^{ST/ST} Pax6αCre</i> mice	66
Figure 27: Rescue of photopic retinal function in <i>Pde6b^{ST/ST} Pax6αCre</i> mice	67
Figure 28: Partial preservation of central bipolar and horizontal cell dendrites.....	68

Figure 29: Rescue of morphological abnormalities in the deep and intermediate vascular plexi	70
Figure 30: Rescue of morphological abnormalities in the superficial vascular plexus	71
Figure 31: Rescue of acellular capillaries in <i>Pde6b^{ST/ST} Pax6αCre</i> mice	73
Figure 32: RPE of <i>Pde6b^{ST/ST}</i> mice demonstrate four morphological regions	74
Figure 33: RPE cells from <i>Pde6b^{ST/ST}</i> mice do not show onset of mitosis but disrupted cytoskeleton	75
Figure 34: Rescue of morphological abnormalities in the RPE	77
Figure 35: Nanoparticle tracking analysis and immunoblotting of isolated small EVs.....	79
Figure 36: Light-electron microscopy of immunogold-labeled PDE6B in EVs	80
Figure 37: Pde6b RNA in isolated small EVs	81
Figure 38: <i>Pde6b</i> DNA in isolated small EVs	82
Figure 39: 661W cells show uptake of isolated small EVs but no PDE6B expression	84
Figure 40: Absence of Pde6b RNA in retinal explants.....	85

List of tables

Table 1: Composition of utilized buffers and solutions	22
Table 2: Utilized chemicals and reagents.....	23
Table 3: Utilized consumables.....	25
Table 4: Utilized commercial kits.....	27
Table 5: Utilized devices and belonging software.....	27
Table 6: MasterMix components for genotyping in μ l.....	29
Table 7: Utilized genotyping primers in 100 μ M stock, all ordered from Metabion.....	30
Table 8: Thermocycling conditions for amplification of <i>Pde6b</i> ^{STOP}	30
Table 9: Thermocycling conditions for amplification of <i>Pax6αCre</i>	31
Table 10: Thermocycling conditions for amplification of <i>ROSA</i> ^{nT-nG}	31
Table 11: Thermocycling conditions for amplification of <i>ROSA</i> ^{mT-mG}	31
Table 12: Thermocycling conditions for amplification of <i>Pde6g</i> ^{CreERT2}	32
Table 13: Thermocycling conditions for amplification of <i>RhoCre</i>	32
Table 14: Sizes of PCR products in bp.....	32
Table 15: Retinal explant media.....	34
Table 16: Immunofluorescence primary antibodies and lectins	36
Table 17: Immunofluorescence secondary antibodies	36
Table 18: H&E staining procedure	38
Table 19: Number of replicates for retinal section and flatmount quantifications.....	39
Table 20: Number of replicates for vasculature and RPE quantifications.....	40
Table 21: MasterMix for one RT-PCR reaction.....	46
Table 22: Settings for RT-PCR run.....	46
Table 23: MasterMix for one qRT-PCR reaction	47
Table 24: Utilized qPCR primers in 100 μ M stock, all ordered from Metabion	47
Table 25: Settings for qRT-PCR run	48
Table 26: Western Blot primary antibodies	49
Table 27: Western Blot secondary antibodies.....	49

Abbreviations

AF	Alexa Fluor
ALIX	Apoptosis-linked gene 2 interacting protein X
ANOVA	Analysis of variance
APS	Ammonium persulfate
ATP	Adenosine triphosphate
bp	Base pair
BSA	Bovine serum albumin
CAR	Cone arrestin
cDNA	Complementary deoxyribonucleic acid
CDS	Coding sequence
cGMP	Cyclic guanosine monophosphate
CLEM	Correlative light-electron microscopy
CNG	Cyclic nucleotide-gated
CNS	Central nervous system
ddH ₂ O	Double-distilled water
DMSO	Dimethyl sulfoxide
dNTP	Deoxyribose nucleoside triphosphate
DPBS	Dulbecco's PBS
DVP	Deep vascular plexus
ECM	Extracellular matrix
EDTA	Ethylenediamine tetraacetic acid
EGFP	Enhanced green fluorescent protein
EMT	Epithelial-mesenchymal transition
ER	Endoplasmatic reticulum
ERG	Electroretinogram
ESCRT	Endosomal sorting complex required for transport
EV	Extracellular vesicle
EZL	Extracellular solution
FACS	Fluorescence-activated cell sorting
FBS	Fetal bovine serum
FSC	Forward scatter
GARP	Glutamic-acid-rich protein

GCL	Ganglion cell layer
GDP	Guanosine diphosphate
GFAP	Glial fibrillary acidic protein
GTP	Guanosine triphosphate
H&E	Hematoxylin and eosin
HEPES	Hydroxyethyl-piperazineethanesulfonic acid
HRP	Horseradish peroxidase
i.p.	Intraperitoneal
ILM	Inner limiting membrane
INL	Inner nuclear layer
IPL	Inner plexiform layer
IS	Inner segment
IVP	Intermediate vascular plexus
<i>LoxP</i>	Locus of x-over P1
MEA	Multielectrode array
MVB	Multivesicular body
NTA	Nanoparticle tracking analysis
ON	Optic nerve
ONL	Outer nuclear layer
OPL	Outer plexiform layer
OS	Outer segment
P	Postnatal day
Pax6	Paired box 6
PB	Phosphate buffe
PBS	Phosphate buffered saline
PCR	Polymerase chain reaction
PDE	Phosphodiesterase
PEDF	Pigment epithelium-derived factor
Pen/Strep	Penicillin/Streptomycin
PFA	Paraformaldehyde
PKC α	Protein kinase C alpha
pw	Postnatal week
qRT-PCR	Quantitative real-time PCR
RNA	Ribonucleic acid

ROI.....	Region of interest
ROS	Reactive oxygen species
ROSA26.....	Reverse oriented splice acceptor clone 26
RP	Retinitis pigmentosa
RPE	Retinal pigment epithelium
SCGN	Secretagoin
SDS	Sodium dodecyl sulfate
SEM	Standard error of the mean
snRNA	Small nuclear RNA
SSC	Sideward scatter
SVP	Superficial vascular plexus
TAE	Tris-acetate-EDTA buffer
TBST	Tris-buffered saline with Tween-20
TCA	Tricarboxylic acid cycle
tdTomato	Tandem dimer Tomato
TEMED	Tetramethylethylenediamine
VEGF	Vascular endothelial growth factor

Summary

Retinitis pigmentosa (RP) is characterized by progressive loss of photoreceptor cells leading to night blindness, tunnel vision and ultimately blindness. While mutant rod photoreceptors are primarily affected, secondary changes in cones, inner retinal cells, retinal vasculature and the retinal pigment epithelium (RPE) have been reported. So far, there is no cure for RP, but therapeutic strategies (e.g. gene therapy or transplantation) are being intensively developed and tested. However, current methods treat only a fraction of diseased cells resulting in a mosaicism of both healthy and mutant rods.

To study the effect of healthy rods on neighboring mutant rods, we used an RP mouse model with deficiency in the beta subunit of the rod-specific phosphodiesterase 6 (*Pde6b*). These mice contain a *LoxP* flanked *STOP* cassette on both alleles (*Pde6b*^{STOP/STOP}) resulting in lack of PDE6B. Partial rescue of *Pde6b* was achieved by *Pax6αCre* recombinase, which recombines *LoxP* sites resulting in PDE6B expression in parts of the retinal periphery. To visualize *Pax6αCre* recombinase activity, *Pde6b*^{STOP/STOP} *Pax6αCre* mice were crossed with two-color fluorescent reporter mice. These reporter mice express EGFP in Cre-recombined cells and tdTomato in non-recombined cells. Using this approach, we generated retinas with zones of EGFP-positive, Cre-recombined (“healthy”) rods in the periphery and tdTomato-positive, non-recombined (“mutant”) rods in the center.

After partial PDE6B rescue by *Pax6αCre* in the EGFP-positive periphery, rod degeneration was successfully prevented in this region. On the other hand, in the tdTomato-positive center, PDE6B expression was absent leading to progressive degeneration of rods. Interestingly, with disease progression, we observed stepwise PDE6B expression in tdTomato-positive rods bordering the EGFP-positive zone. As a result, the outer nuclear layer, which contains the photoreceptor nuclei, was graded in its thickness from periphery to center. Since Cre protein and Cre RNA were absent in adult photoreceptors, the PDE6B expression in tdTomato-positive rods appears to be due to *Pde6b* transfer from healthy to mutant photoreceptors. To evaluate this possibility, small extracellular vesicles (EVs) were isolated and characterized. We found that EVs from partially treated retinas contained *Pde6b* RNA. Next, we demonstrated that remodeling of inner retina, RPE and retinal vasculature was partially prevented in the central region, suggesting that these structures were positively impacted by healthy rods in the periphery. Importantly, the function of partially rescued retinas was almost normal.

Taken together, these data highlight the cellular communication and interaction between healthy and mutant rods, with positive consequences for retinal homeostasis and function.

1 Introduction

1.1 The mammalian eye

Eyes are the sensory organs of the visual system, which enable organisms their sense of sight. They detect light, convert it into electrical signals and send it to the visual cortex of the brain [1].

1.1.1 Anatomy of the eye

When light enters the eye, it first passes through the protective cornea and the lens, which collect the light and focus the image via contraction or relaxation of the ciliary body through connected zonule fibers (**Fig. 1**). The iris, which is located between the cornea and the lens, controls the incidence of light by change in diameter and size of the pupil. Together these four structures build the anterior segments of the eye. In the posterior segment of the eye, the light first passes through the vitreous body, which maintains the ocular shape. After, the signal reaches the retina where it is converted, bundled and transmitted via the optic nerve (ON) to the visual cortex of the brain. In this region of the retina, called the optic disc, no light-detecting photoreceptors are present and the corresponding part of the field of vision is invisible. Retinal photoreceptors in the back of the eye are closely connected with the monolayered retinal pigment epithelium (RPE), which has important functions in protection of the retina but also in transport between the retina and the choroidal blood stream underneath. The outmost layer of the eye is the sclera, that helps to maintain and protect the shape of eyeball [1–3]. On the sclera, the *ora serrata* marks the transition from the non-photosensitive anterior segments to the retina [4].

Compared to humans (**Fig. 1** left), mouse eyes (**Fig. 1** right) share most anatomical characteristics although a few differences can be observed as they are nocturnal animals with accordingly developed eyes. The most prominent difference is the proportional larger lens and subsequent smaller vitreous body enabling mice to focus a wider field of view. In addition, mouse eyes lack the oval-shaped pigmented area in the center of the retina called macula and the *fovea centralis* therein, which is responsible for sharp central vision in humans due to closely packed cones, while rods are completely absent. Moreover, humans have three different cone opsins whereas mice lack red-light detecting L-opsins [5]. Since the retinal functional features of human and mouse eyes are very much alike, mice are suitable animals to study pathologies of eye diseases and subsequent treatment *in vivo*.

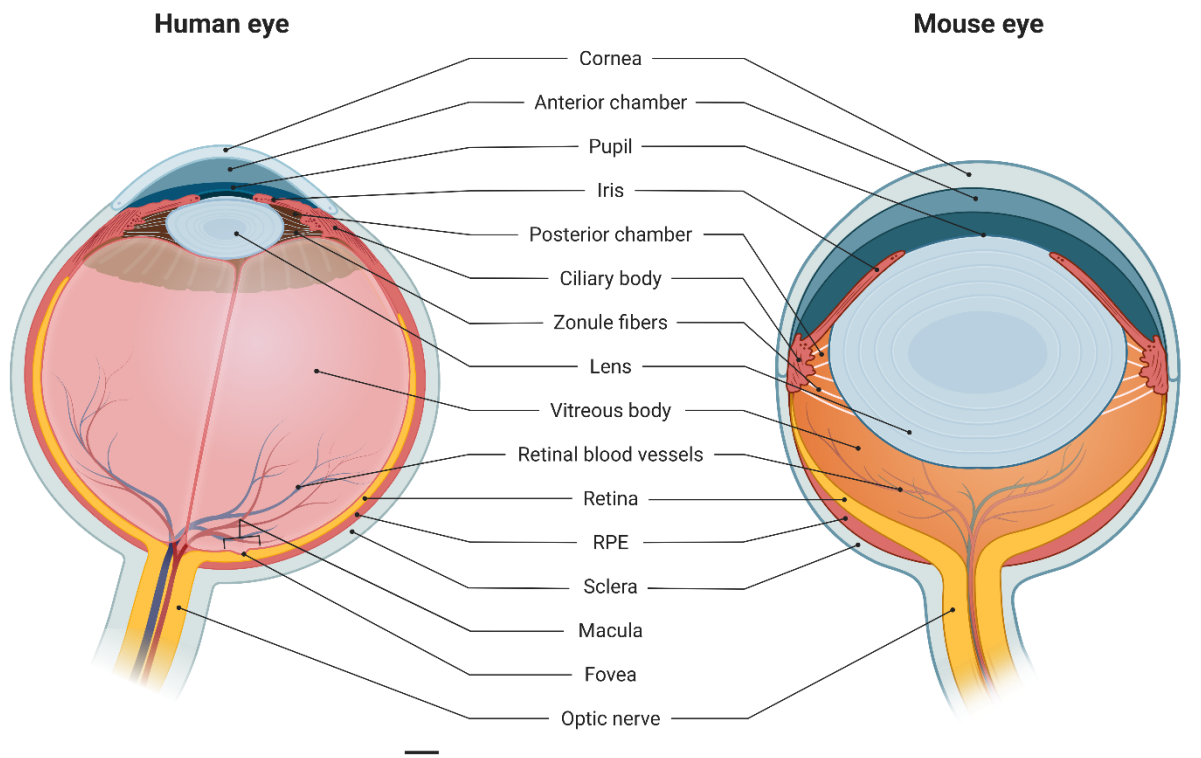


Figure 1: Anatomy of the eye in human and mice.

The human (left) and mouse (right) eye present a similar anatomic structure. The most prominent difference is the proportional larger lens and subsequent smaller vitreous body as well as the missing macula in mice. Scale bars, 2 mm. Created with BioRender.com

1.1.2 Retinal layers

The neural retina is a 100-300 μm thick tissue, which consists of three nuclear layers of densely packed nuclei and two plexiform layers containing synapses and dendrites (**Fig. 2**). Photoreceptor cell bodies form the outer nuclear layer (ONL), the following inner nuclear layer (INL) contains nuclei of bipolar, horizontal, amacrine and Müller cells, while ganglion cell nuclei are located in the ganglion cell layer (GCL) [6].

Incoming light first passes the whole retina until it reaches the outer segments (OS) of rod and cone photoreceptors, where the phototransduction cascade takes place. The signal is then bundled through rod and cone bipolar cells, whose dendrites are connected with photoreceptor synapses in the outer plexiform layer (OPL). After, it is forwarded to the ganglion cells, whose dendrites are located in the inner plexiform layer (IPL) connected to bipolar cell synapses. The axons of ganglion cells merge together in the nerve fiber layer to form the optic nerve sending

action potentials to the visual cortex of the brain [7]. In the outer plexiform layer, also the dendrites of horizontal cells are located, which provide inhibitory feedback to rods, cones and bipolar cells [8]. Similarly, dendrites of amacrine cells can be found in the inner plexiform layer, that transfer signals from rod bipolar cells via cone bipolar cells to ganglion cells [9].

In addition, three different types of glial cells, Müller cells, microglia and astrocytes reside in the retina to support neuronal functions. Müller cells span across the entire retina and have a major role in regulating the extracellular environment as well as maintaining the stability of the retina [10]. Microglia are resident immune cells localized in both plexiform layers and play a role in neuronal development and homeostatic functions of the central nervous system (CNS) [11]. Astrocytes, located in the ganglion cell layer, are involved in retinal vascularization and homeostasis. Together with Müller cell end feet, astrocytes form the inner limiting membrane (ILM) separating the retina from the vitreous body [10,12].

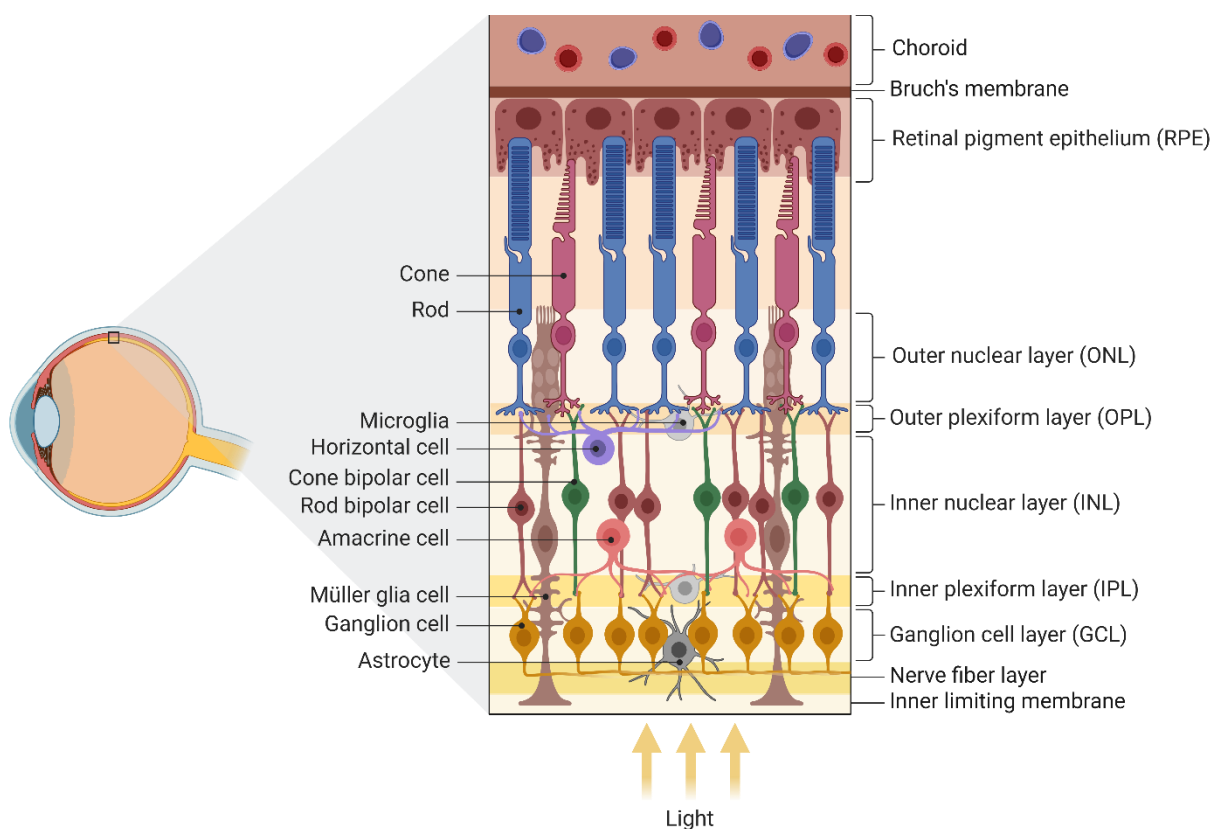


Figure 2: Composition of the multilayered retina with Bruch's membrane and choroid.

Schematic representation of the retina, which is a structured multilayer of the retinal pigment epithelium (RPE), photoreceptors, horizontal cells, bipolar cells, amacrine cells, Müller cells, microglia, astrocytes and ganglion cells. It is located at the inner side of the eyecup. It comprises three layers of cell bodies, the outer nuclear layer (ONL), inner nuclear layer (INL) and ganglion cell layer (GCL), and two layers of synapses and dendrites, the outer plexiform layer (OPL) and inner plexiform layer (IPL). Created with BioRender.com

1.1.3 Photoreceptors

Photoreceptors are characterized by their ability to sense light and convert it into chemical stimuli. There are two types of photoreceptors in the retina, rods and cones, which are mainly distinguished by their light sensitivity [13]. Morphologically, rods and cones are very much alike. They both consist of an outer segment, connecting cilium, inner segment (IS), cell body, axon and synapses (**Fig. 3A**). Structural differences can be found primarily in the outer segments: In rods, the outer segments are significantly longer, have a cylindric shape and comprise internal optic discs, that contain the photopigment rhodopsin for visual phototransduction. In comparison, cone outer segments are shaped conically and their discs, that contain opsin photopigments, are invaginations of the plasma membrane [14].

Rods primarily contribute to night vision (scotopic conditions) as they are very sensitive and can respond to excitation by single photons. Cones, that are stimulated by brighter light (photopic conditions), can be subdivided into short (S), middle (M) and long (L) cones, that differ in their sensitivity to light of different wavelengths (**Fig. 3B**). Under intermediate light (mesopic) conditions, rods and cones are activated simultaneously [15]. In human, S-, M- and L-cones are distributed in a mosaic-like pattern [16]. In mice, different cones are arranged in a gradient from M-cones at the dorsal side via cones that co-express both S- and M-opsins to S-cones residing at the ventral side of the retina [17].

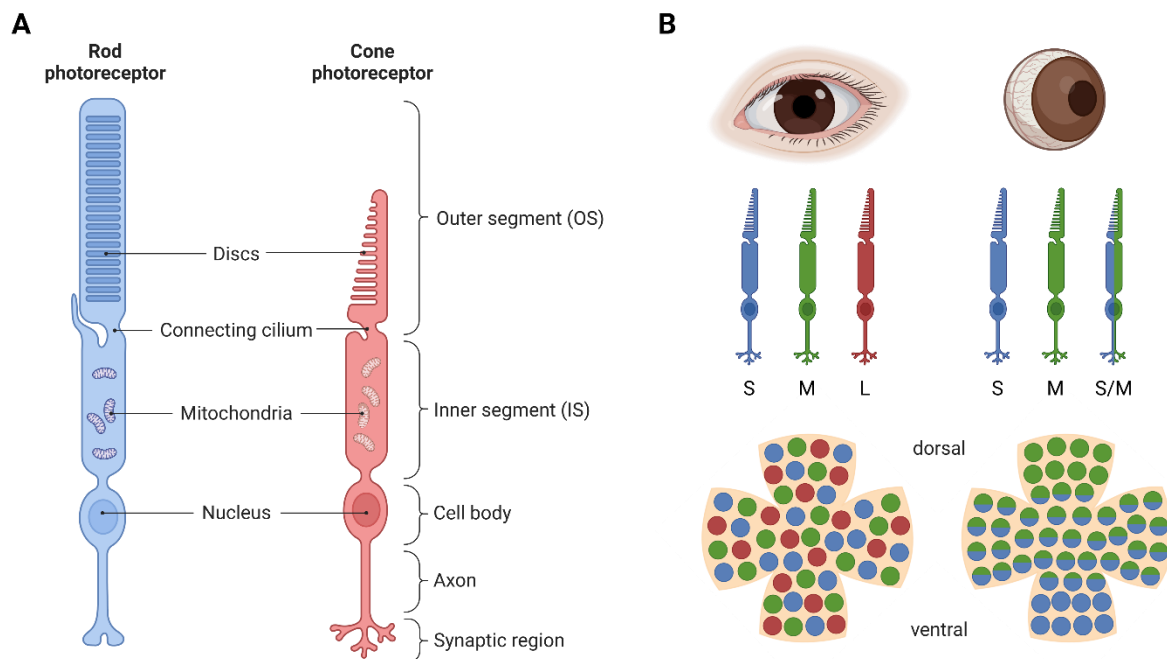


Figure 3: Photoreceptor composition and cone distribution.

(A) Schematic representation of a rod (left) and cone (right) photoreceptor. Both consist of five major structural regions, the outer segment (OS), inner segment (IS), cell body with nucleus, axon, and synaptic region. **(B)** In human (left), S-, M- and L-cones are distributed in a mosaic-like pattern. In mice, cones are arranged in a gradient from M-cones at the dorsal side via S/M-cones to S-cones at the ventral side of the retina. Created with BioRender.com

1.1.4 Visual phototransduction

When light enters the eye, it is converted to electrochemical stimuli by the visual phototransduction cascade, which takes place in the outer segments of rod and cone photoreceptors.

In the dark, intracellular cyclic guanosine monophosphate (cGMP) binds to cyclic nucleotide-gated (CNG) channels, that are located at the outer segment membrane. Consequent channel opening causes a constant influx of sodium and calcium, called the dark current, which leads to depolarization and a membrane potential of -40 mV (**Fig. 4** left). As a consequence, voltage-gated calcium channels open and the intracellular calcium concentration increases [7,18,19]. Calcium then binds to synaptotagmin proteins on the surface of synaptic vesicles, which induces their fusion with the presynaptic membrane and glutamate release [20].

Incoming light is sensed by photopigments, which are G-protein coupled receptors (GPCRs) located at the outer segment discs (**Fig. 4** right). By stimulation with a photon, 11-*cis* retinal isomerizes to all-*trans* retinal and opsin undergoes conformational change to metarhodopsin II. Subsequently, metarhodopsin II binds to the G-protein transducin, causing the replacement of guanosine diphosphate (GDP) with guanosine triphosphate (GTP) at its α -subunit. Consequently, the GTP-bound α -subunit activates phosphodiesterase 6 (PDE6) through dissociation of its regulatory γ -subunit. PDE6 then hydrolyses cGMP to GMP reducing the level of intracellular cGMP causing closure of CNG channels. Following membrane hyperpolarization due to ongoing efflux of potassium ions through non-gated potassium channels then leads to closure of voltage-gated calcium channels. As calcium is required for the fusion of vesicles with the presynaptic membrane, glutamate release drops [7,18,19].

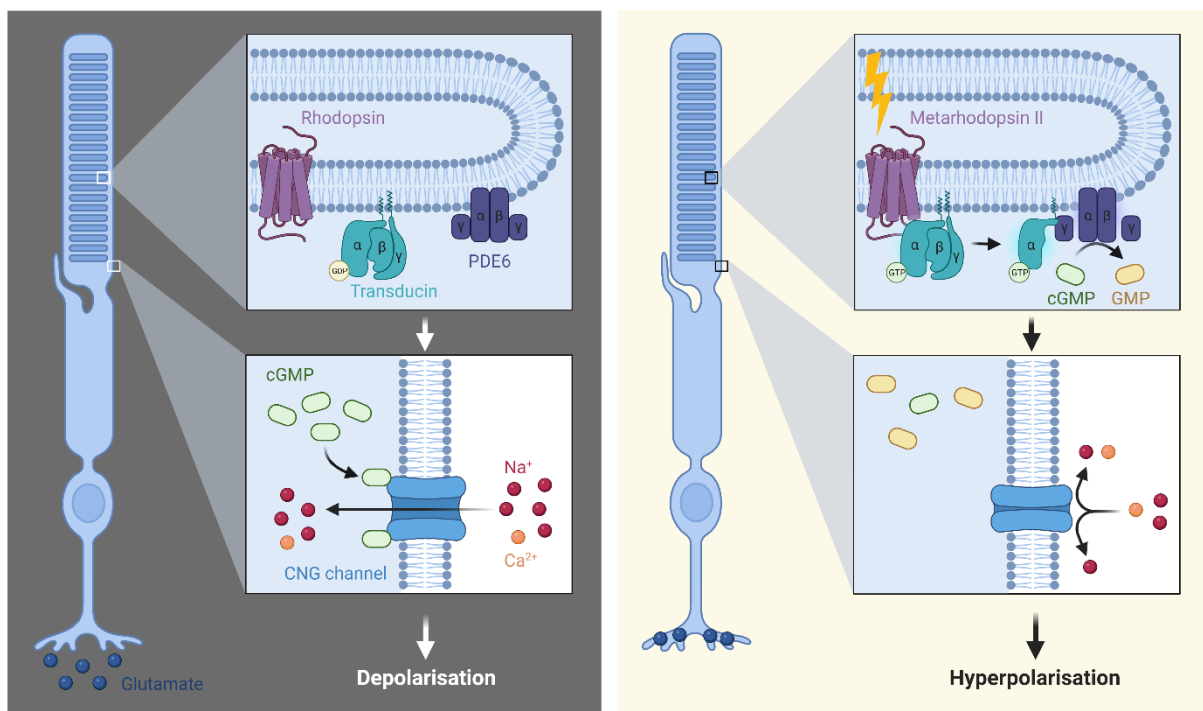


Figure 4: Visual phototransduction cascade under dark and light condition.

Under dark condition (left), rhodopsin, GDP-bound transducin and phosphodiesterase 6 (PDE6), that reside at the disc membrane, are inactive. Cyclic nucleotide-gated (CNG) channels are open resulting in the dark current (depolarization). When light falls in (right), rhodopsin undergoes a conformational change to metarhodopsin II, which activates GTP-bound transducin. The α -subunit of transducin activates PDE6 by removing its inhibitory γ -subunits. PDE6 then degrades cGMP to GMP causing closure of CNG channels and hyperpolarization. Created with BioRender.com

Chemical stimuli are then transmitted to the dendrites of downstream second-order neurons in the outer plexiform layer. Cone bipolar cells can be divided into ON and OFF subtypes, that get hyperpolarized and depolarized respectively, in response to decreased glutamate release. ON bipolar cell synapses are then in contact with ON ganglion cells in the inner half and OFF bipolar cell synapses with OFF ganglion cells in the outer half of the IPL. On the other hand, rod bipolar cells are all ON types. In contrast to cone bipolar cells, they send their signals not directly to the ganglion cells but via amacrine and cone bipolar cells [9,21,22].

1.1.5 Phosphodiesterase 6

PDE6 plays a crucial role in the visual phototransduction cascade of both rods and cones. It is a heterotetrameric enzyme, which is anchored to the disc membrane through interactions with other proteins such as the rod outer segment membrane protein 1 (ROM1) in rods.

Two catalytic subunits are responsible for hydrolyzing cGMP to GMP. Through binding to them, inhibitory PDE6 subunits regulate the enzymatic activity by preventing their interaction with cGMP. In rods, PDE6 contains an α - and β - catalytic subunit and two inhibitory γ -subunits. Cones express PDE6H instead of PDE6G, which has a similar inhibitory function. In addition, they comprise two catalytic α -subunits and lack the β -subunit [19,23,24].

1.1.6 Vasculature of the eye

The retina is supplied by two blood circulations. On the one hand, the choroid capillaries provide nutrients via transport through the RPE [25–27]. On the other hand, the inner retina contains three layers of interconnected blood vessels. The first one is the superficial vascular plexus (SVP) composed of larger arteries, arterioles, capillaries, venules, and veins, that primarily lie in the ganglion cell layer and partly in the inner plexiform layer. It derives from the central retinal artery in conjunction with the optic nerve and is characterized by a centripetally branching pattern. The SVP then branches into the intermediate vascular plexus (IVP), that contains mainly capillaries at the IPL/INL interface. The third layer is the deep vascular plexus (DVP), which lies in between the inner nuclear layer and outer plexiform layer. As the IVP, it is interconnected by vertically oriented vessels and consists of small capillaries. In contrast to the SVP, the IVP and DVP are arranged in winding patterns of uniform sized vessels without directional preference [26,28,29].

Unlike the fenestrated choroidal capillaries, retinal blood vessels consist of non-fenestrated endothelial cells, that form the inner blood-retinal barrier to mediate highly selective transport of molecules. Furthermore, responses to changes in tissue oxygen levels as well as metabolic needs of the retina are autoregulated by the retinal vasculature, while the choroid supply is under neurogenic control [25,26].

1.1.7 Retinal pigment epithelium

The RPE is a monolayer of penta- to hexagonal shaped cells, that contain densely packed pigment granules. It is located in between the photoreceptors and the Bruch's membrane, the innermost layer of the choroid vasculature. The RPE has a strong apical to basal polarization and fulfills several functions in maintaining the homeostasis of the retina (**Fig. 5**) [27,30].

On their apical side, the surface area of RPE cells is increased by microvilli, that are closely connected to photoreceptor outer segments, which enables efficient epithelial trafficking [27,30]. During visual phototransduction, all-*trans* retinal is transported into the RPE where it is reduced to all-*trans*-retinol, re-isomerized to 11-*cis*-retinal and is then returned to the outer segments [31]. In addition, the RPE plays an important role in the blood-retinal barrier, that facilitates the highly selective transport of metabolites, ions, oxygen and water between the choroid and the retina. Especially transport of glucose is essential for retinal metabolism, as it serves as source of energy. Glycolysis in photoreceptors is used for lipid biosynthesis and produced lactate is further secreted to inner nuclear cells or returned to the RPE [32,33]. Another important function of the RPE is the phagocytosis and digestion of photoreceptor outer segments, that are constantly renewed by shedding their tips. Thereby, dismantled fatty acids get transported back to photoreceptors and serve for adenosine triphosphate (ATP) production in the mitochondrial tricarboxylic acid cycle (TCA) [34]. As RPE cells contain melanosome pigments, they are able to absorb scattered light and thus protect the tissue from photo-oxidative stress. Furthermore, the RPE secretes various factors and signaling molecules, such as growth factors, in order to communicate with photoreceptors and the choroid [27].

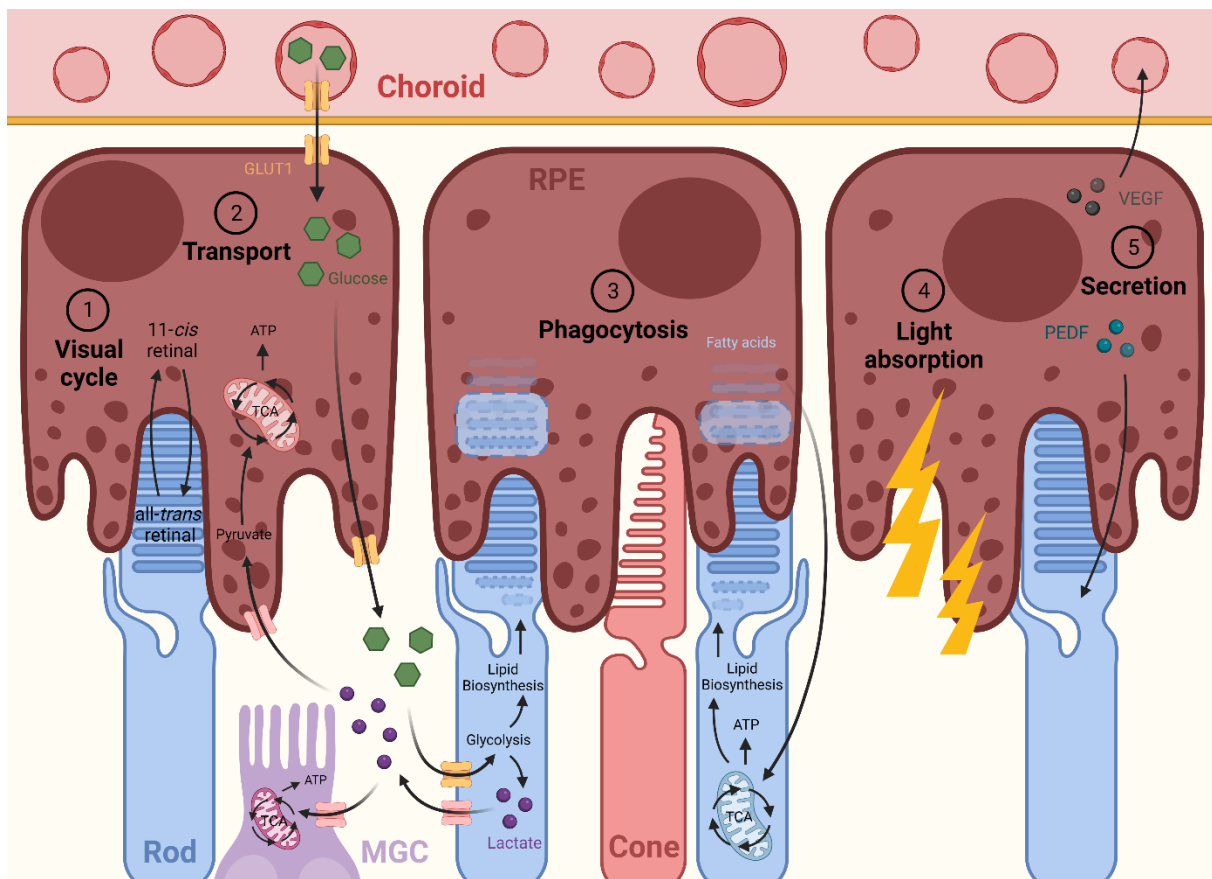


Figure 5: Functions of the RPE.

Retinal pigment epithelium (RPE) cells are in close contact with photoreceptor outer segments and show various interconnected functions. First, during the visual cycle all-*trans* retinal is transported into the RPE where it is re-isomerized to 11-*cis*-retinal and then returned to the outer segments. Second, the RPE is responsible for the highly selective transport of metabolites, ions, oxygen, and water between the choroid and the retina. Especially glucose, which is metabolized to lactate by photoreceptors, is very important for energy supply of the retina, particularly for Müller glia cells (MGCs). Third, the RPE phagocytoses photoreceptor outer segments, that are constantly renewed. Fourth, RPE pigments absorb scattered light to protect the tissue from photo-oxidative stress. Fifth, the RPE secretes various molecules like growth factors, e.g. vascular endothelial growth factor (VEGF) or pigment epithelium-derived factor (PEDF). Created with BioRender.com

1.2 Retinitis pigmentosa

Retinitis pigmentosa (RP) is a group of genetic disorders, that causes loss of vision. With a prevalence of approximately 1:4,000 it is the most common inherited retinal dystrophy [35]. RP is characterized by pigment deposits in the retina and progressive loss of photoreceptors leading to night blindness and tunnel vision [36].

1.2.1 Genetic alterations

Symptoms of RP patients are caused by loss of photoreceptors due to genetic mutations in rod- or RPE-specific genes. As a consequence, rods start to undergo cell death in the retinal periphery followed by secondary cone degeneration [37]. So far, more than 3,100 mutations in 80 genes have been identified leading to this phenotype in non-syndromic RP, that is not associated with symptoms [35,38]. Depending on the genetic alterations, RP is inherited as autosomal recessive (50-60%), autosomal dominant (30-40%) or X-linked (5-15%) disease [39,40]. At least 29 genes are known to cause syndromic RP, that is accompanied with symptoms affecting other parts of the body, such as hearing loss in Usher syndrome [36,37].

Some genetic mutations occur with a higher prevalence than others. However, 2-5% of autosomal recessive RP patients, that constitute only 1% of all cases, carry alterations in PDE6A, PDE6B, eyes shut homolog (EYS) or RPE65 [38]. On the other hand, some mutations are rare. For instance, only few patients are known to carry a mutation in the PDE6G gene coding for the rod-specific regulatory γ -subunit of the PDE6 enzyme [41].

1.2.2 Disease progression

The evolvement of RP symptoms usually proceeds over several decades. The first indications can appear in the first years of life or only after two decades. Some patients go through rapid evolution of the disease, that takes over two decades, while others experience a slow progression and never experience blindness.

In early stages, mild night blindness occurs due to loss of rods in the peripheral visual field. However, there is almost no effect during daylight as cones are still functional. As a consequence, these symptoms are often ignored or stay unnoticed. In this phase, fundus examination seems to be normal since pigment deposits are not present yet and the attenuation of retinal arterioles is

only modest (**Fig. 6** early stage). On the other hand, electroretinogram (ERG) measurements often already show a decreased b-wave amplitude under scotopic conditions.

In the mid stage, night blindness is complete and restricts the life of patients under low light or dark conditions. In addition, peripheral vision during daylight is restricted, also referred to as tunnel vision (**Fig. 6** mid stage). Using fundoscopy, blood vessel narrowing, retinal degeneration and pigment deposits in the equatorial region, caused by the rupture of the underlying RPE cells, can be revealed. Moreover, ERG measurements show no recordings under scotopic conditions, while cone responses are significantly decreased.

In the late stage, patients lose their entire peripheral vision, that eventually leads to complete blindness (**Fig. 6** late stage). Fundus examination exposes widespread pigment deposits, that might even reach the macula, and retinal blood vessels became very thin. Furthermore, ERG measurements show no recordings for cone responses anymore [36,37].

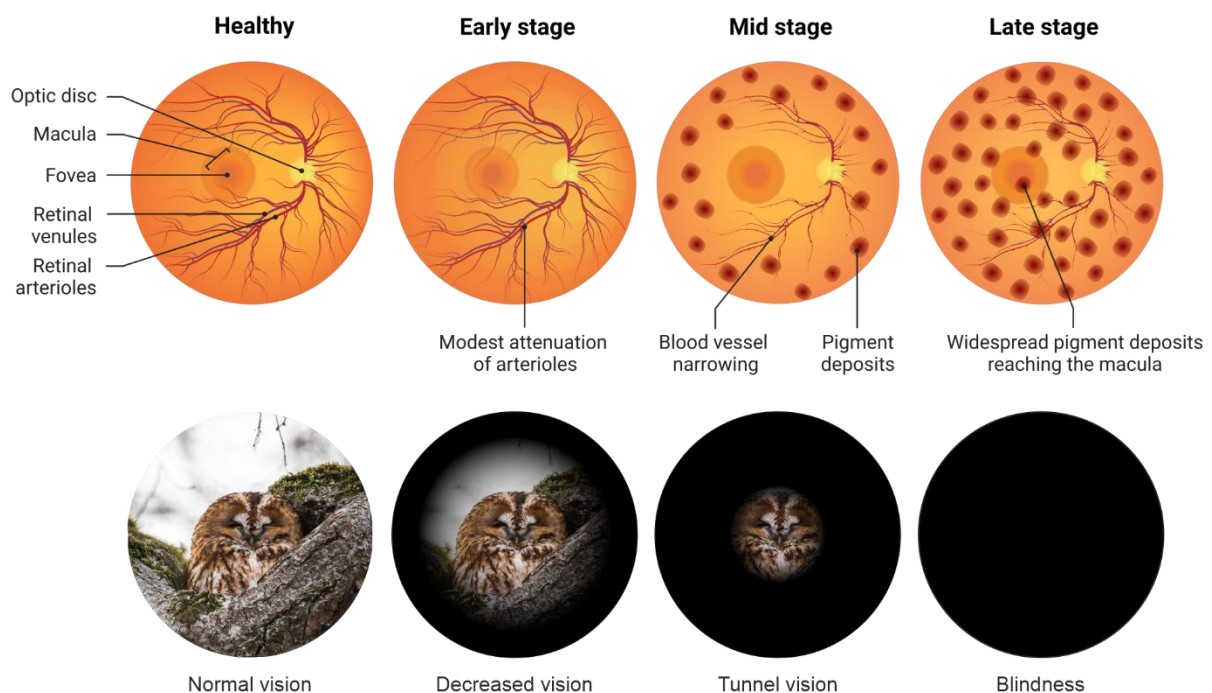


Figure 6: Fundus and vision during progression of retinitis pigmentosa.

In early stages of RP, fundoscopy reveals modest attenuation of retinal arterioles accompanied with mild night blindness. In mid stages, severe blood vessel narrowing and peripheral pigment deposits are recorded together with tunnel vision by restriction of the peripheral field. In late stages, vessels became very thin and pigment deposits are present all over the retina, which eventually leads to complete blindness. Partly created with BioRender.com

1.2.3 Retinal remodeling

Due to photoreceptor loss in RP, a series of progressive events called remodeling gets triggered, which might also impact the success of applied therapies. Retinal remodeling can be divided into three phases. In phase 1, which is the pre-degeneration period, mainly photoreceptors themselves are being remodeled as outer segments become shorter and sprouting of synaptic terminals, extending as far as the ganglion cell layer, occurs. In addition, inner nuclear cells, such as rod bipolar cells, retract and extend their dendrites into the inner plexiform layer. Phase 2 then describes the period of photoreceptor cell death, although some small clusters of cones may survive. It is mainly characterized by the formation of a distal fibrotic glial seal composed of Müller cell processes, that separates the retina from the RPE. Furthermore, microglia start to branch into the outer nuclear layer. Finally, phase 3 depicts neuronal remodeling. After photoreceptor degeneration, all other retinal cells become vulnerable to cell death. Inner nuclear cells lose their connecting dendrites and develop new processes, so called microneuromas, into the inner nuclear layer. Moreover, RPE cells show morphological alterations by loss of their characteristic size and shape. Besides, RPE cells can migrate into the inner retina, often accompanied by choroidal vessels, through gaps in the glial seal [42–46].

Accompanying remodeling of neurons, continuous changes in the vasculature were reported in RP patients. In fact, they exhibit a reduced retinal vessel density with the greatest effect measured in the DVP [47]. Along with retinal vasoconstriction, it has been shown that also the choroid vessels become thinner [48]. In addition, both retinal and choroidal blood flow are decreased [49-51], while retinal venous oxygen saturation is increased [52]. It is hypothesized that these changes may be a consequence of reduced retinal metabolism of nutrients and oxygen due to loss of photoreceptors [53].

1.2.4 Current therapies

So far, there is no cure for RP. However, retinal implants can be used to improve the high contrast visual capacity of patients. Only four devices have currently been approved in Europe. The first one was the Argus II retinal prosthesis system (NCT00407602) [54]. Other devices are the Alpha AMS subretinal implant (NCT02720640), a newer version of the Alpha IMS (NCT01024803) [55,56], and the epiretinal implant IRIS II (NCT02670980).

As loss of photoreceptors cannot be reversed and the retina lacks any regenerative capacity, several clinical approaches are being tested to prevent further degeneration and disease progression. Thereby, adeno-associated virus (AAV) vector-based gene therapy is widely used as these viruses target various cell types and demonstrate a relatively high transduction efficiency. The first approved AAV-based gene therapy for RP is Luxturna, which treats mutations in the RPE65 gene [57]. It has been demonstrated that AAVs are very restricted in their cargo capacity, but novel studies already described a dual AAV strategy [58]. Another gene-independent therapy is the transplantation of retinal cells or precursors into the subretinal space. Transplanted cells have been shown to improve vision but are also accompanied by high immune responses [59]. Both therapies require a morphologically intact retina and thus have a limited time window as they can only be applied efficiently before onset of symptoms or in early stages of RP. In addition, retinal injections are accompanied by various side effects, such as increased inflammation or retinal detachment, and have been shown to act only locally around the injection side [60]. Thus, a high need to optimize therapeutic approaches persists.

1.3 Material transfer in the retina

Various new transplantation experiments are being conducted in order to improve RP therapy. Thereby, human grafts have been associated with the ability to incorporate into recipient mouse retinas [61]. In comparison, it has been shown that most mouse-derived photoreceptors, that were subretinally injected into recipient mice, did not integrate into the adult retina but rather interact via material transfer [62–68]. This phenomenon has been characterized by bi-directional exchange of fluorophores, but also Cre recombinase and other retinal proteins. Following material transfer, an improvement of vision in RP mouse models has already been demonstrated. Further, it has been shown that this transfer does not happen due to cytoplasmic or nuclear fusion events [64–67]. Recent studies proved that both cone and rod precursor transplants undergo exchange with the host retina, while multipotent retinal progenitors or adult photoreceptors do only rarely interact [67,69]. Despite transplantation, transfer of fluorescent markers has also been shown to occur endogenously between cones and neighboring rods via cellular connections [70], although material transfer between rods has not been described yet. Furthermore, it needs to be investigated whether photoreceptors engage in material exchange only among each other. So far, just a few studies have been conducted about transfer to second-order neurons, which showed

low levels of fluorophores in bipolar and Müller cells located next to labeled photoreceptors [64-67].

The underlying mechanism of material transfer in the retina is still not completely understood yet. Some studies showed exchange via cellular connections like nanotubes between grafts and host cells [62,63,65], while others described material transfer between cells located at distant sites without sustained contact [67]. It is also possible that exchange is achieved via extracellular vesicles (EVs), as it has been shown for several cell types, like some neurons and glia cells amongst others [71]. Accordingly, material transfer does not appear to be mediated by the release of free-floating proteins as no uptake has been observed after subretinal injection of recombinant green fluorescent protein (GFP) [67]. Although most publications report exchange of proteins, it has not been clearly defined if also ribonucleic acids (RNA) or even deoxyribonucleic acid (DNA), as it has been shown for cancer cells [72], are transferred and further translated into proteins of interest. Moreover, it also remains unclear if the transfer occurs selectively due to cellular communication or if it is rather random.

1.3.1 Biogenesis and composition of extracellular vesicles

Extracellular vesicles have been shown to play an important role in homeostasis of the healthy retina, but also in cellular communication after injection therapies [73–77]. They are membrane bound carriers, that are classified into three groups based on their size and biogenesis (**Fig. 7** left). Exosomes are considered to be the smallest vesicles with a diameter of 30-150 nm and origin from endocytic multivesicular bodies (MVBs) [71]. The second group are microvesicles with a diameter of 100-1000 nm, that are produced by budding and blebbing from the plasma membrane. The largest extracellular vesicles, which are bigger than 1000 nm in diameter, are apoptotic bodies that get released by cells after cell death [78]. Extracellular vesicles are further differentiated based on their composition of proteins, nucleic acids, lipids and metabolites, although some markers overlap between different groups [79].

In recent studies, the role of exosomes in pathophysiological processes and their therapeutic potential, especially in cancer and cardiovascular diseases, has gained a lot of attention as they can transfer their cargo to surrounding cells [72,80].

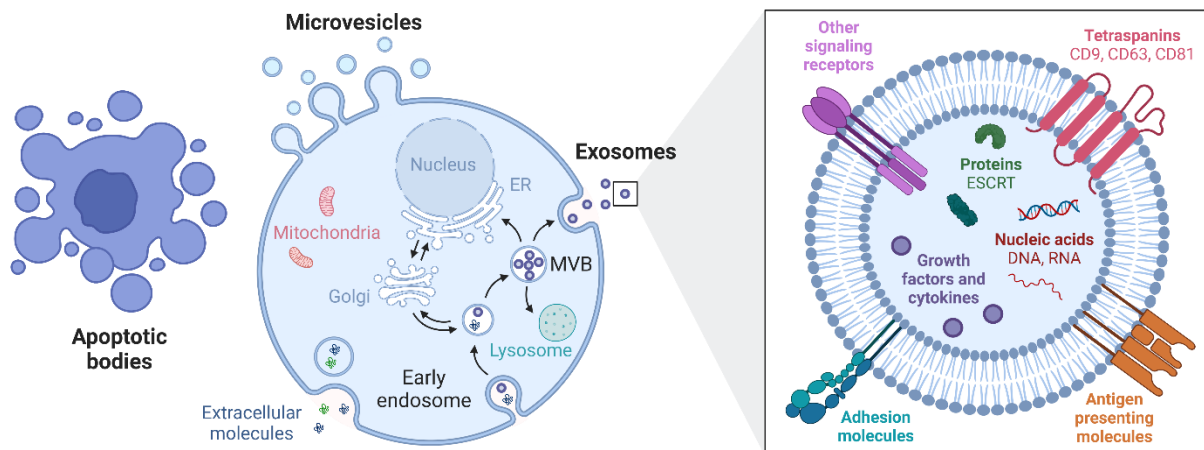


Figure 7: Biogenesis of extracellular vesicles and exosome composition.

Extracellular vesicles are classified into three groups based on their size and biogenesis. Apoptotic bodies are released by cells that undergo programmed cell death, while microvesicles are produced by blebbing and budding from the cell membrane. Exosomes originate from multivesicular bodies (MVBs) and are released by exocytosis. Their membrane contains various transmembrane proteins and they transport different cargo, such as proteins, cytokines or nucleic acids. Created with BioRender.com

The composition of exosomes can be mainly distinguished from bigger extracellular vesicles by the expression of membrane-bound tetraspanin proteins (CD9, CD63 and CD81) and flotillins, as well as endogenous proteins from the endosomal sorting complex required for transport (ESCRT), such as the apoptosis-linked gene 2 interacting protein X (ALIX) (Fig. 7 right) [81–83]. While some markers are common among all exosomes, other proteins, like the antigen presenting molecules, are specific to the donor cell type [84]. The cargo of exosomes contains all kinds of nucleic acids, even including DNA, as well as functional proteins and metabolites [79,85,86]. After exocytosis from the donor cell, exosomes can undergo membrane fusion at the recipient membrane with subsequent cargo release, direct interaction via receptor signaling or internalization into early endosomes. Contents from early endosomes are then spread into several different pathways resulting in their further exocytosis, degradation in lysosomes, cytosolic release or uptake by the nucleus or endoplasmic reticulum (ER) [79].

1.3.2 Role of extracellular vesicles in retinal health and disease

During early stages of retinal development, cultured retinal progenitor cells and retinal organoids have been shown to release extracellular vesicles, that contain RNA of various transcription factors amongst others [87,88]. It has also been described that healthy photoreceptors, that were isolated shortly after birth (P0-P8), are able to release extracellular vesicles in culture, that carry phototransduction proteins and other cargo [62,63]. In these mice, multivesicular bodies have been shown to accumulate at the cell membrane in photoreceptor inner segments in close proximity to Müller cells [62]. In fact, Müller cells have been described as one of the main retinal cell types, that release small and large extracellular vesicles, which contribute to their interaction with neurons and angiogenesis [89–91]. In adult photoreceptors, only low release of extracellular vesicles remains [76]. The reason for this might be the intermediate filament protein peripherin, which was reported to suppress membrane budding and thus microvesicle release [92,93]. In accordance, it was displayed that the majority of isolated extracellular vesicles from wildtype mice contained ESCRT proteins suggesting origin from multivesicular bodies [74]. Nonetheless, the role and functional significance of released extracellular vesicles in retinal development and adulthood could not be revealed yet.

In contrast, mouse retinal explant cultures exhibiting photoreceptor degeneration did show an increased extracellular vesicle released, which may also originate from other cells than photoreceptors, e.g. from Müller cells [94]. In addition, it has been reported that RPE cells release different types of extracellular vesicles both from their apical and basal side, that changed in composition upon pathology induction [73,77]. However, there are no data available yet demonstrating the role of extracellular vesicles in health or pathology-induced photoreceptor signaling.

Although the importance of exosomes in retinal disease has not been fully studied, the retina is an ideal target for exosome-based therapy as is it immune-privileged by the blood-retinal barrier [80]. Suitably, exosomes are described as attractive therapeutic vectors due to their reduced immunogenicity and bi-layered lipid structure, that protects the cargo from degradation. Furthermore, their small size and membrane composition allow them to cross biological membranes, such as the blood-retinal barrier [95]. It has been hypothesized that one of the therapeutic mechanisms of transplanted stem cells, which are used as replacement throughout retinal cell death or to provide trophic support to the damaged cells, is the release of extracellular vesicles [96]. In a retinal degeneration mouse model, it has already been shown that transplanted neural progenitor cells secrete exosomes, that protect photoreceptors by inactivation of microglia [97]. In addition, it has been described that RPE-derived exosomes are able to protect dying

photoreceptors in mice by suppression of inflammatory immune responses [75,98]. Interestingly, AAV vectors were reported to associate with microvesicles and exosomes, either at their membrane or inside the vesicles, which enhances transduction capacity while being inaccessible for neutralizing antibodies and even giving them the ability to cross the blood-brain barrier [99-104]. However, it has not been clearly defined which retinal cells are able to internalize EVs as their visualization turned out to be challenging [76,105].

1.4 Retinitis pigmentosa mouse models

Various different mouse models have been used for decades to study the progression and therapy of retinal diseases. Thereby, two mouse models, named *Pde6b^{rd1}* and *Pde6b^{rd10}*, have been used most extensively as PR degeneration models. *Pde6b^{rd1}* mice carry a nonsense mutation in exon 7 of the *Pde6b* gene. As a consequence, rods begin to die at postnatal day 8 (P8) and complete loss is already observed at P20 [106,107]. In *Pde6b^{rd10}* mice, exon 13 of the *Pde6b* gene is affected by a missense mutation. Rod degeneration in these mice progresses slower compared to *Pde6b^{rd1}* mice as it starts at P16 and is completed by P60 [108,109]. Nevertheless, these mouse models only allow a very short therapeutic window and treatment cannot be achieved without injection approaches. To this purpose, a genetically engineered mouse model, which utilizes the non-invasive Cre-*LoxP* system for genetic rescue, was used in this study.

1.4.1 *Pde6b^{STOP/STOP}* mouse line as model for retinitis pigmentosa

In this study, a mouse model with a disrupted *Pde6b* gene was used [38]. To obtain the interruption of its transcription, a *LoxP*-flanked STOP cassette sequence is placed in intron 1 of the *Pde6b* gene [110]. In control mice (*Pde6b^{ST/WT}*), only one allele has the mutation while the other allele ensures PDE6B expression. By this, rod degeneration is prevented and mice have a normal wildtype phenotype (**Fig. 8** top). Mutant mice (*Pde6b^{ST/ST}*) exhibit this alteration on both alleles causing a lack of PDE6B expression and subsequent cell death of rods over time (**Fig. 8** bottom). As PDE6B is needed for the degradation of cGMP to GMP during visual phototransduction, *Pde6b^{ST/ST}* mice are completely blind from birth.

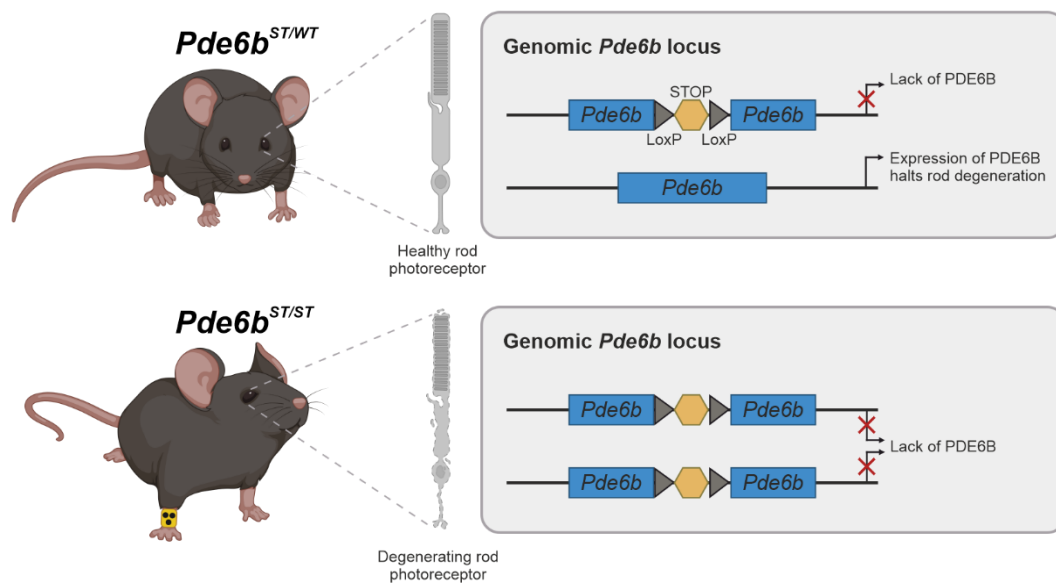


Figure 8: *Pde6b*^{STOP} mice as model for retinitis pigmentosa.

As control, *Pde6b*^{ST/WT} mice have one functional *Pde6b* allele, which ensures PDE6B expression and prevents rod degeneration. In *Pde6b*^{ST/ST} mice, both *Pde6b* alleles contain a *LoxP*-flanked STOP cassette, which was inserted in intron 1. The STOP cassette prevents PDE6B expression, which leads to rod degeneration over time. Partly created with BioRender.com

1.4.2 Cre-Lox recombination

As the STOP cassette in *Pde6b*^{ST/ST} mice is flanked by two locus of x-over P1 (*LoxP*) sites, lack of PDE6B can be rescued by expression of Cre recombinase. The Cre-*LoxP* system is a recombinase technology, that allows site-specific DNA modifications. It consists of an enzyme called Cre recombinase, that is produced by bacteriophage P1 and recombines a pair of short target *LoxP* sequences. These *LoxP* sites consist of 34 base pairs (bp) including two 13 bp palindromic repeats and 8 bp core sequences [111,112]. For recombination, the Cre recombinase binds to the first and last palindromic repeats forming a dimer. Dimers of two *LoxP* sites then join together creating a tetramer. Then, the double stranded DNA is cut out by the Cre recombinase and strands are re-joined by the DNA ligase. Depending on the orientation of *LoxP* sites, recombination results in deletion, insertion, translocation or inversion of the target gene [113].

Cre recombinases can be expressed in a spatial manner under the control of a genetic promoter, that marks the specific cell type of interest [114,115]. Furthermore, expression can be induced at a specific timepoint using a Cre recombinase, that is fused to an estrogen receptor, called CreERT, which is only released after addition of tamoxifen [114]. Using these advantages, the Cre-*LoxP* system allows a very specific, simple and efficient genetic manipulation of target cells.

1.4.3 *Pde6b*^{STOP/STOP}, *Pax6αCre*, *ROSA* mouse line

To prevent rod degeneration by partial treatment, *Pde6b*^{ST/ST} mice were crossed with *Pax6αCre* mice (**Fig. 9**). These mice express a Cre recombinase under the P0 promoter of the paired box 6 (Pax6) gene in combination with an alpha enhancer. Pax6 is a developmental protein, that controls the formation of optic vesicles, thus it is only expressed in embryonic stages in photoreceptor precursors. Furthermore, it has been shown that Pax6 only appears in the periphery of the retina [116,117]. In addition, the α regulatory element was added, which enhances the expression in the nasal and temporal periphery of the retina by binding several transcription factors [118]. Although Pax6 plays an important role in retinal development, it was reported to be non-spatially expressed in adult mice exclusively in amacrine cells. Consequently, Cre-*LoxP* recombination of the *Pde6b* STOP cassette was ensured in the retinal periphery, while the central region remained mutant. Moreover, transcription of Cre recombinase was coupled to a GFP tag meaning that nuclei appear GFP-positive in case of Cre expression. As the α-P0-Cre-GFP construct is a transgene, it gets inserted in any random genomic locus of mice offspring [116].

To visualize Cre-*LoxP* recombination, mice were additionally crossed with either *ROSA*^{nT-nG} or *ROSA*^{mT-mG} two-color fluorescent reporter mice. These mice carry a *LoxP*-flanked tandem dimer Tomato (tdTomato) sequence followed by an enhanced GFP (EGFP) sequence inserted into the reverse oriented splice acceptor clone 26 (*ROSA26*) locus. Transcripts from the *ROSA26* locus are normally ubiquitously expressed non-coding RNAs. Importantly, knock-in did not lead to any impairment of endogenous gene function [119]. In *ROSA*^{nT-nG} mice, the expression of fluorophores was coupled to a nuclear localization domain, while in *ROSA*^{mT-mG} mice they were targeted to the plasma membrane [120,121]. Upon Cre-*LoxP* recombination, the tdTomato gene is removed and EGFP can be transcribed. In cells that do not express Cre recombinase, transcription of tdTomato is terminated with a stop codon before the RNA polymerase reaches the EGFP sequence. Taken together, tdTomato-positive cells are non-recombined, while EGFP-positive cells demonstrate recombination due to Cre recombinase expression.

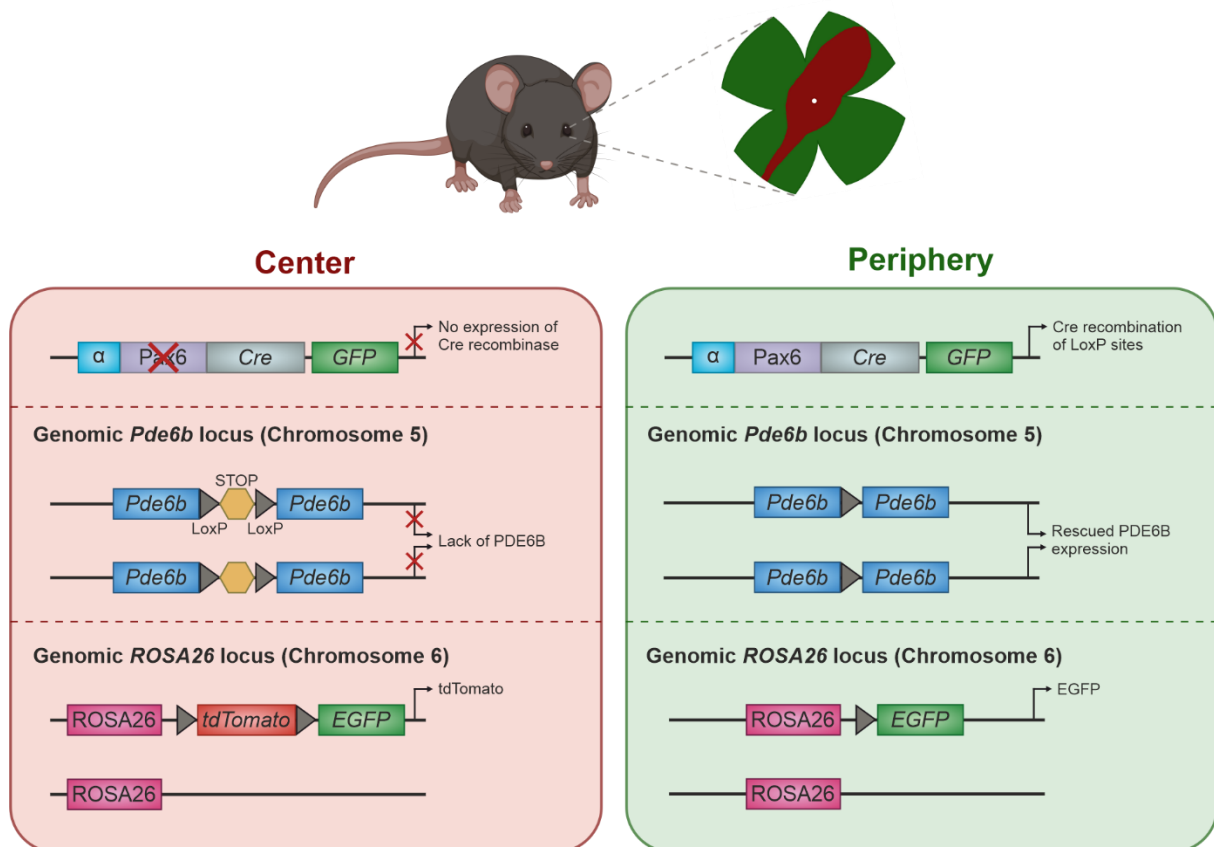


Figure 9: Partial rescue by expression of Pax6 α Cre.

For partial rescue, *Pde6b*^{ST/ST} mice were crossed with *Pax6 α Cre* mice expressing a Cre recombinase under the Pax6 promoter. Mice were further crossed with *ROSA*^{nT-nG} or *ROSA*^{mT-mG} mice to visualize expression of Cre recombinase. As the Pax6 promoter is not active in the center of the retina, the mutant phenotype is preserved and *tdTomato* is expressed. In the prenatal retinal periphery, Pax6 is active and Cre recombinase expressed. Consequently, flanking *LoxP* sites of *Pde6b* and *tdTomato* become recombined, leading to restoration of PDE6B expression and EGFP as marker. Parts created with BioRender.com

All in all, this mouse model offers several advantages to study the disease progression of RP and its treatment. First, rods of *Pde6b*^{ST/ST} mice degenerate comparatively slow, which on the one hand mimics RP progression in humans and on the other hand allows sufficient time for rescue by material transfer [122–124]. Secondly, treatment is achieved by Cre-*LoxP* recombination, which does not cause any injection injuries. Moreover, it rescues photoreceptors effectively and subsequent PDE6B expression levels are comparable to endogenous wildtype levels [122]. As staining of Cre recombinase turns out to be difficult, the *ROSA* reporter allows an endogenous two-color marker for Cre recombinase activity.

2 Aim of the thesis

Retinitis pigmentosa is caused by degeneration of photoreceptors due to genetic mutations in rods. As loss of photoreceptor cells cannot be reversed and the retina lacks any regenerative capacity, several clinical approaches are being tested to prevent further degeneration and disease progression. One of these approaches is the transplantation of healthy photoreceptors or their precursors, which is performed as replacement therapy or to provide trophic support to damaged cells, although it is accompanied by high immune responses. However, it has already been reported that most of these transplanted cells did not integrate into the adult retina but rather interact via material transfer. Another therapeutic method is gene therapy through application of viral vectors, which are only able to treat a restricted area around the injection side.

In this study, it was aimed to evaluate the possibility of interactions between healthy and mutant rods after partial rescue and later the underlying mechanism of suggested endogenous horizontal material transfer. Furthermore, it was supposed to investigate whether secondary remodeling of the inner retina, especially of bipolar and horizontal cells, blood vessels, and the RPE can be halted. Besides the evaluation of an interaction between rescued and mutant cells, it was of special interest which kind of cellular material is transported and if this mechanism is specific to unfulfilled needs of recipient cells. In particular, it was to be determined if small extracellular vesicles might be the responsible carriers of transferred material.

To this purpose, the *Pde6b*^{STOP/STOP} mouse line was used as model for retinal degeneration with partial rescue through expression of Pax6 α Cre combined with either nuclear (*ROSA*^{nT-nG}) or membrane-bound (*ROSA*^{mT-mG}) endogenous Cre recombinase reporters. To evaluate the resultant effects, an extensive morphological evaluation and analysis of expression profiles in retinas and RPE cells from wildtype, mutant and partially rescued mice was performed. In addition, electroretinogram recordings were conducted to study retinal function. Moreover, extracellular vesicles were isolated from mice or imaged in retinal sections using electron microscopy for their characterization, cargo analysis and proof of concept studies *in vitro* as well as *ex vivo*.

3 Material and methods

3.1 Material

3.1.1 Buffers and solutions

Unless otherwise indicated, all buffers were prepared with double-distilled water (ddH₂O).

Table 1: Composition of utilized buffers and solutions

Buffer	Composition
Anesthetic solution	1X PBS (sterile), 10 mg/ml Ketamine, 0.2 mg/ml Xylazine
EZL 5X	136 mM NaCl, 3 mM KCl, 1 mM MgCl ₂ x 6H ₂ O, 10 mM HEPES, 2 mM CaCl ₂ , 11 mM Glucose
EZL 1X (pH 7.4)	1:5 EZL 5X
FACS sample buffer	PBS 1X, 2 mM EDTA, 25 mM HEPES, 2% FBS
Laemmli sample buffer 5X (pH 6.8)	25% Glycerol, 12,5% β-Mercaptoethanol, 5% SDS, 0.026% Bromphenolblue in 1,25 M Tris-HCl
PBS 10X	1.37 M NaCl, 27 mM KCl, 100 mM Na ₂ HPO ₄ , 18 mM KH ₂ PO ₄
PBS 1X (pH 7.4)	1:10 PBS 10X
PBS/Glucose	PBS 1X, 12 mM Glucose
Running buffer 10X	250 mM Tris, 1.9 M Glycine
Running buffer 1X	1:10 Running buffer 10X, 0.1% SDS
Separation gel, 10%	10% Rotiphorese Gel 30, 0.39 M Tris-HCl (pH 8.8), 0.1% SDS, 0.1% APS, 0.0013% TEMED
SSC 20X (pH 7.0)	3 M NaCl, 0.34 M Na ₃ C ₆ H ₅ O ₇
SSC 5X	1:4 SSC 20X
Stacking gel	2% Rotiphorese Gel 30, 0.13 M Tris-HCl (pH 6.8), 0.1% SDS, 0.1% APS, 0.002% TEMED
TAE 1X	1:50 TAE 50X
TAE 50X	2 M Tris base, 1 M Acetic acid, 0.05 M EDTA (pH 8.0)
TBS 10X (pH 7.5)	500 mM Tris, 1.5 M NaCl
TBS 1X	1:10 TBS 10X
TBST 1X	1:10 TBS 10X, 0.1% Tween-20
Transfer buffer	1:10 Running buffer 10X, 20% Methanol

3.1.2 Chemicals

Table 2: Utilized chemicals and reagents

Product	Supplier	Catalog Number
100 bp DNA Ladder	Thermo Fisher	15628050
30% Bovine serum albumin (BSA) solution	Carl Roth	9401.1
Acetic acid (CH ₃ COOH)	Carl Roth	3738.4
Agarose	Carl Roth	3810.3
Ammonium persulfate (APS)	Carl Roth	9178.3
Aqua-Poly/Mount media	Polysciences	18606
B27 Supplement	Thermo Fisher	17504044
Bromophenol blue sodium salt	Carl Roth	A512.1
Calcium chloride (CaCl ₂)	Carl Roth	CN93.1
ChemiBlocker	Merck Millipore	2170
cOmplete Protease Inhibitor Cocktail	Sigma Aldrich	11697498001
D(+)-Glucose	Carl Roth	HN06.2
D(+)-Sucrose	Carl Roth	4621.1
Dimethyl sulfoxide (DMSO)	Carl Roth	A994.1
Disodium phosphate (Na ₂ HPO ₄)	Carl Roth	T876.1
DMEM, low glucose, GlutaMAX Supplement, pyruvate medium	Thermo Fisher	21885
DMEM/F-12	Thermo Fisher	11320074
DNase I	Sigma Aldrich	11284932001
Dulbecco's phosphate buffered saline (DPBS)	Thermo Fisher	14190250
Ethanol, absolute	Carl Roth	5054.1
Ethylenediamine tetraacetic acid (EDTA)	Sigma Aldrich	E1644
Fetal bovine serum (FBS)	Thermo Fisher	10270106
Fix Buffer	BD Biosciences	557870
Glutardialdehyde solution 25%	Merck Millipore	1.04239.0250
Glycerol	Carl Roth	3783.3
Glycine	Carl Roth	0079.3
Hoechst 33342, Trihydrochloride, Trihydrate	Thermo Fisher	H1399
Hydrochloric acid	Carl Roth	9277.1

Product	Supplier	Catalog Number
Hydrogen peroxide 35%	Carl Roth	9683.4
Hydroxyethyl-piperazineethanesulfonic acid (HEPES)	Carl Roth	HN77.3
Immobilon Forte Western HRP Substrate	Merck Millipore	WBLUF0100
Isopropanol	Carl Roth	6752.2
Ketamine 10%	Bela-pharm	9089.01.00
Magnesium chloride hexahydrate ($\text{MgCl}_2 \times 6\text{H}_2\text{O}$)	Carl Roth	HN03.1
Methanol	Carl Roth	0082.3
Methocel 2% eyedrops	OmniVision	04682367
Monopotassium phosphate (KH_2PO_4)	Carl Roth	3904.2
M-PER Mammalian Protein Extraction Reagent	Thermo Fisher	78503
Mydriaticum Stulln 2.5% eye drops (0.5% tropicamide-phenylephrine)	Pharma Stulln	4647856
Neosynephrin-POS 10% eye drops	Ursapharm	828590
Non-fat dry milk powder	Santa Cruz	sc-2324
Opal 650 Reagent Pack	AKOYA	FP1496001KT
PageRuler Plus Prestained Protein Ladder	Thermo Fisher	26619
Papain	Sigma Aldrich	10108014001
Paraformaldehyde (PFA)	Carl Roth	0335.2
Penicillin/Streptomycin (Pen/Strep)	Thermo Fisher	15140122
Perm/Wash Buffer	BD Biosciences	557885
Potassium chloride (KCl)	Carl Roth	6781.3
Proxylaz 20 mg/mL (xylazinehydrochloride)	Bela-pharm	3100408.00.00
RNAscope Probe - Mm-CRE-C2	Bio-Techne	312281-C2
RNAscope Probe - Mm-Pde6b-C2	Bio-Techne	1202511-C2
RNAscope Probe Diluent	Bio-Techne	300041
Rotiphorese Acrylamide solution 30%	Carl Roth	A124.1
Sodium chloride (NaCl)	VWR	27810.295
Sodium citrate dihydrate ($\text{Na}_3\text{C}_6\text{H}_5\text{O}_7 \times 2\text{H}_2\text{O}$)	VWR	27833.363
Sodium dodecyl sulfate (SDS)	Carl Roth	2326.1
Sybr Green	Thermo Fisher	A25741
Sybr Safe DNA Gel Stain	Thermo Fisher	S33102
Tetramethylethylenediamine (TEMED)	Carl Roth	2367.3

Product	Supplier	Catalog Number
Tissue-Tek O.C.T. Compound	Hartenstein	TTEK
Tris	Carl Roth	0188.2
Tris base	Sigma Aldrich	T1503-1KG
Triton-X-100	Carl Roth	3051.3
Trypsin (1:250)	Thermo Fisher	27250018
Trypsin 0.05% EDTA	Thermo Fisher	25300054
Tween-20	Carl Roth	9127.1
Type F Immersion liquid	Leica	11513859
UltraPure DNase/RNase-Free distilled water	Thermo Fisher	10977035
β -Mercaptoethanol	Sigma Aldrich	M7522

3.1.3 Consumables

Table 3: Utilized consumables

Product	Supplier	Catalog Number
0.2 ml 8-Strip 'Non-Flex' Natural PCR Tubes, Attached Flat Caps	Starlab	I1402-3700
10 cm Cell Culture Dish	Thermo Fisher	150350
10 ml Serological Pipette	Sarstedt	861.685.020
25 ml Serological Pipette	Sarstedt	72.695.500
31.5 mL, Open-Top Thinwall Polypropylene Konical Tube, 25 x 89mm	Beckman Coulter	358126
35 x 10 mm CytoOne Dish, TC-Treated	Starlab	CC7682-3340
48-Well CytoOne Plate, TC-Treated	Starlab	CC7682-7548
5 ml Serological Pipette	Sarstedt	861.253.001
Biopsy Punch 1.0 mm	Kai medical	BPP-10F
Chromatography-Papers Whatman 0.92 mm	Carl Roth	7602.1
Circle Writer Liquid Blocker	Science Services	CWAL-FG
Coverslips thickness 1, 24 x 24 mm	Carl Roth	H875.2
Coverslips thickness 1, 24 x 60 mm	Carl Roth	H878.2

Product	Supplier	Catalog Number
Cryomold embedding dishes	Hartenstein	CMM
Disposable needles Sterican long bevel facet, 40 mm, 0.80 mm, green	Carl Roth	X127.1
Falcon round-bottom tubes PS 5	Corning	352008
MicroAmp Fast Optical 96-Well Reaction Plate, 0.1 mL	Thermo Fisher	4346907
MicroAmp Optical Adhesive Film	Thermo Fisher	4360954
Microtome blades, Feather	Hartenstein	C35
Millicell Cell Culture Inserts 30 mm	Millipore	PICM0RG50
Omnican 50 0.5 ml 0.30x8 mm	NeoLab	9151117
Omnifix Solo disposable syringes	B. Braun	4616103V
Parafilm Sealing Film	Starlab	I3080-1038
Pasteur pipettes	Carl Roth	4522
Polystyrene 24-well Cell Culture Multiwell Plate	Greiner Bio-One	662160
Polystyrene 6-well Cell Culture Multiwell Plates	Greiner Bio-One	657160
PVDF Transfer Membrane, 0.2 μ m	Sigma	GE10600021
Safeseal tube 1,5 mL	Sarstedt	72.706
Safeseal tube 2 mL	Sarstedt	72.695.500
Scalpel	NeoLab	294200101
Screw cap tube, 15 ml	Sarstedt	62554502
Screw cap tube, 50 ml	Sarstedt	62559001
Sterican Needles	B. Braun	4656300
Syringe filters, sterile filtration, 0.2 μ m	VWR	514-0072
X72 Superfrost Plus slides	Fisher Scientific	10149870

3.1.4 Commercial kits

Table 4: Utilized commercial kits

Product	Supplier	Catalog Number
AllPrep DNA/RNA FFPE Kit	Quiagen	80234
H&E Fast Staining Kit	Carl Roth	9194.1
miRNeasy Serum/Plasma Advanced Kit	Quiagen	217204
Pierce Coomassie (Bradford) Protein Assay Kit	Thermo Fisher	23200
PKH67 Green Fluorescent Cell Linker Midi Kit	Sigma Aldrich	MIDI67
RevertAid First Strand cDNA Synthesis Kit	Thermo Fisher	K1622
RNAscope Multiplex Fluorescent Reagent kit V2	Bio-Techne	323100

3.1.5 Technical devices

Table 5: Utilized devices and belonging software

Device	Supplier	Software
BZ-X800 Fluorescent Microscope	Keyence	BZ-800 Viewer
ChemiDoc MP	Bio-Rad	Image Lab 6.1
Dmi8 Confocal Microscope	Leica	Leica Application Suite X 3.5.7
Espion ERG	Diagnosys LLC	Espion V6
EVOS FL Microscope	Thermo Fisher	Revision 1.4
FACSAriaFusion	BD Biosciences	BD FACSDiva Software
GelDoc 2000	Bio-Rad	Quantity One
Mastercycler nexus GX2	Eppendorf	-
NanoDrop 2000c	Thermo Fisher	NanoDrop 2000
QuantStudio 5	Applied Biosystems	QuantStudio Design & Analysis Software 1.5.2
SpectraMax iD3	Molecular Devices	SoftMax Pro 7.0.3

Data were analyzed using GraphPad Prism 9, ImageJ 1.54b and CorelDRAW 2019.

3.2 Biological Systems

3.2.1 Cell culture

661W cells were cultivated in DMEM, low glucose, GlutaMAX Supplement, pyruvate medium supplemented with 10% FBS and 1% Pen/Strep in cell culture dishes at 37°C and 5% CO₂. For passaging, cells were washed with DPBS and detached using Trypsin 0.05% EDTA for 5 min at 37°C and 5% CO₂. Fresh medium was added to stop the reaction and a diluted cell suspension was used to further cultivate the cells. Seeding for experiments was carried out in 24-well plates using cell suspensions from passaging.

3.2.2 Mice

All animal experiments were performed according to the ARVO statement for the use of animals in ophthalmic and vision research and were approved by the local authorities (Regierung von Oberbayern). Mice were kept at standard conditions under a 12-hour light/12-hour dark cycle with access to water and food *ad libitum*.

Pde6b^{STOP} and *Pde6g^{CreERT2}* mice were generated in the Barbara & Donald Jonas Stem Cells Laboratory, Columbia University, USA. Mice were rederived via *in vitro* fertilization at the Biomedical Center Munich, Germany. Partial treatment was achieved by crossing with *Pax6αCre* mice, which were obtained from Prof. Dr. Marquardt, University of Göttingen, Germany. In this study, control (*Pde6b^{ST/WT}*), mutant (*Pde6b^{ST/ST}*) and partially rescued (*Pde6b^{ST/ST} Pax6αCre*) mice of both sexes were used. To visualize Cre-*LoxP* recombination, they were additionally crossed with either nuclear *ROSA^{nT-nG}* (strain #023035) or membrane-bound *ROSA^{mT-mG}* (strain #007576) two-color fluorescent reporter mice, which were purchased at Jackson Laboratory. As control for *Pax6αCre* expression, *Pde6g^{CreERT2/WT}* mice of both sexes and one male *RhoCre* (strain #032909) mouse from Prof. Dr. Michalakis, LMU Munich, Germany, were used.

Mice were anesthetized with isoflurane and sacrificed by cervical dislocation.

3.3 Methods

3.3.1 Polymerase chain reaction

To isolate DNA for genotyping, ear punches were boiled in 600 μ l 50 mM NaOH at 95°C for 10 min. Then, 50 μ l 1M Tris-HCL (pH 8.0) was added and mixed by vortexing. Samples were then centrifuged for 6 min at 15,000 xg and stored at 4°C.

MasterMix components (**Table 6**) were mixed without DNA template and portioned into 0.2 ml 8-strip PCR tubes. Gene-specific primers used for genotyping are given in **Table 7**. DNA templates were added to each tube, mixed by vortexing and spun down. Polymerase chain reactions (PCRs) were run in a Mastercycler nexus GX2, whereby lid heating was constantly kept at 105°C. Individual PCR programs are given in **Table 8-13**.

Table 6: MasterMix components for genotyping in μ l

	<i>ROSA^{nT-nG}</i> and <i>Pde6b^{STOP}</i>	<i>Pax6αCre</i>	<i>ROSA^{mT-mG}</i>	<i>Pde6g^{CreERT2}</i>	<i>RhoCre</i>
10X Dreamtaq mix	1.50	1.50	2.50	2.50	2.50
dNTPs	0.50	0.50	0.50	0.50	0.50
10 μ M primer 1	1.25	1.25	1.00	1.00	1.25
10 μ M primer 2	1.25	1.25	1.00	1.00	1.25
10 μ M primer 3	1.25	-	1.00	1.00	-
DNA template	1.00	1.00	3.00	2.00	2.00
PCR grade water	8.13	9.38	15.70	16.70	17.20
Dream Taq polymerase	0.13	0.13	0.30	0.30	0.30
Total volume	15	15	25	25	25

Table 7: Utilized genotyping primers in 100 μ M stock, all ordered from Metabion

Target	Direction	Sequence (5' to 3')	Length in bp	T _m in °C
<i>Pde6b</i> ^{STOP}	forward	TGCTCTGTGGTGTGCTCTGC	21	64.0
	reverse	TGGCGATGCAGAGTGTCTGA	21	65.1
	internal	GTCCTGCACGACGCGAGCTG	20	64.9
<i>Pax6αCre</i>	forward	CGTATGAAGGGGCAATAGA	20	56.1
	reverse	AGGCAAATTTTGGTGTACGG	20	55.7
<i>ROSA</i> ^{nT-nG}	wildtype forward	GGAGCGGGAGAAATGGATATG	21	60.3
	mutant forward	CCAGGCGGGCCATTTACCGTAAG	23	67.2
	common reverse	AAAGTCGCTCTGAGTTGTTAT	21	55.9
<i>ROSA</i> ^{mT-mG}	wildtype forward	AGGGAGCTGCAGTGGAGTAG	20	60.0
	mutant forward	TAGAGCTTGCGGAACCCTTC	20	59.1
	common reverse	CTTTAAGCCTGCCAGAAGA	20	56.7
<i>Pde6g</i> ^{CreERT2}	forward	GGTCAGATTCCAGTGTGTGGG	21	63.0
	reverse	GTTTAGCTGGCCCAAATGTTG	21	59.4
	internal	CTTAGGTGGTCCTTTCCTGGG	21	62.9
<i>RhoCre</i>	forward	GCAGAACCTGAAGATGTTTCGC	21	61.1
	reverse	ACACCAGAGACGGAAATCCAT	21	60.7

Table 8: Thermocycling conditions for amplification of *Pde6b*^{STOP}

Step	Temperature in °C	Duration	Cycles
Initial Denaturation	95	3 min	1
Denaturation	95	30 s	30
Annealing	65	30 s	
Extension	72	1 min	
Final Extension	72	10 min	1
Storage	4	forever	

Table 9: Thermocycling conditions for amplification of *Pax6 α Cre*

Step	Temperature in °C	Duration	Cycles
Initial Denaturation	95	3 min	1
Denaturation	95	30 s	
Annealing	59.6	30 s	30
Extension	72	1 min	
Final Extension	72	10 min	1
Storage	10	forever	

Table 10: Thermocycling conditions for amplification of *ROSA^{nT-nG}*

Step	Temperature in °C	Duration	Cycles
Initial Denaturation	95	3 min	1
Denaturation	95	30 s	
Annealing	60	30 s	30
Extension	72	1 min	
Final Extension	72	10 min	1
Storage	10	forever	

Table 11: Thermocycling conditions for amplification of *ROSA^{mT-mG}*

Step	Temperature in °C	Duration	Cycles
Initial Denaturation	94	2 min	1
Denaturation	95	20 s	
Annealing	65 (-0.5°C/step)	15 s	10
Extension	68	10 s	
Denaturation	94	15 s	
Annealing	60	15 s	28
Extension	72	15 s	
Final Extension	72	2 min	1
Storage	10	forever	

Table 12: Thermocycling conditions for amplification of *Pde6g^{CreERT2}*

Step	Temperature in °C	Duration	Cycles
Initial Denaturation	95	3 min	1
Denaturation	95	30 s	
Annealing	65	30 s	40
Extension	72	1 min	
Final Extension	72	10 min	1
Storage	10	forever	

Table 13: Thermocycling conditions for amplification of *RhoCre*

Step	Temperature in °C	Duration	Cycles
Initial Denaturation	95	3 min	1
Denaturation	95	30 s	
Annealing	58	1 min	35
Extension	72	1 min	
Final Extension	72	2 min	1
Storage	10	forever	

DNA of PCR products was separated by size using agarose gel electrophoresis (**Table 14**). To do so, a 2% agarose gel was prepared by cooking the powder in 1X TAE. To stain the DNA, 2.5 µl Sybr Safe was added per 50 µl gel solution before pouring it into the gel tray. After solidification, the chamber was filled with 1X TAE buffer, then 10 µl of samples and 100 bp DNA ladder each were loaded into the pockets. Gels were run for 15 min at 80 V and imaged using a GelDoc 2000 device.

Table 14: Sizes of PCR products in bp

	<i>Pde6b^{STOP}</i>	<i>Pax6αCre</i>	<i>ROSA^{nT-nG}</i> and <i>ROSA^{mT-mG}</i>	<i>PDE6g^{CreERT2}</i>	<i>RhoCre</i>
Wildtype band	284	-	603	514	-
Recombined band	362	-	-	-	-
Mutant band	415	600	320	715	500

3.3.2 Tissue preparation

Mice were euthanized and directly used for tissue preparation.

Tissue isolation for retinal lysates. Retinas were removed using the Winkler method [125]. Briefly, curved forceps were shoved underneath the eye and the cornea was incised using a scalpel. By pulling the forceps upwards, the retina was scraped out. It was placed in a reaction tube and immediately frozen in liquid nitrogen. Tubes were stored at -80°C .

Eyecup preparation. Before enucleation, the temporal side of the eye was marked with a hot needle on the cornea (**Fig. 10** step 1). Tissue preparation of isolated eyes (**Fig. 10** step 2) was performed in a dry 35 mm dish under a stereo microscope Olympus SZ51. First, the cornea was perforated with a needle. For brief fixation, the eye was incubated in 4% paraformaldehyde (PFA) in 1X phosphate buffered saline (PBS) for 5 min. After, the cornea was removed by a circular cut slightly above the *ora serrata* whereby a small incision at the temporal burn mark was made to preserve the orientation of the eye (**Fig. 10** step 3). Additionally, the iris, lens and vitreous were removed with forceps (**Fig. 10** step 4). Eyecups were fixed in 4% PFA for 45 min and then washed three times in 1X PBS. Afterwards, they were either used for preparation of frozen sections or flatmounts.

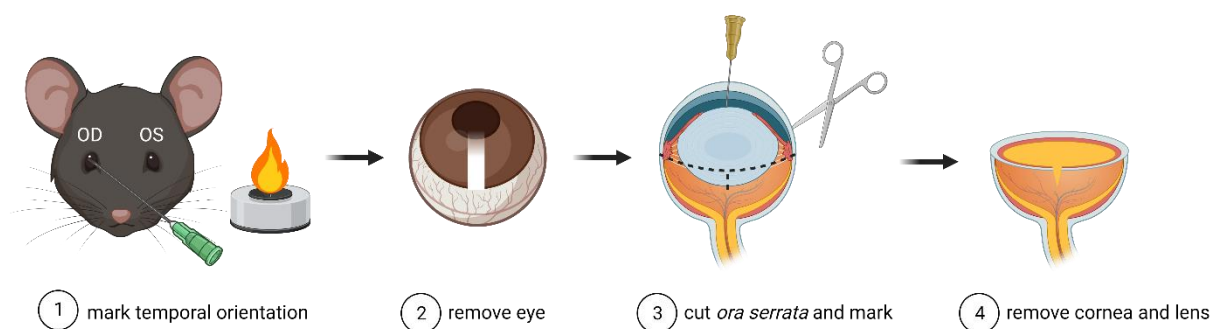


Figure 10: Preparation of the eye.

After the mouse was sacrificed, temporal orientation of eyes was marked with a hot cannula (step 1). The eye was removed (step 2), stung with a needle and placed in 4% PFA. After 5 minutes, the eye was cut circular above the *ora serrata* and slightly into the temporal mark (step 3). Preparation of eyecups was completed by removal of cornea and lens (step 4). Eyecups were used for frozen sections or further prepared to retinal and RPE-choroid-sclera flatmounts. Created with BioRender.com

Preparation of frozen sections. For stabilization of the tissue, eyecups were incubated in 30% sucrose overnight at 4°C. The remaining sucrose solution was dabbed with a tissue. Then, the eyecup was embedded in a Cryomold embedding dish in Tissue-Tek O.C.T. Compound with the temporal orientation facing upwards. Embedded eyecups were frozen on dry ice and stored at -80°C. For sectioning, the frozen block was positioned in a temporal-ventral orientation and cut at 10 µm starting at the dorsal side using the Leica Cryostat CM3050 S. Sections in the central region close to and with the optic nerve were collected on SuperFrost Plus slides. Slides were stored at -20°C for immunofluorescence or at -80°C for fluorescence *in situ* hybridization.

Preparation of flatmounts. To prepare retinal and RPE-choroid-sclera flatmounts, the remaining fat tissue around the sclera at the eyecup was removed. Then, the retina was loosened at the *ora serrata* and separated from the RPE using forceps. For flattening, the retina was quartered with four incisions, while eight incisions were needed for the RPE-choroid-sclera preparation.

3.3.3 Retinal explants

Isolated eyes were directly laid in preparation medium (**Table 15**) and sterilely prepared to RPE-choroid-sclera flatmounts, which were placed on Millicell Cell Culture Inserts in a 6-well plate with the retina facing upward. Culture medium (**Table 15**) was filled below Millicell Cell Culture Inserts. Isolated small EVs were injected subretinally using syringes. Samples were kept at 37°C and 5% CO₂, whereby culture medium was exchanged every two days. On the fifth day, retinas were isolated and further used for quantitative real-time PCR.

Table 15: Retinal explant media

Medium	Composition
Preparation medium	99% DMEM/F-12, 1% Pen/Strep
Culture medium	87% DMEM/F-12, 10% FBS, 2% B27 Supplement, 1% Pen/Strep

3.3.4 Immunofluorescence

Immunofluorescence of eye sections. Frozen slides were thawed and sections were circled using a Circle Writer Liquid Blocker. For washing, sections were covered with one drop 1X PBS. The RPE-choroid-sclera layer was removed under the stereo microscope Olympus SZ51 using needles, forceps and scissors. Liquid on sections was removed by knocking the slides gently on a tissue. Primary antibodies (**Table 16**) were diluted in 5% ChemiBlocker and 0.3% Triton-X-100 in 1X PBS, dropped on sections and incubated overnight at 4°C. For retinal sections, the rabbit-derived GFP antibody as well as the mouse-derived PDE6B antibody were used. After washing three times with 1X PBS, corresponding secondary antibodies (**Table 17**) were added for 1.5 h in 3% ChemiBlocker in 1X PBS. Sections were additionally counterstained with 5 µg/ml Hoechst 33342 solution for 5 min and again washed three times in 1X PBS. For fixation, one drop of Aqua-Poly/Mount media was added per section and then covered. Slides were dried overnight at room temperature and stored at 4°C in the dark.

Immunofluorescence of flatmounts. For staining of flatmounts, primary antibodies (**Table 16**) were diluted in 5% ChemiBlocker in 1X PBS containing 3% DMSO and 0.3% Triton-X-100 overnight at 4°C. For flatmounts from *ROSA^{nT-nG}* mice, the goat-derived GFP antibody was used. After washing three times with 1X PBS, flatmounts were incubated with corresponding secondary antibodies (**Table 17**) for 1.5 h in 3% ChemiBlocker in 1X PBS. After, they were incubated in 5 µg/ml Hoechst 33342 solution for 15 min and again washed three times in 1X PBS. For fixation, flatmounts were placed on slides and covered with cover slips containing Aqua-Poly/Mount media. Slides were dried overnight at room temperature and stored at 4°C in the dark.

Table 16: Immunofluorescence primary antibodies and lectins

Antibody	Species	Dilution	Supplier	Catalog Number
Calbindin D-28k	Mouse	1:8000	Swant	300
Cone Arrestin	Rabbit	1:1000	Merck	AB15282
GARP	Mouse	1:800	Sigma Aldrich	MABN2429
GFP	Goat	1:1000	Biomol	600-101-215
GFP	Rabbit	1:1000	Abcam	Ab6556
Isolectin GS-B4 conjugated FITC	-	1:100	Sigma Aldrich	L2895
PDE6B	Mouse	1:400	Santa Cruz	sc-377486
PDE6B	Rabbit	1:4000	Thermo Fisher	PA1-722
PKC α	Mouse	1:1000	Santa Cruz	sc-8393
Secretagogin	Rabbit	1:5000	Prof. Dr. Wagner (University of Vienna, Austria)	(72)
α -Tubulin	Rat	1:1600	Thermo Fisher	MA180017
β -Catenin	Rabbit	1:1000	Cell Signaling	8480S

Table 17: Immunofluorescence secondary antibodies

Compound	Conjugate	Species	Dilution	Supplier	Catalog Number
Anti-Goat	Alexa Fluor 488	Donkey	1:1000	Thermo Fisher	A-11055
Anti-Mouse	Alexa Fluor 555	Goat	1:1000	Thermo Fisher	A-21425
Anti-Mouse	Alexa Fluor 647	Goat	1:1000	Thermo Fisher	A-21240
Anti-Rabbit	Alexa Fluor 488	Donkey	1:1000	Thermo Fisher	A-21206
Anti-Rabbit	Alexa Fluor 647	Goat	1:1000	Thermo Fisher	A-21245
Anti-Rat	Alexa Fluor 488	Goat	1:1000	Thermo Fisher	A-11006

3.3.5 Fluorescence *in situ* hybridization

Samples were prepared in RNase-free buffers. Fluorescence *in situ* hybridization of RNAs in retinal sections was achieved using the RNAscope Multiplex Fluorescent Reagent Kit according to manufacturer's protocol with slight modifications. In brief, sections were cooked with 1X PBS for 30 min at 60°C followed by post-fixation in 4% PFA for 15 min at 4°C. After dehydration of the tissue using ethanol, samples were directly incubated with Protease III solution for 10 min at 40°C without target retrieval in between. Pde6b RNA was targeted using a custom-made probe binding to its coding sequence (CDS), while Cre RNA was targeted with a commercially available probe. After 2 h hybridization, sections were stored in 5X SSC buffer overnight at room temperature. On the next day, amplification steps for C2 probes were conducted at 40°C, followed by assignment of Opal 650 Reagent. Last but not least, endogenous EGFP signal was amplified by immunofluorescence.

3.3.6 Immunohistochemistry

Retinal trypsin digestion. Trypsin digestion was used to isolate the retinal vasculature for immunohistochemistry staining as previously described with slight modifications [126]. Briefly, eye cups were prepared as described in chapter 3.3.2 without the temporal orientation incision. The retina was removed from the RPE-choroid-sclera tissue and incubated in 4% PFA overnight at 4°C. On the next day, it was washed five times 30 min each with ddH₂O and then kept in ddH₂O overnight at 4°C. For digestion, the retina was incubated in 3% trypsin in 0.1 M Tris (pH 7.8) for 1.5 h at 37°C. The digestion solution was then replaced with ddH₂O and blood vessels were isolated by flushing the retina gently with ddH₂O to remove digested tissue. The vasculature was transferred with a glass pipette on SuperFrost Plus slides and dried at 37°C overnight.

Hematoxylin and eosin staining. After trypsin digestion, the vasculature was stained with the H&E fast staining kit. In detail, hematoxylin was used for staining of cell nuclei in a purplish blue, while eosin was used for staining of the extracellular matrix and cytoplasm in pink. To do so, samples were immersed in the solutions one after the other given in **Table 18**. After the staining procedure, slides were dried overnight and finally fixed with Aqua-Poly/Mount media.

Table 18: H&E staining procedure

Solution	Time
HCL solution (pH 4.3)	10 s
HE solution 1	8 min
HCL solution (pH 4.3)	10 s
HCL solution (pH 2.4)	20 s
Flowing distilled H ₂ O	6 min
HE solution 2	5 min
Flowing distilled H ₂ O	30 s

3.3.7 Imaging

Confocal images of sections were taken with a Leica TCS SP5 Confocal Microscope using a 40x or 63x objective with Type F Immersion liquid.

Images of retinal and RPE-choroid-sclera flatmounts were taken with a Keyence BZ-X800 Microscope or a custom-made VisiScope CSU-X1 confocal system equipped with a high-resolution sCMOS camera (Visitron Systems, Puchheim, Germany). For the vasculature and RPE, pictures were taken in 1 μm distance Z-Stacks from the top to the bottom layer using a 20x objective. Up to three images each were taken in the central and peripheral region. For flatmounts from *ROSA^{nT-nG}* mice, images were taken with the stitching tool using a 10x objective.

Cell culture images were taken with an EVOS FL Microscope.

Representative pictures were chosen as examples.

3.3.8 Quantitative analysis

Quantification of retinal sections. Retinal frozen sections were stained for PDE6B or cone arrestin (CAR) and counterstained with Hoechst 33342. Using ImageJ, the distance from the optic nerve to PDE6B-positive photoreceptors was measured on the nasal and temporal side of the eye. The ONL thickness and cone length was quantified in 50 μm steps from the optic nerve to 700 μm distance both on the nasal and temporal side of the section. The number of replicates per age and genotype for the quantification of sections are given in **Table 19**.

Quantification of GFP-positive area. Retinal flatmounts from *Pde6b^{ST/WT} Pax6 α Cre ROSA^{nT-nG}* and *Pde6b^{ST/ST} Pax6 α Cre ROSA^{nT-nG}* mice were immunolabeled with the goat-derived GFP antibody to amplify the endogenous EGFP signal. Images were analyzed using ImageJ. First, flatmounts were manually selected and GFP pixels inside the selected area were counted by transforming the image into a binary image. The relative GFP-positive area was then calculated by dividing the number of GFP pixels by the number of selected area pixels. The number of replicates per age and genotype for the quantification of the GFP-positive area are listed in **Table 19**.

Table 19: Number of replicates for retinal section and flatmount quantifications

Quantification	Age	<i>Pde6b^{ST/WT}</i>	<i>Pde6b^{ST/ST}</i>	<i>Pde6b^{ST/ST} Pax6αCre</i>
Outer nuclear layer thickness	pw 4	3	3	4
	pw 48	3	3	3
Cone length	pw 48	3	3	3
Distance from ON to PDE6B ⁺ cells	pw 4	-	-	6
	pw 48	-	-	9
GFP-positive area	pw 4	4	-	3
	pw 48	4	-	5

Quantification of retinal vessel area. Imaged Z-Stacks of retinal flatmounts stained with Isolectin GS-IB4 conjugated FITC were divided into superficial vascular plexus (SVP) or deep and intermediate vascular plexus (DVP and IVP) and stacked as maximum intensity projections using ImageJ. The AngioTool software (University of Warwick, UK) was used to quantify the relative vessel area per image [127]. The number of replicates per genotype, region and age for the retinal vessel area analysis are given in **Table 20**.

Quantification of acellular vessels. The number of acellular vessels in H&E stained vasculatures was manually counted with ImageJ by identification of capillaries without nuclei. The number of replicates per genotype, region and age for the acellular vessel analysis are listed in **Table 20**.

Quantification of the retinal pigment epithelium. Imaged Z-Stacks of RPE-choroid-sclera flatmounts stained for β -Catenin were stacked as maximum intensity projections using ImageJ. Automated analysis of cell area, eccentricity and solidity was carried out using the CellProfiler software [128]. The cell eccentricity reflects its elongation while cell solidity is defined as the cell area divided by the convex hull area showing deviations from the hexagonal cell shape (**Fig. 11**). Incorrectly recognized RPE cells were manually excluded. The number of replicates per genotype, region and age for the RPE analysis are given in **Table 20**.

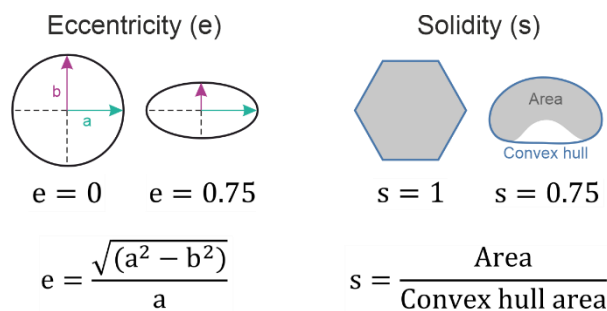


Figure 11: Schematic representation of cell eccentricity and solidity.

Eccentricity, which describes the cellular elongation, and solidity, the proportion of the RPE cell area filling a best-fit convex envelope, of RPE cells were quantified using the CellProfiler software.

Table 20: Number of replicates for vasculature and RPE quantifications

Quantification	Genotype	Center			Periphery		
		pw 4	pw 24	pw 48	pw 4	pw 24	pw 48
Retinal vessel area (DVP + IVP)	<i>Pde6b</i> ^{ST/WT}	6	3	3	6	3	4
	<i>Pde6b</i> ^{ST/ST}	4	3	3	6	3	3
	<i>Pde6b</i> ^{ST/ST} <i>Pax6</i> α <i>Cre</i>	4	4	3	4	4	4
Retinal vessel area (SVP)	<i>Pde6b</i> ^{ST/WT}	-	-	2	-	-	4
	<i>Pde6b</i> ^{ST/ST}	-	-	8	-	-	8
	<i>Pde6b</i> ^{ST/ST} <i>Pax6</i> α <i>Cre</i>	-	-	4	-	-	6
Acellular vessels	<i>Pde6b</i> ^{ST/WT}	3	6	4	3	6	4
	<i>Pde6b</i> ^{ST/ST}	3	3	4	3	5	6
	<i>Pde6b</i> ^{ST/ST} <i>Pax6</i> α <i>Cre</i>	4	5	4	4	6	4
Retinal pigment epithelium	<i>Pde6b</i> ^{ST/WT}	6	5	6	7	5	6
	<i>Pde6b</i> ^{ST/ST}	4	2	3	4	2	3
	<i>Pde6b</i> ^{ST/ST} <i>Pax6</i> α <i>Cre</i>	4	2	3	6	2	3

Data were analyzed using an unpaired t-test or a two-way analysis of variance (ANOVA) with Tukey's multiple comparisons and standard error of the mean (SEM). $P \leq 0.05$ was considered statistically significant ($*P \leq 0.05$; $**P \leq 0.01$; $***P \leq 0.001$).

3.3.9 Correlative light-electron microscopy

Biopsies punches of central and peripheral retinal regions were fixed in 4% PFA in 0.1 M phosphate buffer (PB, pH 7.4) and processed for Tokuyasu cryo-sectioning [129,130] by Dr. Thomas Kurth at the Technical University Dresden, Germany.

In brief, samples were washed in PB, infiltrated stepwise into 10% gelatin (1% for 30 min, 3% for 45 min, 7% for 1h, 10 for 2h) at 37°C, cooled down on ice, incubated in 2.3 M sucrose for 24 h at 4°C, mounted on pins, and plunge frozen in liquid nitrogen. Then, 70-100 nm sections were cut on a Leica UC6+FC6 cryo-ultramicrotome and picked up in methyl cellulose (MC) in sucrose (1 part 2% methyl cellulose, 25 centipoises + 1 part 2.3 M sucrose). Sections were stained with the mouse-derived PDE6B antibody (**Table 16**). Grids were placed upside down on drops of PBS at 37°C for 20 min to remove gelatin, sucrose, and methyl cellulose, then washed with 0.1% glycine in 1X PBS (5x 1 min), blocked with 1% bovine serum albumin (BSA) in 1X PBS (2x 5 min) and incubated with the primary antibody for 1 h. Sections were washed in 1X PBS (4x 2 min), and incubated with rabbit-anti-mouse bridging antibodies [130]. After, they were incubated with protein A conjugated to 10 nm gold for 1 h, washed again in 1X PBS (3x 5 s, 4x 2 min) and post-fixed for 5 min in 1% glutaraldehyde. G Sections were demounted, washed in ddH₂O (10x 1 min), stained with neutral uranyl oxalate (2% uranyl acetate in 0.15 M oxalic acid, pH 7.0) for 5 min, washed in ddH₂O and incubated in MC containing 0.4% UA for 5 min. Grids were looped out, the MC/UA film was reduced to an even thin film and air dried. Finally, the sections were analyzed on a JEM 1400Plus transmission electron microscope (JEOL, Freising, Germany) at 80 kV and images were taken with a Ruby digital camera (JEOL).

3.3.10 Flow cytometry

Enzymatic digestion of retinas. Both retinas of one mouse were isolated using the Winkler method as described in chapter 3.3.2 and placed in PBS/Glucose. For digestion, tissue was incubated in 0.1 U Papain in PBS/Glucose at 37°C for 30 min. After washing three times with PBS/Glucose, retinas were incubated in 200 U DNase I in PBS/Glucose for 4 min. Finally, supernatant was replaced with 1X extracellular solution (EZL) and retinas were dissociated using a glass pipette.

Immunolabeling for FACS. Cell suspension was centrifuged at 400 xg for 5 min at 4°C and supernatant was removed. Cells were fixed by resuspension of the pellet in Fix buffer for 20 min on ice. After another centrifugation step, the pellet was resuspended in Perm/Wash buffer and aliquots for negative control gating were taken. The remaining cell suspension was incubated with primary antibodies, that were all diluted 1:100 in Perm/Wash buffer, for 20 min on ice. Thereby, the goat-derived GFP antibody as well as the rabbit-derived PDE6B antibody were used (**Table 16**). After, the solution was again centrifuged at 400 xg for 5 min at 4°C and the pellet was resuspended in Perm/Wash buffer containing corresponding secondary antibodies, that were all diluted 1:100 (**Table 17**). After incubation for 20 min on ice and centrifugation, the pellet was resuspended in FACS sample buffer and kept on ice until sorting.

FAC-sorting. Measurements were performed using a FACSariaFusion flow cytometer at the Core Facility Flow Cytometry of the Biomedical Center in Munich, Germany. Data were analyzed and gated with the FlowJo software. To exclude debris and dead cells, which are smaller in size, a gate named “cells” was set in a dot plot of sideward scatter height vs. forward scatter area (SSC-H/FSC-A) (**Fig. 12** upper left). Thereby, the forward scatter indicates cell size whereas side scatter relates to the complexity or granularity of the cell. For exclusion of clumped cells, two gating were created, the first one named “singlets 1” with the forward scatter height vs. forward scatter area (**Fig. 12** upper right) and the second one named “singlets 2” with the sideward scatter width vs. sideward scatter height (**Fig. 12** lower left). Finally, PDE6B-Alexa Fluor 647 (AF647) and tdTomato double-positive cells were selected in the “target” gating (**Fig. 12** lower right). Therefore, a *Pde6b*^{ST/WT} retina, which was stained for PDE6B, and a *Pde6b*^{ST/WT} *Pax6αCre ROSA^{nT-nG}* retina, that was labeled with secondary antibodies only, were used as negative controls. The gate was then set by excluding PDE6B signal in the sample which was not stained with PDE6B primary antibody and tdTomato signal in the sample that was negative for the *ROSA^{nT-nG}* reporter.

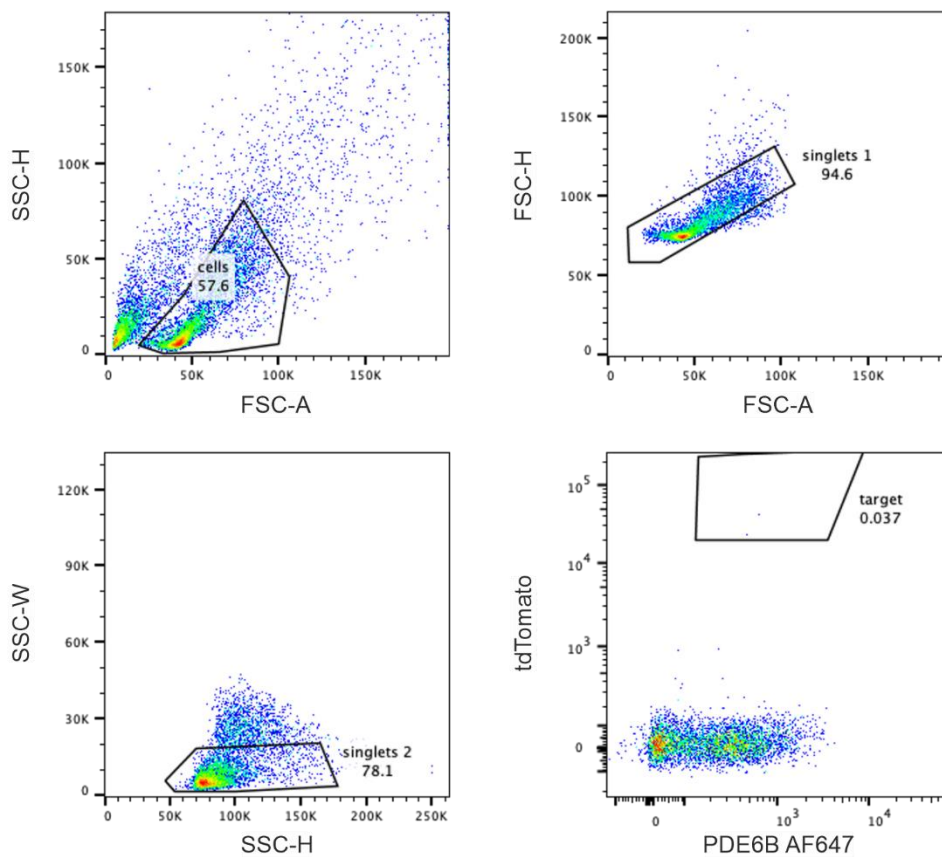


Figure 12: FACS gating strategy using the negative control.

Shown are the representative gating heatmaps for a *Pde6b*^{ST/WT} retina stained for PDE6B, which was used as negative control. Four gating steps were conducted for selection of target cells. First, a gate named “cells” was set in a dot plot of sideward scatter height vs. forward scatter area (SSC-H/FSC-A) to exclude debris and dead cells (upper left). For exclusion of clumped cells, two gatings were created, the first one named “singlets 1” with the forward scatter height vs. forward scatter area (upper right) and the second one named “singlets 2” with the sideward scatter width vs. sideward scatter height (lower left). Double-positive cells for PDE6B Alexa Fluor 647 (AF647) and tdTomato were selected in the “target” gating (lower right). Dots, individual cells; boxes, gates; numbers, relative number of cells in the gating.

3.3.11 Small extracellular vesicles

Isolation of small EVs. For isolation of small EVs by differential ultracentrifugation, both retinas of one mouse were isolated using the Winkler method as described in chapter 3.3.2 and placed in DPBS in a 35 mm dish under a stereo microscope Olympus SZ51 (**Fig. 13** step 1). Leftover tissue was removed before cutting the retinas into small pieces, which were then transferred together with the DPBS to a 15 ml falcon by pipetting (**Fig. 13** step 2). DPBS was removed after retinal pieces sedimented on bottom of the falcon. For tissue digestion, a mixture of 200 U DNase I and

1 mg collagenase D in 500 μ l DPBS was added and incubated for 30 min at 37°C (**Fig. 13** step 3). To allow breakdown of the extracellular matrix (ECM) and vesicle release, falcons were then incubated on ice for 20 min. After, the tissue suspension was neutralized by addition of 11.5 ml DPBS (**Fig. 13** step 4). Subsequent centrifugation at 1,000 xg and 4°C for 10 min was conducted to collect leftover cell debris in a pellet (**Fig. 13** step 5). The vesicle-containing supernatant was transferred to an Open-Top Thinwall Konical Tube and filled up to 30 ml with DPBS. Then, two ultracentrifugation steps were carried out using a Beckman Coulter SW 28 Swinging-Bucket Rotor in a Beckman Coulter Optima LE-80K Ultracentrifuge. In the first step at 10,000 xg and 4°C for 30 min, the small vesicles were further purified by removing bigger vesicles and cell debris in a pellet (**Fig. 13** step 6). After, the supernatant was transferred to a new Open-Top Thinwall Konical Tube. Finally, small EVs were collected in a pellet by centrifugation at 150,000 xg and 4°C for 1.5 h (**Fig. 13** step 7). The supernatant was removed and pellets were dried upside down for 5 min. Vesicles were then used for cell culture experiments, nanoparticle tracking analysis (NTA) or lysed for RNA and DNA isolation.

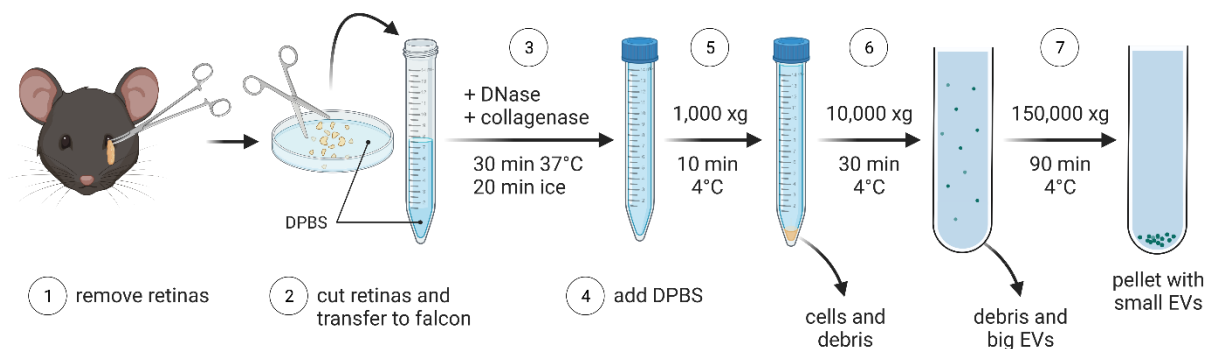


Figure 13: Isolation of small EVs.

Once mice were sacrificed, both retinas were removed (step 1) and placed in DPBS. Tissue was cut into pieces and transferred to a falcon (step 2). Digestion was achieved with DNase I and collagenase D for 30 min at 37°C, followed by 20 min on ice for vesicle release (step 3). After, DPBS was added for neutralization (step 4). Centrifugation at 1,000 xg and 4°C for 10 min was conducted to collect leftover cell debris (step 5). Then, ultracentrifugation at 10,000 xg and 4°C for 30 min was used to remove bigger vesicles and cell debris (step 6). Small EVs were collected in a pellet by ultracentrifugation at 150,000 xg and 4°C for 90 min (step 7). Created with BioRender.com

Immunolabeling of small EVs. Membranes of small EVs were labeled using the PKH67 Green Fluorescent Cell Linker Midi Kit according to manufacturer's protocol with slight modifications. Briefly, the pellet was resuspended in 1 ml Diluent C. After, 6 μ l PKH67 dye was added and continuously mixed by pipetting. Samples were then covered and incubated at room temperature for 5 min. The reaction was quenched by addition of 2 ml 10% BSA in DPBS. In addition, 22.5 ml DPBS were added. A layer of 4.5 ml 0.971 M sucrose was casted to the bottom of the tube using a glass pipette to collect the excel dye. Finally, labeled small EVs were collected by another ultracentrifugation step at 150,000 xg and 4°C for 1.5 h. The pellet was then resuspended in 200 μ l 661W culture medium and added on 30% confluent 661W cells in a 24-well plate. Medium was changed after 24 h incubation and cells were kept for up to five days.

Characterization of small EVs. The small EVs containing pellet was resuspended in 100 μ l DPBS and frozen at -80°C. The number and size of EVs were determined by nanoparticle tracking analysis using a NanoSight NS300 NTA apparatus, the associated software v3.00, and Graph Pad Prism 7 (Malvern Panalytical). For immunoblotting, small EVs from three mice of the same genotype were pooled, resuspended in 50 μ l DPBS and frozen at -80°C. The utilized ALIX antibody is given in **Table 26**. Analysis of small EVs was performed by Dr. Sabine Leitherer at the Hannover Medical School, Germany.

3.3.12 Extraction of DNA and RNA

DNA and RNA from FACS cells or small EVs were isolated using the AllPrep DNA/RNA FFPE Kit according to manufacturer's protocol. Briefly, DNA was separated from RNA by centrifugation. Fixation from cell sorting was reversed by incubation at 80°C for RNA and 90°C for DNA. RNA and DNA were then separately bound to columns by addition of 100% ethanol and washed with different washing buffers. Finally, RNA was eluted with nuclease-free water and DNA with an elution buffer provided in the kit. Samples were stored at -20°C. RNA was used for quantitative real-time PCR (qRT-PCR), while DNA was utilized for PCR identical to genotyping except 2 μ l sample was included as template with accordingly lower volume of PCR grade water.

3.3.13 Quantitative real-time PCR

Quantitative real-time polymerase chain reaction is commonly used to detect changes in protein expression by investigating mRNA levels. To do so, concentration of isolated RNA was measured using the NanoDrop 2000. For the determination of gene expression, RNA was converted into cDNA by reverse transcription using the RevertAid First Strand cDNA Synthesis Kit according to manufacturer's protocol. For one RT-PCR reaction, the MasterMix was prepared as listed in **Table 21**. First, the mixture of primers and 20 ng RNA per sample was filled up to 12 μ l with nuclease-free water and incubated at 65°C for 5 min. Then, the remaining components were added, RT-PCR was run as indicated in **Table 22** and cDNA samples were stored at -20°C.

Table 21: MasterMix for one RT-PCR reaction

Component	Amount
RNA sample	20 ng
Random Hexamer Primers	1 μ l
Oligo (dT) ₁₈ Primers	1 μ l
Nuclease-free H ₂ O	to 12 μ l
5X Reaction Buffer	4 μ l
RNase Inhibitor (20 U/ μ l)	1 μ l
dNTP Mix (10 mM)	2 μ l
Reverse Transcriptase (200 U/ μ l)	1 μ l

Table 22: Settings for RT-PCR run

Step	Temperature in °C	Time in min
Lid Heating	105	constant
Primer extension	25	10
RT reaction	42	60
Inactivation	70	5
Storage	4	forever

Quantitative real-time PCR was performed with duplicates of samples and a negative control with nuclease-free water per primer. For one qRT-PCR reaction, the MasterMix with gene-specific forward and reverse primers and Sybr Green fluorescent dye was prepared as listed in **Table 23**. Measurements took place in a QuantStudio 5 cycler. For FACS samples, the target gene expression was normalized to the house keeper β -Actin. As small EV samples do not contain any cytoskeletal RNA, the target gene expression was normalized to U6 small nuclear RNA (snRNA) instead. Sequences of target gene primers are given in **Table 24**.

The QuantStudio Design & Analysis software was used to analyze qRT-PCR results. Mean values of exponential amplification phase starting points (Ct values) were calculated from duplicates. For the calculation of target fold expression, the term $2^{-(\Delta Ct (\text{sample}) - \Delta Ct (\text{reference}))}$ was used. Thereby, ΔCt was calculated through subtraction of the housekeeping gene Ct value from the Ct value of the gene of interest and wildtype samples were utilized as reference.

Table 23: MasterMix for one qRT-PCR reaction

Component	Volume in μl
Sybr Green	10
Primer forward 10 μM	0.6
Primer reverse 10 μM	0.6
Nuclease-free H ₂ O	3.8
cDNA sample (diluted 1:10)	5

Table 24: Utilized qPCR primers in 100 μM stock, all ordered from Metabion

Target	Direction	Sequence (5' to 3')	Length in bp	T _m in °C
Cre	forward	CTGACGGTGGGAGAATGTTAAT	22	59.4
	reverse	TCAGCTACACCAGAGACGGA	20	59.3
Pde6b	forward	GTGGCTCAGACCAAGAAGATG	21	60.4
	reverse	CACAGCCACGACATCTTTGCC	23	63.4
U6	forward	CTCGCTTCGGCAGCACA	17	60.0
	reverse	AACGCTTCACGAATTTGCGT	20	57.5
β -Actin	forward	CATTGCTGACAGGATGCAGAAGG	23	62.5
	reverse	TGCTGGAAGGTGGACAGTGAGG	22	66.2

Table 25: Settings for qRT-PCR run

Step		Temperature in °C	Time
Lid heating		105	constant
Uracil-DNA Glycosylase activation		50	2 min
Hot-Start DNA Polymerase activation		95	2 min
Amplification 40 X	DNA denaturation	95	3 s
	Annealing	58	5 s
	Elongation	60	25 s
Melt curve acquisition		60	1 min
		Ramp to 95 (0.3/s)	2 min
		95	15 s

3.3.14 Immunoblotting

Immunoblotting is commonly used to visualize changes of intracellular protein levels.

Protein isolation. Frozen retinas were thawed and a mixture of M-PER Mammalian Protein Extraction Reagent and Protease Inhibitor was added. Then, the tissue was lysed using a Branson Sonifier W-450D with 40% amplitude for four times 10 s each. To adjust protein amounts equally, protein concentration was determined using the Pierce Coomassie (Bradford) Protein Assay Kit. To do so, 2 µg/µl albumin was used as protein standard serially diluted in ddH₂O in a flat bottom 96-well plate. Same volume of samples and standard was used to get comparable data. After addition of the reagent solution, absorption was measured with the SpectraMax iD3 plate reader at 595 nm.

SDS Page. To separate the proteins by electrophoresis, samples containing 20 µg protein and 1X Laemmli Sample Buffer were heated at 95°C for 5 min. Afterwards, they were loaded on a 1 mm thick 10 % SDS-polyacrylamide gel with PageRuler Plus Prestained Protein Ladder as molecular weight marker. Gels were run in 1x running buffer for 1.5 h at 120 V.

Western Blot. Separated proteins were transferred from the SDS-polyacrylamide gel to a 0.2 µm PVDF membrane, which was activated for 1 min in methanol before. For the transfer, the membrane and the gel were embedded between two Whatman Papers on each side. Blots were run in transfer buffer for 1.5 h at 90 V on ice.

Immunoassay. Blotted membranes were blocked in 5% non-fat skimmed milk powder in 1X TBST for 1 h. Proteins of interest were detected through incubation of membranes with the respective primary antibodies (**Table 26**) overnight at 4°C and corresponding secondary antibodies (**Table 27**) for 1 h at room temperature. All antibodies were diluted in 5% non-fat skimmed milk powder in 1X TBST. Signals were visualized and detected with the Immobilon Forte Western HRP Substrate by the ChemiDoc MP Imaging System. For detection of other proteins on the same membrane, secondary antibodies were removed by cooking in 1X TBST and the Immunoassay procedure was repeated.

Table 26: Western Blot primary antibodies

Antibody	Species	Dilution	Supplier	Catalog Number
ALIX	Mouse	1:1000	Cell Signaling Technology	2171S
Cre	Rabbit	1:5000	Sigma Aldrich	69050
PDE6B	Mouse	1:100	Santa Cruz	sc-377486
β-Actin-Peroxidase	Mouse	1:3000	Sigma Aldrich	A3854

Table 27: Western Blot secondary antibodies

Compound	Conjugate	Species	Dilution	Supplier	Catalog Number
Anti-Mouse	HRP	-	1:2000	Santa Cruz	sc-516102
Anti-Rabbit	HRP	Mouse	1:2000	Santa Cruz	sc-2357

3.3.15 Electroretinogram recordings

Electroretinogram (ERG) recordings were used to measure the electrical activity of various retinal cells in response to light stimuli. To do so, mice were dark-adapted overnight and the experiment was carried out under dim red light. Then, mice were anesthetized by intraperitoneal (i.p.) injection of 0.1 ml per 10 g body weight anesthetic solution. Mydriaticum Stulln 2.5% eye drops and Neosynephrin-POS 10% eye drops were used one by one to enlarge the pupils. Hydration of the cornea was ensured by application of Methocel 2% eyedrops. ERG responses were recorded on both eyes simultaneously by placing the golden loop electrodes on the corneas (**Fig. 14A**). Measurements were carried out using the Espion E3 ERG in conjunction with the Color Dome. To measure rod response under scotopic conditions, light flash intensities of -3, -2, -1.5, -1, 0.5, and 1 log (cd*s/m²) were used. For suppression of rods, mice were adapted to white light at an intensity of 30 cd/m² for 10 min. Photopic measurements were recorded with light flash intensities of -0.5, 0, 0.5, 1, and 1.5 log (cd*s/m²), which reflects the response of cones. For analysis, a-wave amplitudes were measured from the baseline to the first negative peak and b-wave amplitudes from the low level of the a-wave to the positive peak. For the experiment, 7 *Pde6b*^{ST/WT}, 4 *Pde6b*^{ST/ST} and 4 *Pde6b*^{ST/ST} *Pax6αCre* mice at 40 weeks of age were used. For each animal, the mean response of both eyes was averaged. Data were analyzed using a two-way ANOVA with SEM.

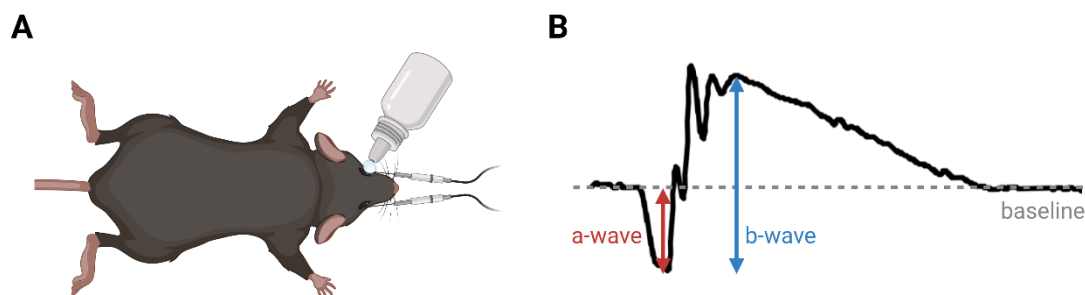


Figure 14: ERG recording and response.

(A) Schematic representation of mice during ERG measurements. Mice were anesthetized and eye drops were used to enlarge the pupils and hydrate the eyes. ERG responses were recorded on both eyes simultaneously by placing the golden loop electrodes on the corneas. **(B)** The a-wave amplitude in ERG responses was measured from the baseline to the first negative peak and b-wave amplitudes from the low level of the a-wave to the positive peak. Created with BioRender.com

4 Results

4.1 Effect of healthy rods on neighboring mutant rods after partial rescue

In this study, the *Pde6b*^{STOP} line was used as RP mouse model, which contains a *LoxP*-flanked STOP cassette sequence in intron 1 of the gene [110]. By this, non-invasive rescue studies without unintentional side effects can be performed through Cre recombination.

4.1.1 Depletion of PDE6B in *Pde6b*^{ST/ST} mice

In *Pde6b*^{ST/ST} mice, both alleles of the *Pde6b* gene contain the STOP cassette causing a lack of PDE6B expression and subsequent rod and cone degeneration, while in *Pde6b*^{ST/WT} mice one functional allele ensures PDE6B expression.

To first gain an understanding of disease progression in our RP mouse model, retinas from *Pde6b*^{ST/ST} mice at 4, 24 and 48 weeks of age were analyzed. Retinas from *Pde6b*^{ST/WT} at 48 weeks of age were used as control. Cones and rod outer segments were visualized by immunofluorescence of cone arrestin (CAR) and glutamic-acid-rich protein (GARP), respectively. Immunofluorescence of PDE6B was used to confirm deficiency in *Pde6b*^{ST/ST} mice. At all timepoints, PDE6B was completely absent in *Pde6b*^{ST/ST} sections, while *Pde6b*^{ST/WT} sections show PDE6B expression in rod outer segments (**Fig. 15**).

In contrast, GARP, a domain of the rod cyclic nucleotide gated beta1 (CNGB1) channel subunit, was found in *Pde6b*^{ST/WT} sections as well as residually in 4-weeks-old *Pde6b*^{ST/ST} mice, but not at 24 or 48 weeks of age, demonstrating shortening and later loss of rod outer segments. Immunolabeling with CAR revealed shortening of cones along with thinning of the outer nuclear layer in 4-weeks-old in *Pde6b*^{ST/ST} mice. At 24 weeks of age, only cone cell bodies were left and rods were mostly degenerated as almost no CAR-negative cells were found. Finally, the outer nuclear layer of 48-weeks-old *Pde6b*^{ST/ST} mice was completely degenerated with few leftover CAR-positive cell debris.

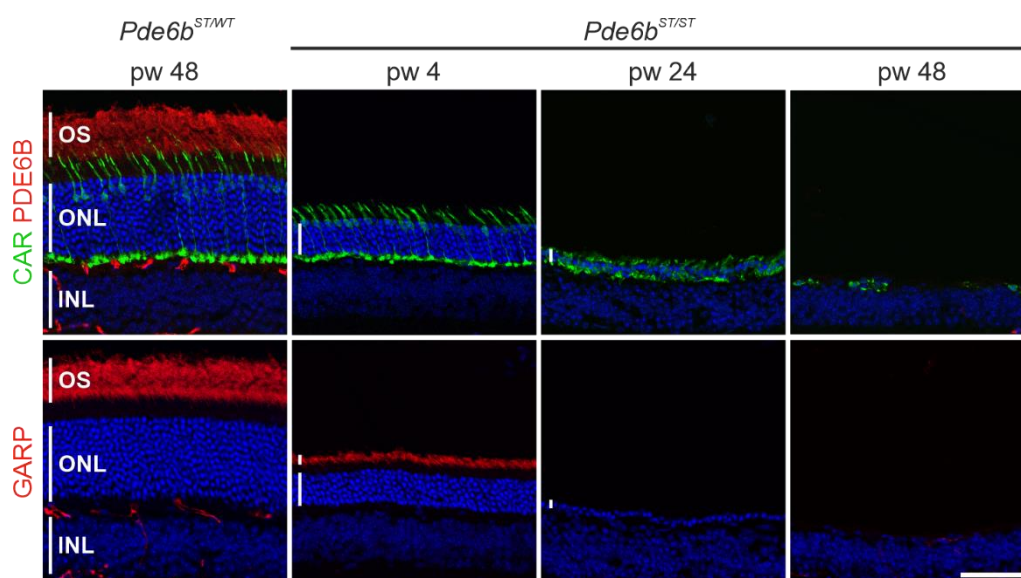


Figure 15: Loss of PDE6B results in progressive photoreceptor degeneration in *Pde6b*^{ST/ST} mice.

Pde6b^{ST/WT} mice were analyzed at 48 weeks of age and *Pde6b*^{ST/ST} mice at 4, 24 or 48 weeks of age. Cones and rod OS were immunolabeled in frozen sections using anti-CAR and anti-PDE6B or anti-GARP, respectively, and counterstained with Hoechst 33342. Representative images are shown. Sections of *Pde6b*^{ST/ST} mice demonstrate absence of PDE6B at any timepoint, leading to a progressive degeneration of photoreceptors (i.e. a decrease in ONL thickness), OS shortening and secondary loss of cones. Vertical white bars, outer segments (OS), outer nuclear layer (ONL) and inner nuclear layer (INL). Scale bar, 50 μ m.

4.1.2 Mosaic Cre expression under Pax6 α promotor

For partial rescue of the *Pde6b*^{ST/ST} phenotype, these mice were crossed with *Pax6 α Cre* mice as the Cre promotor Pax6 α is only active in the temporal and nasal retinal periphery. To visualize Cre-LoxP recombination, *Pde6b*^{ST/ST} *Pax6 α Cre* mice were additionally crossed with nuclear expressed (*ROSA*^{nT-nG}) or membrane-bound (*ROSA*^{mT-mG}) two-color fluorescent reporter mice.

To display the Cre-recombined area, retinal flatmounts of 4- and 48-weeks-old *Pde6b*^{ST/WT} *Pax6 α Cre* *ROSA*^{nT-nG} and *Pde6b*^{ST/ST} *Pax6 α Cre* *ROSA*^{nT-nG} mice were prepared. Endogenous EGFP labeling was amplified by immunofluorescence and relative GFP-positive area was analyzed. Imaging of retinal flatmounts revealed Cre-LoxP recombination only in the periphery, whereby the nasal and temporal side were completely recombined (**Fig. 16A**). A few areas of the dorsal and ventral periphery were shown to be Cre-negative as tdTomato was expressed. Since the Pax6 α promotor is not active in the central region, tdTomato was also expressed circular around the optic nerve demonstrating absence of Cre-LoxP recombination.

Subsequent quantification of relative GFP-positive area in retinal flatmounts showed an overall GFP amount of more than 50% (**Fig. 16B**). At both investigated timepoints, *Pde6b*^{ST/ST} *Pax6α*Cre *ROSA*^{nT-nG} mice had a slightly bigger Cre-recombined area, approximately 10%, compared to *Pde6b*^{ST/WT} *Pax6α*Cre *ROSA*^{nT-nG} mice. In addition, GFP expression of both genotypes was about 5-10% lower at 4 weeks of age compared to 48 weeks of age. Nevertheless, none of these trends was significantly different.

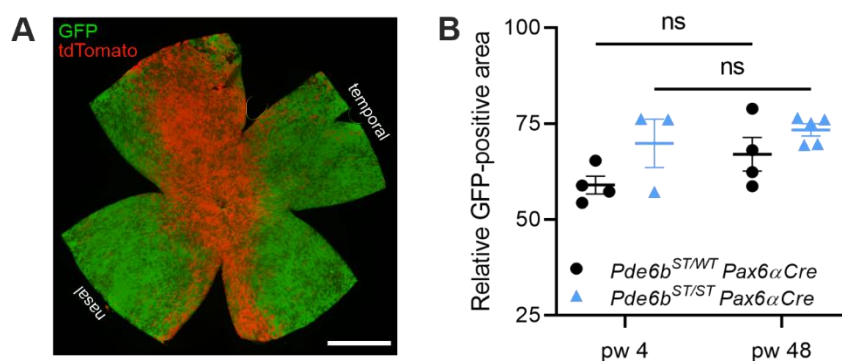


Figure 16: Expression of Cre recombinase in the temporal and nasal periphery of *Pde6b*^{ST/ST} *Pax6α*Cre *ROSA*^{nT-nG} mice.

Pde6b^{ST/WT} *Pax6α*Cre *ROSA*^{nT-nG} and *Pde6b*^{ST/ST} *Pax6α*Cre *ROSA*^{nT-nG} mice were analyzed at 4 or 48 weeks of age and retinas prepared as flatmounts. Label of tdTomato shows Cre-negative regions, while labeling of Cre recombined areas was enhanced using anti-GFP. **(A)** Shown is a representative flatmount of a 4-weeks-old *Pde6b*^{ST/WT} *Pax6α*Cre *ROSA*^{nT-nG} mouse displaying the *Pax6α* expression pattern. Temporal and nasal, retinal orientation. Scale bar, 1 mm. **(B)** Quantification of the relative GFP-positive area in flatmounts was performed using ImageJ. No significant differences in the recombination rate were found between young and old mice of the same genotype. Circles and triangles, individual mice. Data are presented as mean ± SEM. Genotype-matched group means were compared by unpaired t-tests. ns, not significant.

4.1.3 Formation of an ONL gradient due to stepwise PDE6B expression in tdTomato-positive photoreceptors

For the investigation of the retinal phenotype after partial rescue, retinas from 4-, 24- and 48-weeks-old *Pde6b^{ST/ST} Pax6 α Cre ROSA^{nT-nG}* as well as 4- and 48-weeks-old *Pde6b^{ST/ST} Pax6 α Cre ROSA^{mT-mG}* mice were analyzed. The ROSA reporter was used to visualize non-recombined cells by tdTomato expression and recombined cells by expression of EGFP. Immunofluorescence of sections was conducted for GFP and PDE6B to show rescued photoreceptors. As controls, *Pde6b^{ST/WT} Pax6 α Cre ROSA^{nT-nG}* and *Pde6b^{ST/ST} ROSA^{nT-nG}* mice were analyzed at 48 and 4 weeks of age, respectively. In *Pde6b^{ST/WT} Pax6 α Cre ROSA^{nT-nG}* retinas, PDE6B was present in outer segments of GFP- and tdTomato-positive photoreceptors. On the other hand, no PDE6B and GFP signal was found in *Pde6b^{ST/ST} ROSA^{nT-nG}* sections. In *Pde6b^{ST/ST} Pax6 α Cre ROSA^{nT-nG}* and *Pde6b^{ST/ST} Pax6 α Cre ROSA^{mT-mG}* mice, PDE6B was only expressed in the outer segments of GFP-positive rods in 4-weeks-old mice (**Fig. 17A, B**). In sections from 24-weeks-old mice, PDE6B was also present in the outer segments of tdTomato-positive photoreceptors (**Fig. 17A**). In tdTomato-positive photoreceptors, that were far away from GFP-positive ones, but closer to the optic nerve, no expression of PDE6B was found. Finally, at 48 weeks of age all remaining photoreceptors in the outer nuclear layer showed PDE6B expression (**Fig. 17A,B**). No indications for nuclear or membrane fusion were found as both GFP and tdTomato markers did not overlay in any of the two different reporter mice.

In addition, the formation of a gradient in the outer nuclear layer thickness was observed. At 4 weeks of age, *Pde6b^{ST/ST} Pax6 α Cre* showed a slight reduction of photoreceptor nuclei in tdTomato-positive areas (**Fig. 17A,B**). In sections from 24-weeks-old mice, the outer nuclear layer thickness was further diminished in tdTomato-positive but PDE6B-negative areas, while double-positive cells were stepwise retained (**Fig. 17A**). In tdTomato-positive photoreceptors, that did not show PDE6B expression, only two rows of nuclei were left in the outer nuclear layer. At 48 weeks of age, the outer nuclear layer became more and more thinner with higher distance of tdTomato-positive cells to GFP-positive ones (**Fig. 17A,B**). Moreover, PDE6B expression also became lower in the same manner displayed by shorter outer segments.

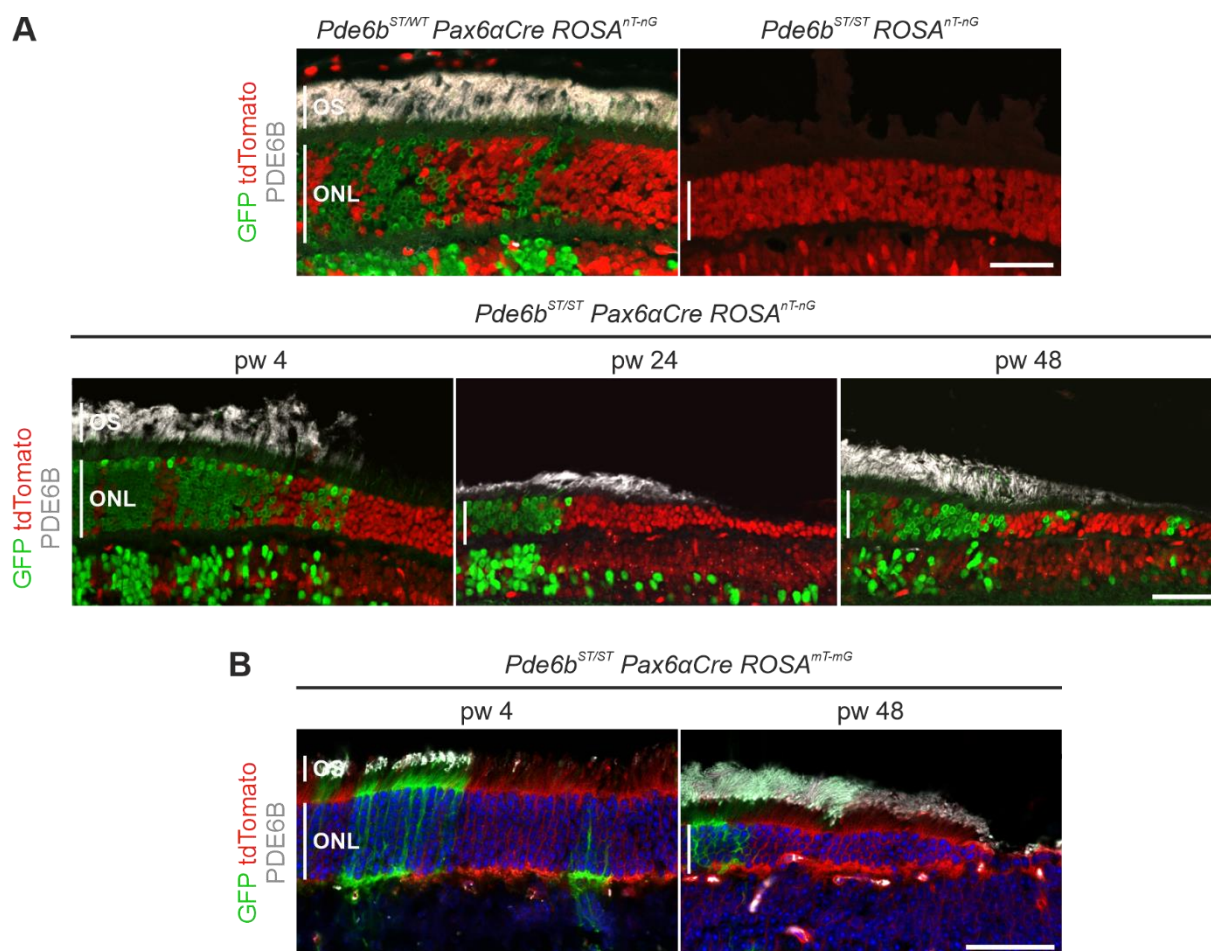


Figure 17: Stepwise PDE6B expression in tdTomato-positive photoreceptors.

(A) *Pde6b^{ST/WT} Pax6αCre ROSA^{nT-nG}* and *Pde6b^{ST/ST} ROSA^{nT-nG}* mice were analyzed at 48 and 4 weeks of age, respectively, and *Pde6b^{ST/ST} Pax6αCre ROSA^{nT-nG}* mice at 4, 24 or 48 weeks of age. Label of tdTomato in retinal sections displays non-recombined nuclei, while labeling of Cre recombined areas was enhanced using anti-GFP with anti-PDE6B co-labeling to show rescued cells. Shown are representative images of the GFP-tdTomato-transition area. **(B)** *Pde6b^{ST/ST} Pax6αCre ROSA^{mT-mG}* mice, expressing the membrane-bound Cre recombinase reporter, were analyzed at the age of 4 or 48 weeks. Retinal sections were immunolabeled using anti-GFP and anti-PDE6B. Shown are representative images of the GFP-tdTomato-transition area. In *Pde6b^{ST/ST} Pax6αCre ROSA^{nT-nG}* sections, PDE6B was mainly present in the OS of GFP-positive cells at 4-weeks-old and then stepwise progressed over time, without membrane fusion of GFP- and tdTomato-positive photoreceptors. Vertical white bars, outer segments (OS) and outer nuclear layer (ONL). Scale bars, 50 μm .

To quantify the stepwise elevation of PDE6B levels, the distance from the optic nerve to PDE6B-positive photoreceptors on the nasal and temporal sides of *Pde6b^{ST/ST} Pax6αCre* sections from 4- and 48-weeks-old mice were measured. At 4 weeks of age, the nasal and temporal distances were 295 $\mu\text{m} \pm \text{SEM}$ and 230 $\mu\text{m} \pm \text{SEM}$, respectively, while at 48 weeks of age the distances were 174 $\mu\text{m} \pm \text{SEM}$ and 77 $\mu\text{m} \pm \text{SEM}$ (**Fig. 18**). Compared to 4 weeks of age, PDE6B expression was about 150 $\mu\text{m} \pm \text{SEM}$ closer to the optic nerve at 48 weeks of age. The difference between 4- and 48-weeks-old mice was significant with $P < 0.02$ for the nasal side and $P \leq 0.01$ for the temporal side. Importantly, some sections showed PDE6B expression in the whole outer nuclear layer, mainly on the temporal side.

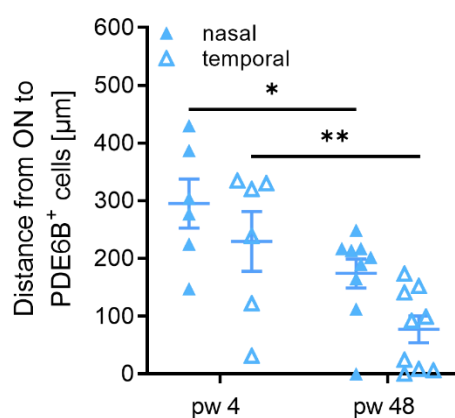


Figure 18: PDE6B expression in tdTomato-positive photoreceptors is more elevated in 48-weeks-old mice.

Pde6b^{ST/ST} Pax6αCre mice were analyzed at 4 or 48 weeks of age. Rescued photoreceptors were immunolabeled using anti-PDE6B in retinal sections. The distance from the optic nerve (ON) to PDE6B-positive photoreceptors was measured on the nasal and temporal side of the sections using ImageJ. On both sides, PDE6B labeling was closer to the ON in old mice compared to young mice. Triangles, individual mice. Data are presented as mean \pm SEM. Area-matched group means were compared by unpaired t-tests. * $P < 0.02$; ** $P \leq 0.01$.

To quantify survival of GFP- and tdTomato-positive photoreceptors, the outer nuclear layer thickness was measured in sections through the optic nerve of 4- and 48-weeks-old *Pde6b^{ST/WT}*, *Pde6b^{ST/ST}* and *Pde6b^{ST/ST} Pax6αCre* mice in 50 μm steps from the optic nerve using the Hoechst 33342 nuclei immunofluorescence counterstaining. At 4 weeks of age, the outer nuclear layer of *Pde6b^{ST/WT}* mice was around 60 μm in thickness (**Fig. 19A**). In *Pde6b^{ST/ST}* sections, it was roughly 40 μm thick, demonstrating a reduction of approximately 40% compared to *Pde6b^{ST/WT}*. Until around 350 μm distance from the optic nerve, *Pde6b^{ST/ST} Pax6αCre* mice demonstrated a similar outer nuclear layer thickness as *Pde6b^{ST/ST}* mice. After, it became gradually thicker and finally, after about 650 μm distance, results were comparable to *Pde6b^{ST/WT}* mice. At 48 weeks of age, *Pde6b^{ST/ST}* mice revealed a completely degenerated outer nuclear layer, while the outer nuclear layer thickness from *Pde6b^{ST/WT}* sections was comparable to the ones from 4-weeks-old sections of the same genotype (**Fig. 19B**). *Pde6b^{ST/ST} Pax6αCre* mice displayed an almost linear gradient in the outer nuclear layer thickness starting at the optic nerve and a nearly similar result as in *Pde6b^{ST/WT}* sections at approximately 700 μm distance. The gradient on the temporal side was shown to be steeper compared to the nasal side. Interestingly, the outer nuclear layer thickness in the retinal periphery of *Pde6b^{ST/ST} Pax6αCre* mice did not overlay completely with the one from *Pde6b^{ST/WT}* sections.

In addition to these observations, cone length was quantified in sections from 48-weeks-old mice using CAR immunolabeling. In *Pde6b^{ST/WT}* sections, overall cone length was approximately 90 μm, with slightly longer cones on the temporal side (**Fig. 19C**). As *Pde6b^{ST/ST}* mice revealed a complete loss of the outer nuclear layer (**Fig. 19B**), also cones were completely degenerated (**Fig. 19C**). Until roughly 150 μm distance from the optic nerve, *Pde6b^{ST/ST} Pax6αCre* mice demonstrated completely degenerated cones as in *Pde6b^{ST/ST}* sections. Afterwards, the cone length was gradually rising and after about 650 μm distance results were comparable to *Pde6b^{ST/WT}*, although they did not overlay completely.

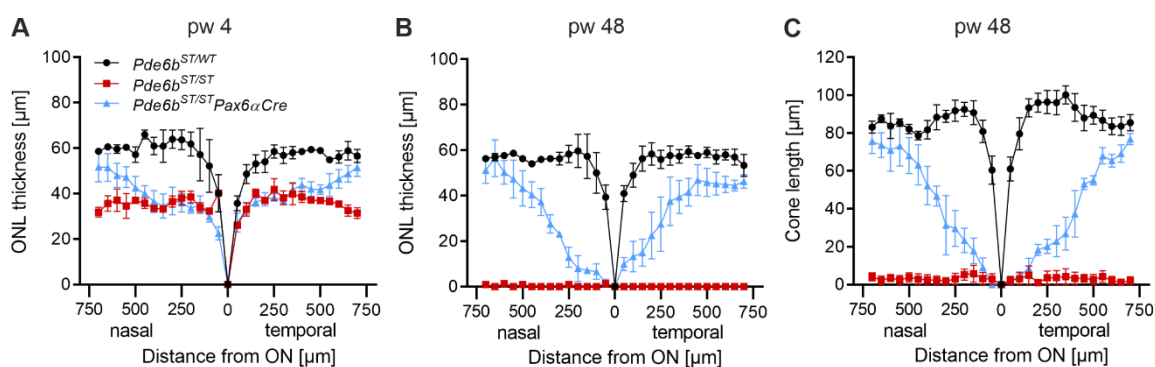


Figure 19: Progression of a gradient in the outer nuclear layer thickness and cone length.

Retinal sections of *Pde6b^{ST/WT}*, *Pde6b^{ST/ST}* and *Pde6b^{ST/ST} Pax6αCre* mice were analyzed on the nasal and temporal side using ImageJ. Nuclei in retinal sections of **(A)** 4-weeks-old or **(B)** 48-weeks-old mice were immunolabeled using Hoechst 33342 and the ONL thickness quantified. At 4 weeks of age, the ONL of *Pde6b^{ST/ST} Pax6αCre* mice degenerates at a similar rate as mutant mice in the center. In sections of 48-weeks-old mice, degeneration of *Pde6b^{ST/ST} Pax6αCre* photoreceptors was gradually halted. **(C)** Retinal sections of 48-weeks-old mice were immunolabeled with anti-CAR to stain cones and cone length quantified. Due to rescue of rods, secondary cone degeneration in *Pde6b^{ST/ST} Pax6αCre* mice was gradually halted. Data are presented as mean \pm SEM. ONL, outer nuclear layer; ON, optic nerve.

4.1.4 Stepwise Pde6b RNA expression in tdTomato-positive photoreceptors

In the next step, it was investigated whether only PDE6B appears in tdTomato-positive photoreceptors or also Pde6b RNA. For this reason, retinal sections of 4-weeks-old *Pde6b^{ST/WT} Pax6αCre ROSA^{nT-nG}* and *Pde6b^{ST/ST} ROSA^{nT-nG}*, as well as 4-, 24- and 48-weeks-old *Pde6b^{ST/ST} Pax6αCre ROSA^{nT-nG}* mice were used to perform fluorescence *in situ* hybridization of Pde6b RNA. In *Pde6b^{ST/WT} Pax6αCre ROSA^{nT-nG}* mice, Pde6b RNA was found in the whole outer nuclear layer, both in tdTomato- and GFP-positive photoreceptors, as well as in photoreceptor inner segments (**Fig. 20** top left). In contrast, no Pde6b RNA signal was found in *Pde6b^{ST/ST} ROSA^{nT-nG}* sections (**Fig. 20** top right). In *Pde6b^{ST/ST} Pax6αCre ROSA^{nT-nG}* mice at 4 weeks of age, Pde6b RNA was highly and predominantly expressed in GFP-positive cells, but only a few dots were found in tdTomato-positive photoreceptors, which were in close proximity to GFP-positive cells (**Fig. 20** bottom left). In *Pde6b^{ST/ST} Pax6αCre ROSA^{nT-nG}* mice at 24 weeks of age, Pde6b RNA was detected in tdTomato-positive photoreceptors (**Fig. 20** bottom mid). Importantly, with higher distance to GFP-positive cells, the concentration of RNA molecules decreased and was completely absent in tdTomato-positive photoreceptors close to the optic nerve. In 48-weeks-old *Pde6b^{ST/ST} Pax6αCre ROSA^{nT-nG}* mice, Pde6b RNA was found in all remaining photoreceptors.

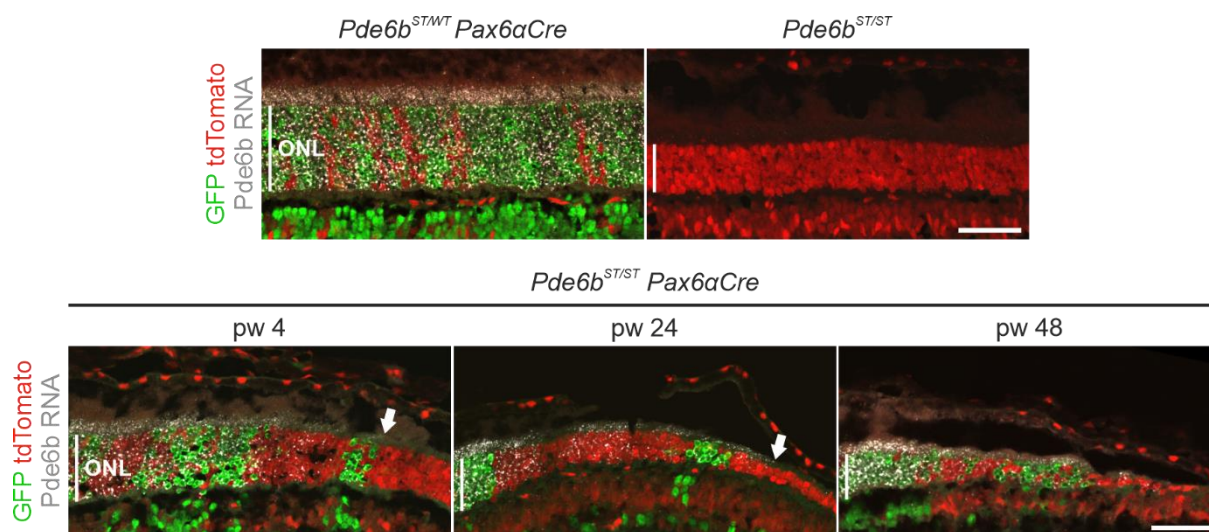


Figure 20: Stepwise expression of Pde6b RNA in tdTomato-positive photoreceptors.

Pde6b^{ST/WT} *Pax6αCre* *ROSA*^{nT-nG}, *Pde6b*^{ST/ST} were analyzed at 4 weeks of age, *Pde6b*^{ST/ST} *Pax6αCre* *ROSA*^{nT-nG} mice at 4, 24 or 48 weeks of age. Label of tdTomato shows non-recombined nuclei, while labeling of Cre recombined nuclei was enhanced using anti-GFP. Retinal sections were used for Pde6b fluorescence *in situ* hybridization. Shown are representative merged images of the GFP-tdTomato-transition areas in close proximity to the optic nerve. In *Pde6b*^{ST/ST} *Pax6αCre* *ROSA*^{nT-nG} sections, Pde6b RNA was mainly present in the OS of GFP-positive cells at 4-weeks-old and then stepwise progressed over time. Arrowheads, end of Pde6b RNA labeling. Vertical white bars, outer nuclear layer (ONL). Scale bar, 50 μm.

To confirm the presence of Pde6b RNA in tdTomato-positive photoreceptors, cells from 24-weeks-old *Pde6b*^{ST/WT} *Pax6αCre* *ROSA*^{nT-nG} and *Pde6b*^{ST/ST} *Pax6αCre* *ROSA*^{nT-nG} mice, that were double-positive for PDE6B and tdTomato, were isolated by FAC-sorting. Since it is challenging to keep the morphology of photoreceptors intact during the procedure, only approximately 4% of retinal cells were selected in the FAC-sorting gate (**Fig. 21A**). Due to the fact that *Pde6b*^{ST/ST} mice do not express PDE6B and can therefore not be isolated by FAC-sorting, whole retinal lysates were used as negative control. DNA and RNA from all samples were separated using the AllPrep DNA/RNA FFPE Kit and RNA was used for quantitative real-time PCR of *Pde6b*. The result demonstrates that Pde6b RNA was present in FAC-sorted cells from *Pde6b*^{ST/WT} *Pax6αCre* *ROSA*^{nT-nG} mice and absent in *Pde6b*^{ST/ST} retinas (**Fig. 21B**). Furthermore, Pde6b RNA was found in PDE6B and tdTomato double-positive cells from *Pde6b*^{ST/ST} *Pax6αCre* *ROSA*^{nT-nG} mice. Its expression was about half of the *Pde6b*^{ST/WT} *Pax6αCre* *ROSA*^{nT-nG} cells.

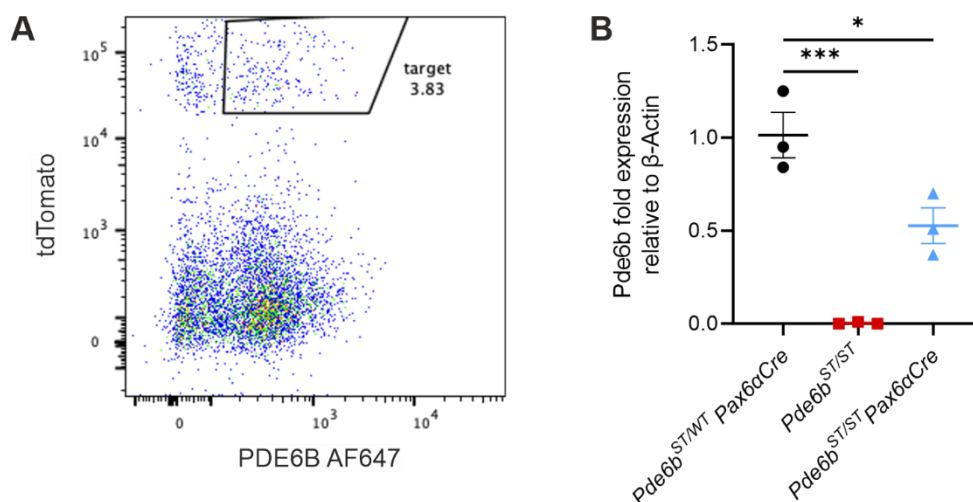


Figure 21: Pde6b RNA in FAC-sorted tdTomato and PDE6B double-positive photoreceptors.

PDE6B expressing Cre-negative cells of *Pde6b*^{ST/WT} *Pax6αCre* *ROSA*^{nT-nG} and *Pde6b*^{ST/ST} *Pax6αCre* *ROSA*^{nT-nG} mice were analyzed at 24 weeks of age. Retinas were digested with Papain and cells were stained with anti-GFP and anti-PDE6B. Photoreceptors were isolated by FAC-sorting of double-positive cells for tdTomato and PDE6B. Retinas from 4-weeks-old *Pde6b*^{ST/ST} were used without sorting as negative control. **(A)** Shown is a representative gating heatmap of a *Pde6b*^{ST/ST} *Pax6αCre* *ROSA*^{nT-nG} mouse demonstrating that only approximately 4% of all retinal cells were selected in the gate. Dots, individual cells; boxes, gates; numbers, relative number of cells in the gating. **(B)** RNA of all samples was isolated and used for quantitative real-time PCR of *Pde6b*. Results were normalized to β-Actin and *Pde6b*^{ST/WT} *Pax6αCre* values. *Pde6b* RNA was present in *Pax6αCre* samples but absent in *Pde6b*^{ST/ST} retinas. Circles, squares and triangles, individual mice. Data are presented as mean ± SEM. Tukey's test for multiple comparisons. * $P = 0.02$; *** $P < 0.001$.

4.1.5 Postnatal absence of Pax6αCre recombinase in photoreceptors

To confirm postnatal inactivity of the Pax6α promoter and subsequent absence of Cre recombinase, retinas of one 4-weeks-old *Pde6b*^{ST/WT} *Pax6αCre* and three 24-weeks-old *Pde6b*^{ST/ST} *Pax6αCre* mice, as well as from one 13-weeks-old *RhoCre* mouse were isolated and used for immunoblotting. Incubation with β-Actin-Peroxidase was performed as loading control showing an equal protein amount in all used samples (**Fig. 22**). Incubation with Cre recombinase antibody revealed expression only in the *RhoCre* positive control, while protein was absent in all retinal lysates from *Pde6b*^{ST/WT} *Pax6αCre* and *Pde6b*^{ST/ST} *Pax6αCre* mice.

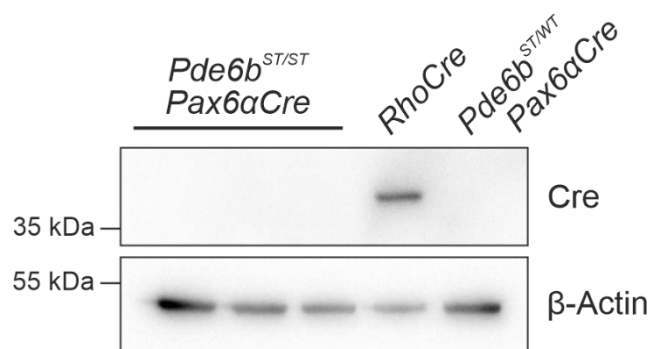


Figure 22: Absence of Pax6 α Cre recombinase protein in adult mice.

Three *Pde6b*^{ST/ST} *Pax6 α Cre* mice, one *RhoCre* mouse used as positive control and one *Pde6b*^{ST/WT} *Pax6 α Cre* mice were analyzed at 24, 13 and 4 weeks of age, respectively. Retinas were isolated, immediately frozen and used for immunoblotting with anti-Cre recombinase, while β -Actin-Peroxidase was used as loading control. Cre was only detected in the *RhoCre* positive control.

As immunoblotting might not be sensitive enough to show low levels of Cre recombinase expression, Cre recombinase RNA was visualized with fluorescence *in situ* hybridization using retinal sections of 4-weeks-old *Pde6b*^{ST/WT} *Pax6 α Cre* *ROSA*^{nT-nG} and *Pde6b*^{ST/ST} *ROSA*^{nT-nG}, as well as from 4, 24 and 48-weeks-old *Pde6b*^{ST/ST} *Pax6 α Cre* *ROSA*^{nT-nG} mice. One 13-weeks-old *RhoCre* mouse was used as positive control. Imaging of *RhoCre* sections showed high expression of Cre recombinase RNA in the outer nuclear layer and photoreceptor inner segments (**Fig. 23**). In contrast, no signal was detected in *Pde6b*^{ST/ST} *ROSA*^{nT-nG} negative control sections. Pax6 α Cre recombinase RNA was absent in the outer nuclear layer of *Pde6b*^{ST/WT} *Pax6 α Cre* *ROSA*^{nT-nG} and *Pde6b*^{ST/ST} *Pax6 α Cre* *ROSA*^{nT-nG} mice at any timepoint. However, it was found in a few GFP-positive nuclei at the inner margin of the inner nuclear layer independently of central or peripheral region (**Fig. 23** arrowheads).

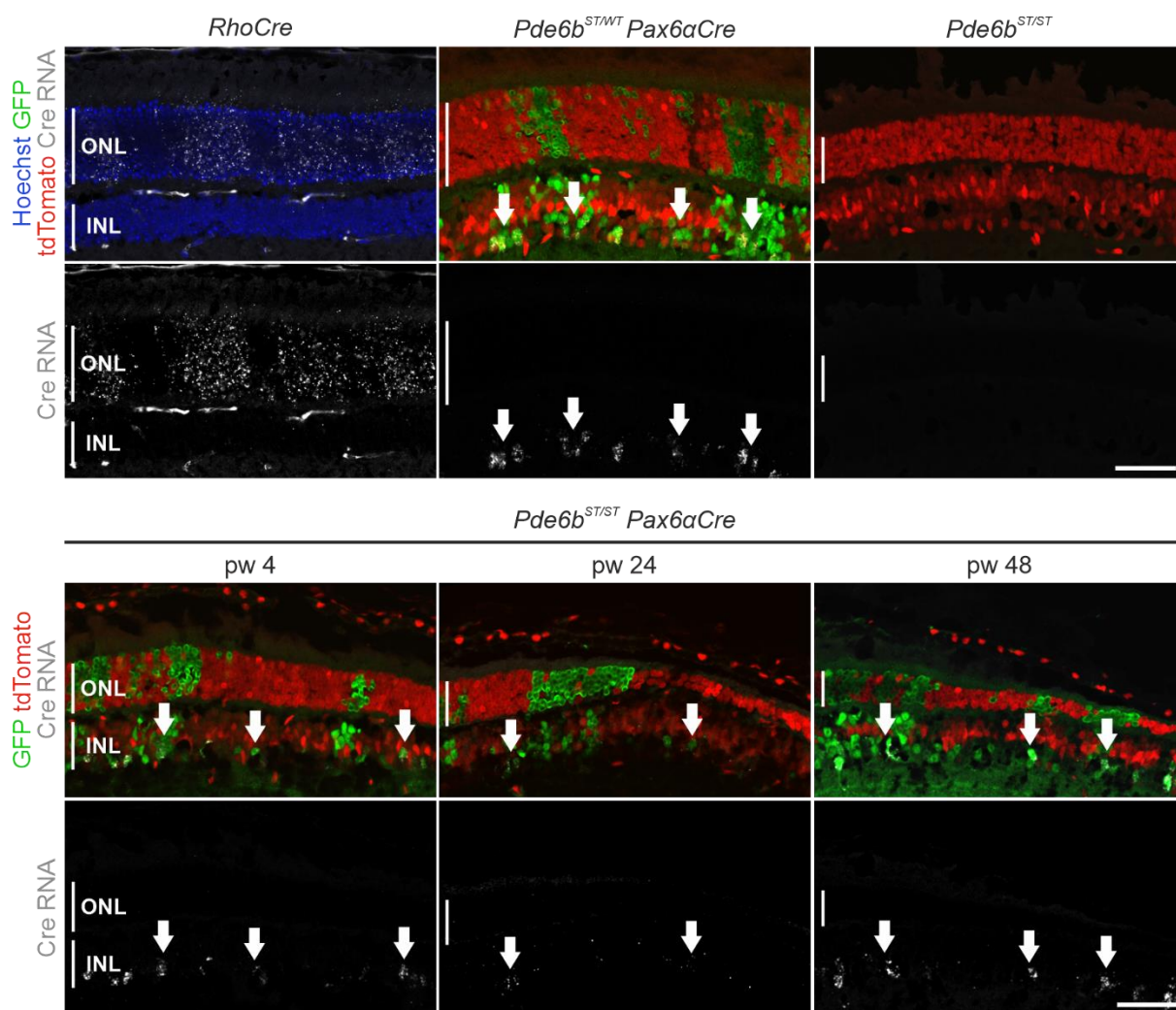


Figure 23: Absence of Pax6αCre recombinase RNA in the outer nuclear layer.

One *RhoCre* mouse was analyzed at 10 weeks of age as positive control. *Pde6b^{ST/WT} Pax6αCre ROSA^{nT-nG}* and *Pde6b^{ST/ST}* mice were analyzed at 4 weeks of age and *Pde6b^{ST/ST} Pax6αCre ROSA^{nT-nG}* mice at 4, 24 or 48 weeks of age. Retinal sections were used for Cre recombinase fluorescence *in situ* hybridization with Hoechst 33342 counterstaining in *RhoCre* sections. In *ROSA^{nT-nG}* sections, tdTomato label displays Cre-negative nuclei, while labeling of Cre recombined areas was enhanced using anti-GFP. Shown are representative merged images of the GFP-tdTomato-transition areas near the optic nerve and corresponding Cre RNA single channels. The result demonstrates absence of Pax6αCre recombinase in the outer nuclear layer of all *Pde6b* mice, but appearance in single cells at the inner margin of the INL displaying probably amacrine cells. Arrowheads, Cre RNA containing nuclei. Vertical white bars, outer nuclear layer (ONL), inner nuclear layer (INL). Scale bar, 50 μm.

Further, isolated RNA from double-positive tdTomato and PDE6B FAC-sorted cells and from *Pde6b*^{ST/ST} retinal lysates was used to perform quantitative real-time PCR for Cre recombinase. As positive control for postnatal Cre recombinase expression retinal lysates from 4-weeks-old *Pde6g*^{CreERT2/WT} mice were used, that express a tamoxifen-inducible Cre recombinase under the *Pde6g* promoter [122]. All values were normalized to the housekeeping gene β -Actin and further to *Pde6g*^{CreERT2/WT} control values. Cre recombinase RNA was found in *Pde6g*^{CreERT2/WT} lysates, while it was completely absent in all other samples (**Fig. 24**).

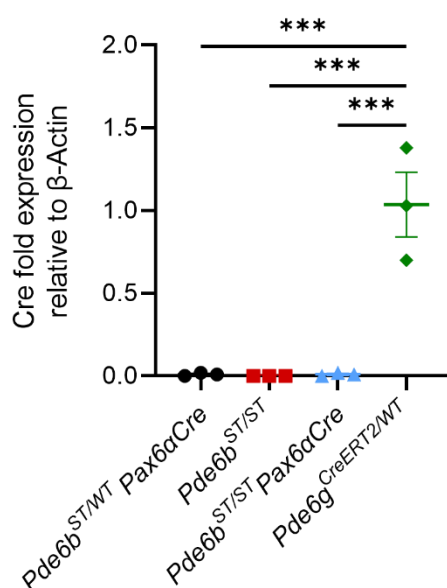


Figure 24: Absence of Pax6 α Cre recombinase RNA in FAC-sorted cells.

Pde6b^{ST/WT} Pax6 α Cre ROSA^{nT-nG} and *Pde6b*^{ST/ST} Pax6 α Cre ROSA^{nT-nG} mice were analyzed at 24 weeks of age. Retinas were digested with Papain and cells were stained with anti-GFP and anti-PDE6B. PDE6B and tdTomato double-positive photoreceptors were isolated by FAC-sorting. Retinas from 4-weeks-old *Pde6b*^{ST/ST} (negative control) and 4-weeks-old *Pde6g*^{CreERT2/WT} (positive control) mice were used without sorting. RNA of all samples was isolated and used for quantitative real-time PCR of Cre recombinase. Results were normalized to β -Actin and *Pde6g*^{CreERT2/WT} values. RNA of Cre recombinase was only found in *Pde6g*^{CreERT2/WT} positive control mice and was absent in all *Pde6b* samples. Circles, squares, triangles and diamonds, individual mice. Data are presented as mean \pm SEM. Tukey's test for multiple comparisons. *** $P < 0.001$.

4.1.6 Indications for genetic heterogeneity of *Pde6b* after partial rescue

In the next step, it was investigated whether the STOP cassette of PDE6B and tdTomato double-positive photoreceptors was removed resulting in RNA transcription. To do so, isolated DNA from FAC-sorted cells of 24-weeks-old *Pde6b*^{ST/WT} *Pax6αCre* *ROSA*^{nT-nG} and *Pde6b*^{ST/ST} *Pax6αCre* *ROSA*^{nT-nG} mice was used to perform PCR of *Pde6b*. In *Pde6b*^{ST/WT} *Pax6αCre* *ROSA*^{nT-nG} samples, both *Pde6b* wildtype 284 bp and mutant 415 bp bands were present, but they also showed faint recombinant 362 bp bands (**Fig. 25A**). Further, isolated DNA from *Pde6b*^{ST/ST} retinal lysates was used as control. The mutant *Pde6b* band was found in all three replicates of *Pde6b*^{ST/ST} mice. In *Pde6b*^{ST/ST} *Pax6αCre* *ROSA*^{nT-nG} samples, both the mutant and recombinant bands were present at a similar intensity.

To investigate if the recombinant band is present due to FAC-sorting contamination with GFP-positive cells, two mice were used as additional controls. First, one *Pde6b*^{ST/WT} *ROSA*^{nT-nG} mouse was used for sorting of tdTomato and PDE6B double-positive cells. As expected, the *Pde6b* PCR shows one mutant and one wildtype band with similar intensity (**Fig. 25B**). In addition, one *Pde6b*^{ST/ST} *Pax6αCre* *ROSA*^{nT-nG} mouse was used for sorting of GFP and PDE6B double-positive cells. In this case, the result shows the recombinant *Pde6b* band without any additional mutant band. However, a faint band on the same height as the *Pde6b* wildtype band was present, which reflects an unspecific amplification due to higher number of cycles during the PCR.

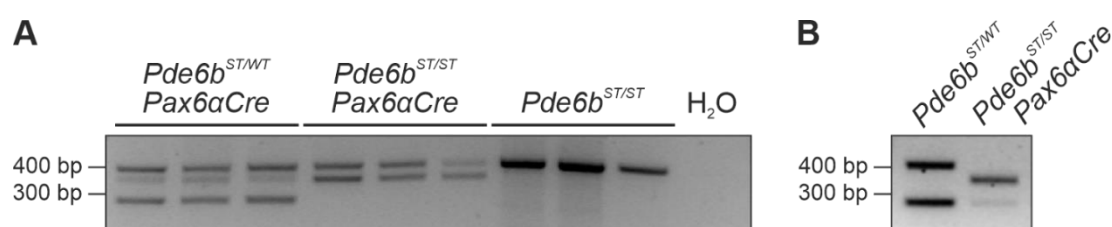


Figure 25: Genetic heterogeneity of *Pde6b* in FAC-sorted cells.

Pde6b^{ST/WT} *Pax6αCre* *ROSA*^{nT-nG}, *Pde6b*^{ST/ST} *Pax6αCre* *ROSA*^{nT-nG} and *Pde6b*^{ST/WT} *ROSA*^{nT-nG} mice were analyzed at 24 weeks of age. Retinas were digested with Papain. Cells were stained with anti-GFP and anti-PDE6B. **(A)** Rescued photoreceptors were isolated by FAC-sorting of double-positive cells for tdTomato and PDE6B. Retinas from 4-weeks-old *Pde6b*^{ST/ST} mice were used without sorting as negative control. DNA of all samples was isolated and used for PCR of *Pde6b*. PCR results were separated by agarose gel electrophoresis and showed the presence of the recombinant *Pde6b* band additional to the *Pde6b* mutant band in *Pax6αCre* mice. **(B)** As FAC-sorting controls, double tdTomato- and PDE6B-positive cells from one *Pde6b*^{ST/WT} *ROSA*^{nT-nG} mouse and double GFP- and PDE6B-positive cells from one *Pde6b*^{ST/ST} *Pax6αCre* *ROSA*^{nT-nG} mouse were isolated by FAC-sorting. DNA was isolated and used for PCR of *Pde6b*. PCR products were separated by agarose gel electrophoresis. The result demonstrates a clean FAC-sorting due to absence of the *Pde6b* mutant band in *Pde6b*^{ST/ST} *Pax6αCre* *ROSA*^{nT-nG} cells.

4.2 Effect of partial rescue on retinal remodeling

As a consequence of photoreceptor loss in RP, remodeling of the inner retina gets triggered, which might also impact the success of applied therapies. These changes affect inner retinal cells but also the retinal vasculature and RPE cells.

4.2.1 Restoration of visual function after partial rescue

To measure the effect of partial rescue on retinal function, full-field single-flash ERG responses were recorded in 40-weeks-old *Pde6b^{ST/WT}*, *Pde6b^{ST/ST}* and *Pde6b^{ST/ST} Pax6 α Cre* mice. The emitted signal consists of a negative a-wave reflecting photoreceptor responses and a positive b-wave, which is generated by the response of bipolar cells [131].

First, measurements in the scotopic range with a luminance of $\leq 2.0 \log(\text{cd}^*\text{s}/\text{m}^2)$, where only rods are activated [132], were performed. At these light intensities, an overall low a-wave response was recorded in all groups (**Fig. 26A,C**). Responses from *Pde6b^{ST/ST} Pax6 α Cre* mice were analogous to the ones of *Pde6b^{ST/ST}* mice, but both were not significantly different to *Pde6b^{ST/WT}* results. After, both rod and cone activation were determined in the mesopic range. Emitted signals in both the a- and b-wave revealed that *Pde6b^{ST/ST}* retinal potentials were rarely induced as light-sensitive outer segments are already completely degenerated (**Fig. 26**). On the other hand, *Pde6b^{ST/WT}* retinas showed a continuous increase in a- and b-wave amplitudes. The a-wave responses from *Pde6b^{ST/ST} Pax6 α Cre* mice did also rise with higher intensities, but not as much as the ones from *Pde6b^{ST/WT}* mice leading to a significant lower amplitude at luminances of $\geq 0.5 \log(\text{cd}^*\text{s}/\text{m}^2)$ (**Fig. 26A,C**). In contrast, b-wave amplitudes increased in parallel to the ones from *Pde6b^{ST/WT}* mice without significant difference at any timepoint (**Fig. 26B,C**).

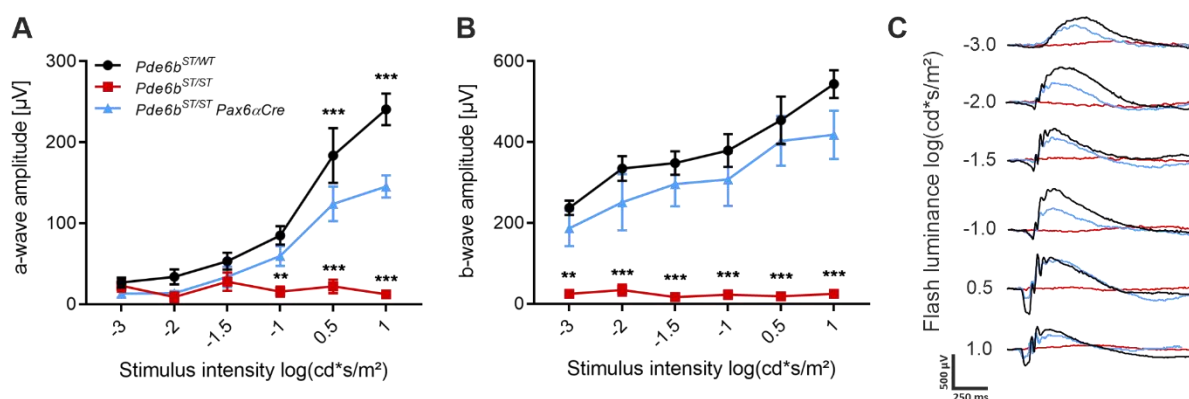


Figure 26: Partial rescue of scotopic and mesopic retinal function in *Pde6b*^{ST/ST} *Pax6αCre* mice.

Full-field single-flash ERGs were recorded in 40-weeks-old *Pde6b*^{ST/WT}, *Pde6b*^{ST/ST} and *Pde6b*^{ST/ST} *Pax6αCre* mice. Scotopic and mesopic (A) a-wave and (B) b-wave amplitudes. In *Pde6b*^{ST/ST} *Pax6αCre* mice, responses were comparable to *Pde6b*^{ST/WT} mice for both a- and b-wave except for luminances of ≥ 0.5 log (cd*s/m²) under mesopic conditions, where a-wave responses were significantly lower. Data are presented as mean \pm SEM. Tukey's test for multiple comparisons. ** $P \leq 0.01$; *** $P \leq 0.001$. (C) Representative responses from a single retina in the scotopic and mesopic range. It visualizes that a- and b-wave responses in *Pde6b*^{ST/ST} *Pax6αCre* mice were almost as high as in control *Pde6b*^{ST/WT} mice. Curves, individual mice.

Further, functionality of cones was examined by photopic ERG measurements. To do so, mice were light-adapted with a rod-desensitizing background and b-wave amplitudes were quantified. Again, retinal potentials in *Pde6b*^{ST/WT} and *Pde6b*^{ST/ST} *Pax6αCre* mice increased with higher light intensities (Fig. 27). In contrast to scotopic and mesopic measurements, the cone-mediated responses of partially rescued mice were indistinguishable from control mice. *Pde6b*^{ST/ST} mice lacked the b-wave and thus their responses were significantly lower compared to *Pde6b*^{ST/WT} mice at luminances of ≥ 0.5 log (cd*s/m²).

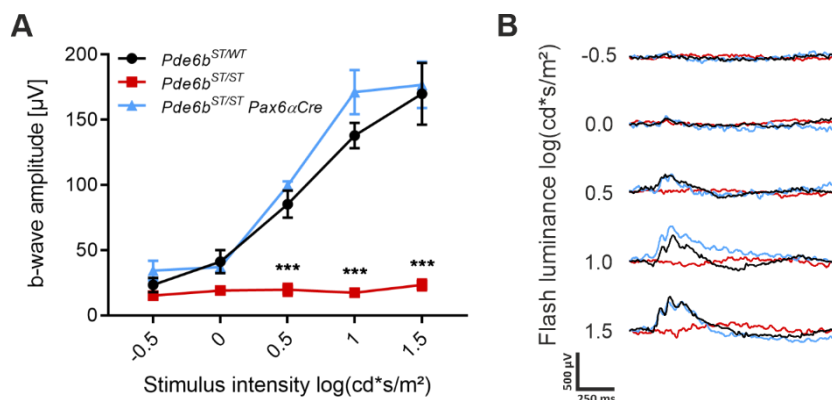


Figure 27: Rescue of photopic retinal function in *Pde6b*^{ST/ST} *Pax6αCre* mice.

Full-field single-flash ERGs were recorded in 40-week-old *Pde6b*^{ST/WT}, *Pde6b*^{ST/ST} and *Pde6b*^{ST/ST} *Pax6αCre* mice. **(A)** Photopic b-wave amplitudes. No response could be measured in *Pde6b*^{ST/ST} mice, while *Pde6b*^{ST/ST} *Pax6αCre* mice were indistinguishable from control *Pde6b*^{ST/WT} mice. Data are presented as mean ± SEM. Tukey's test for multiple comparisons. *** $P \leq 0.001$. **(B)** Representative responses from a single retina in the photopic range. It visualizes that b-wave responses in *Pde6b*^{ST/ST} *Pax6αCre* mice were comparable to control *Pde6b*^{ST/WT} mice. Curves, individual mice.

4.2.2 Partial preservation of central bipolar and horizontal cell dendrites after partial rescue

To evaluate the effect of partial rescue of photoreceptors on inner retinal cells, sections of 48-week-old *Pde6b*^{ST/WT} *Pax6αCre* *ROSA*^{nT-nG}, *Pde6b*^{ST/ST} *ROSA*^{nT-nG} and *Pde6b*^{ST/ST} *Pax6αCre* *ROSA*^{nT-nG} mice were used. Rod bipolar cells, cone bipolar cells and horizontal cells were immunolabeled with antibodies for protein kinase C alpha (PKCα), secretogin (SCGN) and Calbindin, respectively, as well as anti-GFP co-labeling. PKCα accelerates glutamate-driven signal transduction and termination [133], while SCGN and Calbindin are calcium-binding proteins responsible for calcium transport [134,135]. Control *Pde6b*^{ST/WT} mice demonstrated a healthy morphology of all three types of second order neurons characterized by dendritic sprouting that covers the whole outer plexiform layer and enables connection to all photoreceptors (**Fig. 28**). In *Pde6b*^{ST/ST} retinas, most rod and cone bipolar cell dendrites had disappeared, while horizontal cell processes also underwent dramatic retraction, although they were not completely degenerated.

Interestingly, *Pde6b*^{ST/ST} *Pax6αCre* sections showed a healthy morphology of rod bipolar cells, cone bipolar cells and horizontal cells if more than three rows of nuclei were left in the outer nuclear layer. In closer proximity to the optic nerve, where approximately two photoreceptor nuclei layers were left, dendrites of second order neurons showed a slight retraction. In regions with even less survived photoreceptors, the morphology of rod bipolar cells, cone bipolar cells and horizontal cells was comparable to *Pde6b*^{ST/ST} retinas along with thinning of the outer plexiform layer.

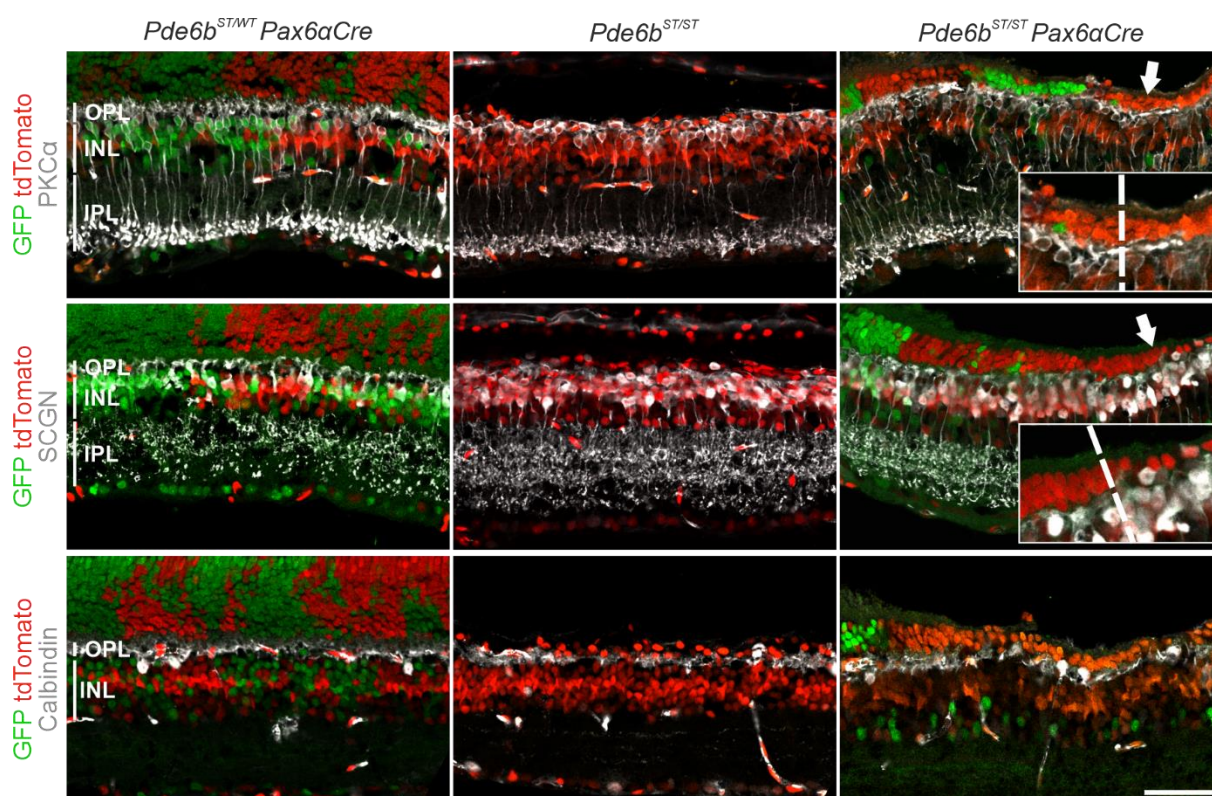


Figure 28: Partial preservation of central bipolar and horizontal cell dendrites.

Pde6b^{ST/WT} *Pax6αCre* *ROSA*^{nT-nG}, *Pde6b*^{ST/ST} *ROSA*^{nT-nG} and *Pde6b*^{ST/ST} *Pax6αCre* *ROSA*^{nT-nG} mice were analyzed at 48 weeks of age. Label of tdTomato displays Cre-negative nuclei, while labeling of Cre recombined areas was enhanced using anti-GFP. Rod bipolar cells, cone bipolar cells and horizontal cells were co-labeled using anti-PKCα, anti-SCGN and anti-Calbindin, respectively. Shown are representative images of the GFP-tdTomato-transition area. The results demonstrate preservation of cell dendrites in rescued regions when approximately more than three rows of photoreceptor nuclei are left in the outer nuclear layer. Vertical white bars, outer plexiform layer (OPL), inner nuclear layer (INL) and inner plexiform layer (IPL). Arrowheads and dashed lines, beginning of dendrite retraction. Scale bar, 50 μm.

4.2.3 Partial rescue of photoreceptors prevents blood vessel remodeling

Although RP is primarily affecting photoreceptors, it has also been associated with structural changes of the retinal vasculature [50,51,122]. To investigate vascular abnormalities, retinal flatmounts were stained with an endothelial cell marker isolectin GS-IB4. Peripheral images of *Pde6b^{ST/ST} Pax6 α Cre* mice were taken on the temporal side of the flatmount, as Pax6 α Cre recombinase is always expressed in this region, while central images were taken in close proximity to the optic nerve.

For analysis, the deep and intermediate vascular plexus (DVP + IVP) were merged. The third layer of the interconnected retinal vascular network, the superficial vascular plexus (SVP), was analyzed separately. In 48-weeks-old *Pde6b^{ST/WT}* and *Pde6b^{ST/ST} Pax6 α Cre* as well as in 4-weeks-old *Pde6b^{ST/ST}* mice, retinal capillaries showed a normal morphology with similar diameter among individual vessels both in central and peripheral regions (**Fig. 29A**). At 24 weeks of age, *Pde6b^{ST/ST}* mice then demonstrated a large proportion of thinner vessels whereby the effect seemed to be stronger in the center compared to the periphery. By 48 weeks of age, the substantial vascular remodeling was even more visible as the majority of capillaries became thin or was already lost. To quantify the vascular degenerative changes, isolectin GS-IB4 stained vessels were analyzed with AngioTool. In central areas, no significant difference in the vessel area of *Pde6b^{ST/ST} Pax6 α Cre* mice compared to *Pde6b^{ST/WT}* was displayed at any timepoint, although the area was 4% smaller at 24 and 48 weeks of age (**Fig. 29B**). On the other hand, *Pde6b^{ST/ST}* mice exhibited an almost linear reduction in their central vessel area over time. In 24-weeks-old mice, the vessel area was already 4% lower than in *Pde6b^{ST/WT}* mice and at 48 weeks of age there was a significant decrease by 11%. In the periphery, *Pde6b^{ST/WT}* and *Pde6b^{ST/ST} Pax6 α Cre* mice were indistinguishable (**Fig. 29C**). The vessel area in *Pde6b^{ST/ST}* retinas was only 1% lower compared to *Pde6b^{ST/WT}* at 4 and 24 weeks of age but showed a significant reduction of 9% at 48 weeks of age.

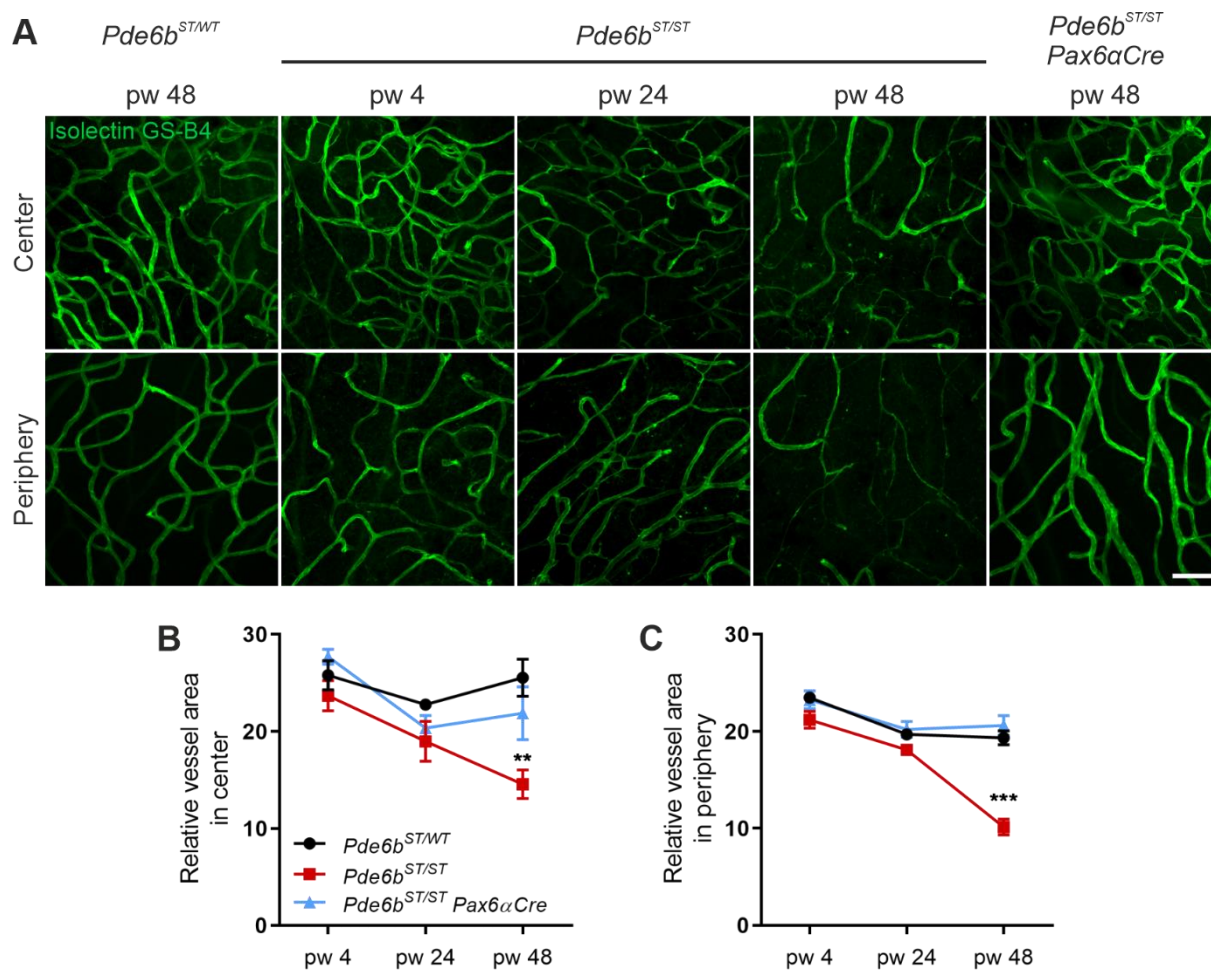


Figure 29: Rescue of morphological abnormalities in the deep and intermediate vascular plexi.

(A) *Pde6b*^{ST/WT} and *Pde6b*^{ST/ST} *Pax6αCre* mice were analyzed at 48 weeks of age, *Pde6b*^{ST/ST} mice at 4, 24 or 48 weeks of age. Retinal flatmounts were stained with isolectin GS-IB4. Shown are the maximum intensity projection representative images of the merged deep and intermediate plexus (DVP + IVP) in the center and periphery. It demonstrates progressive blood vessel degeneration in *Pde6b*^{ST/ST} over time, while the retinal vasculature of *Pde6b*^{ST/ST} *Pax6αCre* mice shows a healthy morphology. Scale bar, 50 μm. Isolectin GS-IB4 immunolabeling of DVP + IVP in retinal flatmounts in **(B)** center and **(C)** periphery were analyzed using AngioTool. Results confirm an almost linear decrease in blood vessel area in *Pde6b*^{ST/ST} retinas, whereas the blood vessel area of *Pde6b*^{ST/ST} *Pax6αCre* mice was comparable to *Pde6b*^{ST/WT} mice. Data are presented as mean ± SEM. Tukey's test for multiple comparisons. ** $P = 0.002$; *** $P < 0.001$.

In contrast to the DVP and IVP, the SVP is composed of larger vessels. It is located in the ganglion cell layer and is directly supplied by the central retinal artery. In 48-weeks-old *Pde6b*^{ST/WT}, *Pde6b*^{ST/ST} and *Pde6b*^{ST/ST} *Pax6αCre* mice, no distinction in vessel area could be made (**Fig. 30A**), which was confirmed by AngioTool quantification (**Fig. 30B**). The analysis demonstrated a superficial vessel area of 15-20% ± SEM. In addition, the vascular morphology in *Pde6b*^{ST/WT} mice and peripheral regions of *Pde6b*^{ST/ST} *Pax6αCre* mice showed no discrepancies. However, in 48-weeks-old *Pde6b*^{ST/ST} mice, as well as in some central regions of *Pde6b*^{ST/ST} *Pax6αCre* mice, tortuous vessels could be found (**Fig. 30A**, filled arrowheads). Furthermore, some acellular vessels were discovered, mainly in the retinal periphery of *Pde6b*^{ST/ST} mice (**Fig. 30A**, empty arrowhead).

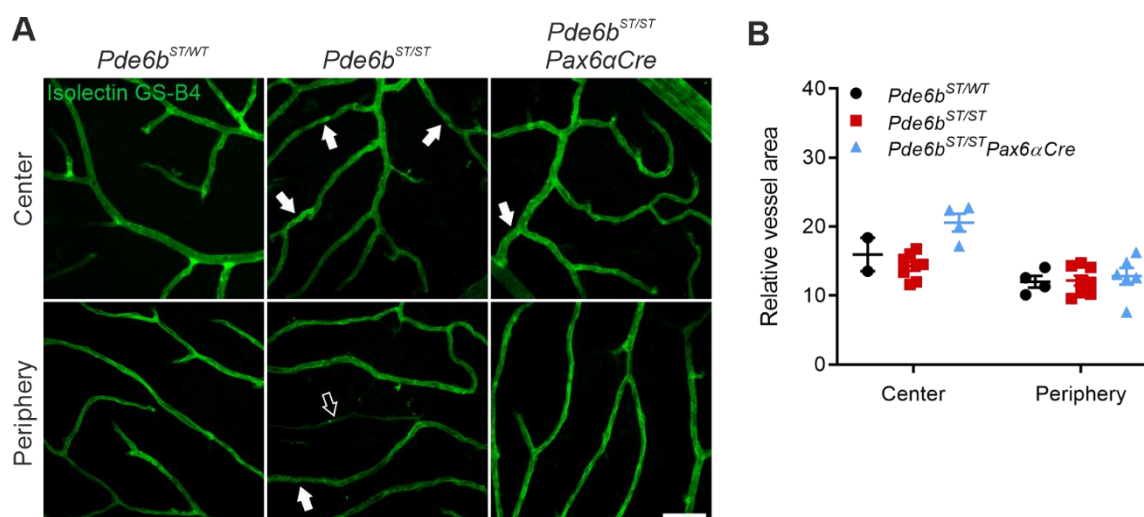


Figure 30: Rescue of morphological abnormalities in the superficial vascular plexus.

(A) *Pde6b*^{ST/WT}, *Pde6b*^{ST/ST} and *Pde6b*^{ST/ST} *Pax6αCre* mice were analyzed at 48 weeks of age. Retinal flatmounts were stained with isolectin GS-IB4. Shown are the maximum intensity projection representative images of the superficial vascular plexus (SVP) in the center and periphery. Filled arrowheads, tortuous vessels; empty arrowhead, acellular vessel. Scale bar, 50 μm. **(B)** Isolectin GS-IB4 immunolabeling of SVP in retinal flatmounts in center and periphery were analyzed using AngioTool. Results demonstrate morphological abnormalities in *Pde6b*^{ST/ST} retinas without reduction of blood vessel area. Circles, squares and triangles, individual mice. Data are presented as mean ± SEM. Tukey's test for multiple comparisons.

The formation of acellular vessels is another characteristic feature of vasculature remodeling and loss of function, as they are composed of remaining basement membranes from dying endothelial cells [136]. For the assessment of acellular vessels, isolated retinas were digested with trypsin, H&E stained and quantified by counting. For this assay, no distinction between the different vascular plexi was made. In *Pde6b^{ST/WT}* mice, only a few acellular vessels were present at all investigated timepoints (**Fig. 31**). At 4 weeks of age, the amount in *Pde6b^{ST/ST}* and *Pde6b^{ST/ST} Pax6αCre* mice was comparable to *Pde6b^{ST/WT}* mice, which was about $10 \pm \text{SEM}$ and $15 \pm \text{SEM}$ acellular vessels per scan field in center and periphery, respectively (**Fig. 31B,C**). In *Pde6b^{ST/ST}* mice, a strong increase in the number of acellular vessels was observed at the age of 24 weeks by demonstrating $75 \pm \text{SEM}$ in the center and $60 \pm \text{SEM}$ in the periphery. In 48-week-old *Pde6b^{ST/ST}* mice, the number then slightly decreased in the center to $60 \pm \text{SEM}$ acellular vessels, while it remained constant in the periphery. On the other hand, the vasculature of 24-week-old *Pde6b^{ST/ST} Pax6αCre* mice displayed $25 \pm \text{SEM}$ acellular vessels in the center, which is a slight increase compared to samples at 4 weeks of age and also significantly higher compared to *Pde6b^{ST/WT}* mice. At 48 weeks of age, the number was reduced again and comparable to *Pde6b^{ST/WT}* mice. In contrast, the number of acellular vessels in the periphery remained comparable to the one of *Pde6b^{ST/WT}* mice at all investigated timepoints.

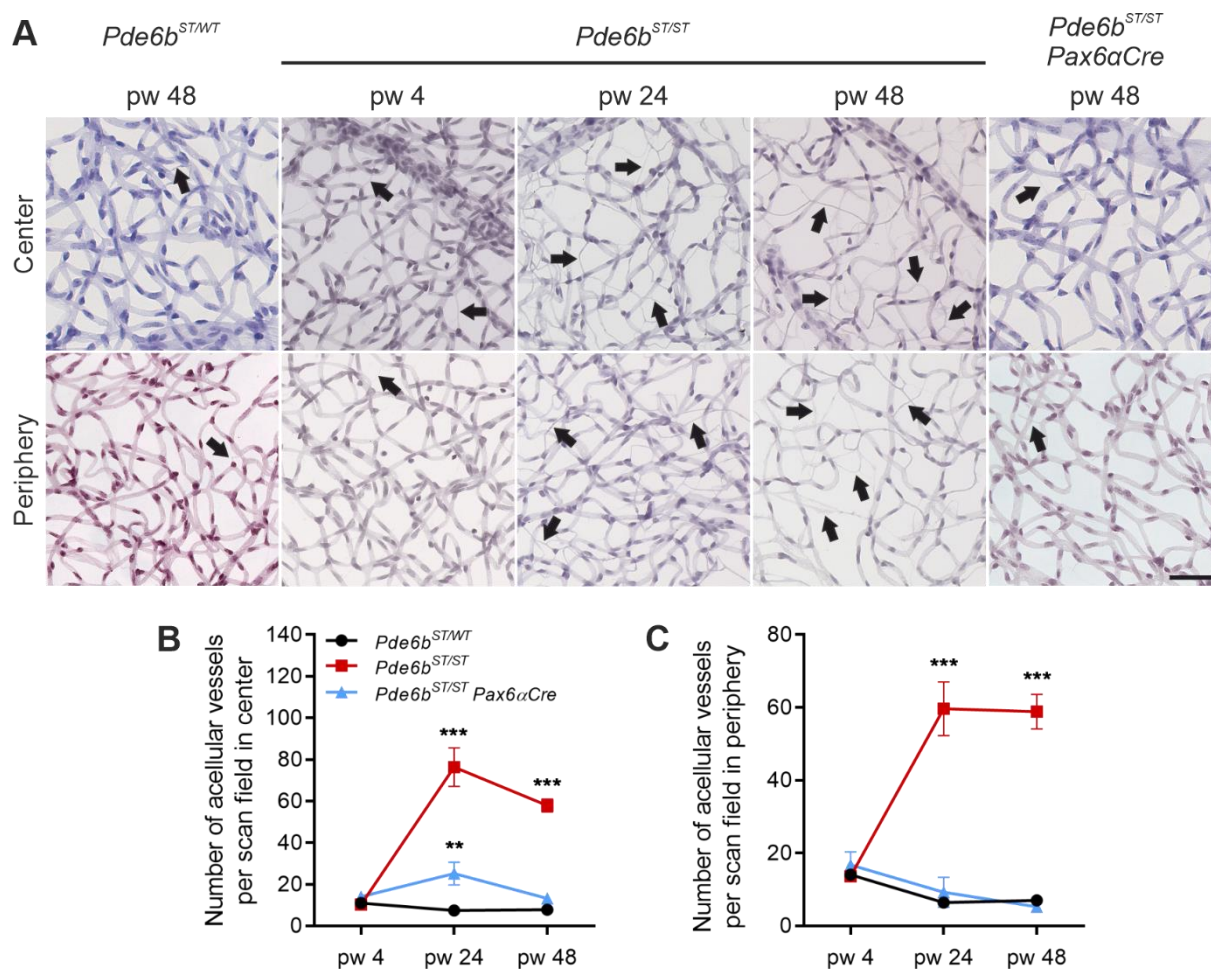


Figure 31: Rescue of acellular capillaries in *Pde6b*^{ST/ST} *Pax6αCre* mice.

(A) *Pde6b*^{ST/WT} and *Pde6b*^{ST/ST} *Pax6αCre* mice were analyzed at 48 weeks of age, *Pde6b*^{ST/ST} mice at 4, 24 or 48 weeks of age. Retinal flatmounts were digested with trypsin and H&E stained. Shown are representative images of the vasculature in the center or periphery. It demonstrates a progressive increase in the acellular vessel number in *Pde6b*^{ST/ST} mice, while the retinal vasculature of *Pde6b*^{ST/ST} *Pax6αCre* mice shows a healthy morphology both in center and periphery. Arrowheads, acellular vessels. Scale bar, 50 μm. Number of acellular vessels per scan field was analyzed in **(B)** center and **(C)** periphery. In both regions, results confirm a strong increase in the number of acellular vessels in *Pde6b*^{ST/ST} retinas, whereas the number of acellular vessels in *Pde6b*^{ST/ST} *Pax6αCre* mice was comparable to *Pde6b*^{ST/WT} mice. Data are presented as mean ± SEM. Tukey's test for multiple comparisons. ** $P = 0.002$; *** $P < 0.001$.

4.2.4 Rescue of peripheral photoreceptors prevents overall RPE remodeling

As photoreceptors are in constant interaction with the RPE monolayer, their degeneration also influences RPE morphology and metabolism [42–46]. To first gain a basic understanding of RPE remodeling in 48-week-old *Pde6b*^{ST/ST} mice, we characterized RPE cell morphologies in RPE-choroid-sclera flatmounts. To do so, the retina was separated, RPE-choroid-sclera flatmounts were bleached and RPE cell adhesions immunolabeled with β -Catenin, which is required for the structural integrity and functional polarization of epithelial cells [137]. Imaging revealed the distinction between four different morphological regions (**Fig. 32**). Around the optic nerve, RPE cells were completely absent most likely due to cell death. Then, an area of small abnormal, specifically wavy and elongated, cells was found. In the intermediate region, a small circular stripe of RPE cells with healthy hexagonal morphology was present. In the periphery, RPE cells turned out to be big and roundish.

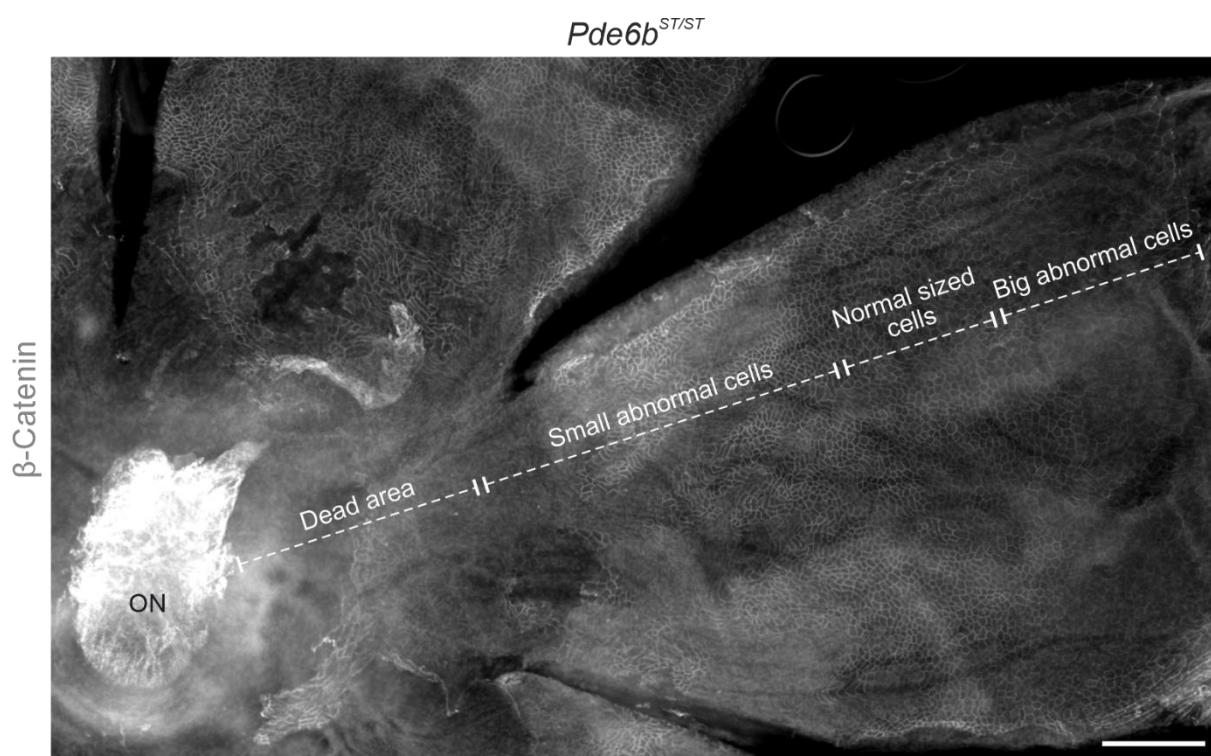


Figure 32: RPE of *Pde6b*^{ST/ST} mice demonstrate four morphological regions.

Pde6b^{ST/ST} mice were analyzed at 48 weeks of age. RPE-choroid-sclera flatmounts were bleached and immunolabeled using anti- β -Catenin. Shown is a representative image of the RPE from the optic nerve (ON) to the periphery. Four morphological regions can be distinguished (dead area, small abnormal cells, normal sized cells and big abnormal cells). White dashed lines, length of regions. Scale bar, 250 μ m.

To determine if the size reduction of central RPE cells took place due to re-onset of mitosis, RPE-choroid-sclera flatmounts of 48-weeks-old *Pde6b^{ST/ST}* mice were immunolabeled with the cytoskeleton component α -Tubulin in addition to β -Catenin and counterstained using Hoechst 33342. As positive control for RPE cell proliferation, RPE-choroid-sclera flatmounts of postnatal day 0 (P0) *Pde6b^{ST/ST}* mice were used on their day of birth, as the RPE undergoes mitosis until P15 [138]. Mitotic cells were identified by α -Tubulin staining of mitotic spindles and exposed chromosomes in metaphase or anaphase labeled by Hoechst 33342 (**Fig. 33**, arrowheads). In the RPE of P0 mice, several mitotic cells were discovered, while in samples from 48-weeks-old mice no single proliferating RPE cell was found. In addition, the tubulin cytoskeleton was shown to be disrupted as the characteristic roundish shape was lost and only α -Tubulin-positive dots were left in the RPE cytoplasm.

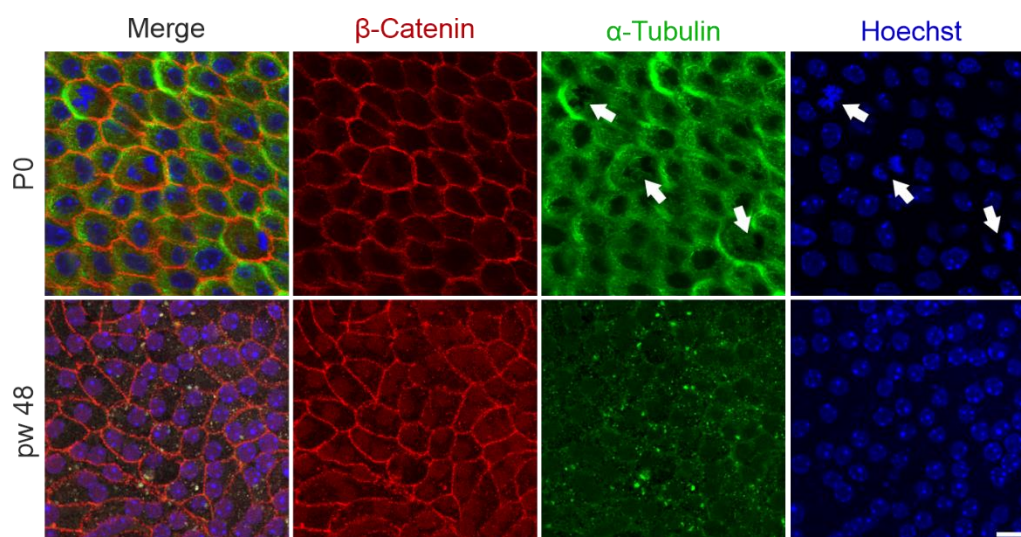


Figure 33: RPE cells from *Pde6b^{ST/ST}* mice do not show onset of mitosis but disrupted cytoskeleton. *Pde6b^{ST/ST}* mice were analyzed at day of birth (P0) or 48 weeks of age. RPE-choroid-sclera flatmounts were bleached and immunolabeled using anti- β -Catenin and anti- α -Tubulin with Hoechst 33342 counterstaining. Shown are the representative images of the central RPE. Mitotic cells were found in the RPE at P0, while no evidence of cell division was discovered in 48-weeks-old mice. Arrowheads, mitotic cells. Scale bar, 10 μ m.

Next, it was investigated how partial photoreceptor rescue influences RPE remodeling. To this purpose, RPE-choroid-sclera flatmounts of 48-weeks-old *Pde6b^{ST/WT}*, *Pde6b^{ST/ST} Pax6 α Cre* and 4-, 24- or 48-weeks-old *Pde6b^{ST/ST}* mice were immunolabeled with β -Catenin, counterstained with Hoechst 33342 and imaged close to the optic nerve in the center and in the periphery. Thereby, peripheral images of *Pde6b^{ST/ST} Pax6 α Cre* mice were taken on the temporal side of the flatmount, as *Pax6 α Cre* recombinase is always expressed in underlying photoreceptors of this region.

In both the central and peripheral area of *Pde6b^{ST/WT}* flatmounts, RPE cells displayed their characteristic hexagonal shape (**Fig. 34A**). A similar morphology was found in *Pde6b^{ST/ST}* mice at 4 weeks of age in both investigated regions, but at 24 weeks of age only in the center. At this timepoint, RPE cells were already slightly elongated in the periphery. Finally, in 48-weeks-old *Pde6b^{ST/ST}* mice, RPE cells in the center were shown to be small and elongated, while they were big and roundish in the periphery. Moreover, β -Catenin was notably dislocated from the cellular membrane to the cytoplasm both in center and periphery. In *Pde6b^{ST/ST} Pax6 α Cre* mice, RPE morphology was comparable to the one of *Pde6b^{ST/WT}* flatmounts in both regions.

Morphometric analysis of the RPE cells was then performed to quantify the changes in central and peripheral regions. First, *Pde6b^{ST/WT}* RPE cells demonstrated an average $400 \mu\text{m}^2 \pm \text{SEM}$ in central regions (**Fig. 34B,C**). In the periphery, RPE cell areas were slightly smaller ($350 \mu\text{m}^2 \pm \text{SEM}$ at 4 weeks of age and $470 \mu\text{m}^2 \pm \text{SEM}$ at 48 weeks of age, respectively). No differences in the RPE cell area between the different genotypes were observed in 4-week-old mice, neither in the center nor in the periphery. In 24-weeks-old mice, there was a slight but significant reduction to $335 \mu\text{m}^2 \pm \text{SEM}$ central RPE cell area in *Pde6b^{ST/ST}* flatmounts, while all groups displayed similar cell areas in the periphery. RPE cells from 48-weeks-old *Pde6b^{ST/ST}* mice revealed a significant decrease to $140 \mu\text{m}^2 \pm \text{SEM}$ in the center and a significant increase to $640 \mu\text{m}^2 \pm \text{SEM}$ in the periphery. Moreover, the central RPE cell area was also significantly reduced to an average of $340 \mu\text{m}^2 \pm \text{SEM}$ in *Pde6b^{ST/ST} Pax6 α Cre*, but comparable to *Pde6b^{ST/WT}* in the temporal periphery.

In the next step, the RPE solidity, which demonstrates deviations from the hexagonal cell shape, in RPE-choroid-sclera flatmounts of 48-weeks-old mice was analyzed. In central areas, *Pde6b^{ST/WT}* mice presented a RPE cell solidity of $0.87 \pm \text{SEM}$ (**Fig. 34D**). In comparison, RPE cell solidities of *Pde6b^{ST/ST}* and *Pde6b^{ST/ST} Pax6 α Cre* mice tended to be slightly lower with $0.835 \pm \text{SEM}$ and $0.845 \pm \text{SEM}$, respectively. In the RPE periphery, cell solidity of *Pde6b^{ST/WT}* mice was $0.9 \pm \text{SEM}$. In contrast, *Pde6b^{ST/ST}* mice demonstrated a RPE cell solidity of $0.83 \pm \text{SEM}$, which was significantly lower. The solidity of *Pde6b^{ST/ST} Pax6 α Cre* RPE cells tended to be slightly higher with $0.92 \pm \text{SEM}$ compared to *Pde6b^{ST/WT}* mice.

Last but not least, the RPE eccentricity, which reflects their elongation, was evaluated. In RPE center and periphery, *Pde6b^{ST/WT}* mice presented a cell eccentricity of $0.64 \pm \text{SEM}$ and $0.65 \pm \text{SEM}$, respectively (**Fig. 34E**). In both regions, *Pde6b^{ST/ST}* mice demonstrated significantly higher RPE eccentricities with $0.82 \pm \text{SEM}$ in central and $0.8 \pm \text{SEM}$ in peripheral regions. On the other hand, *Pde6b^{ST/ST} Pax6 α Cre* RPE cells were only slightly increased in the center by showing a eccentricity of $0.68 \pm \text{SEM}$. In their periphery, RPE eccentricity was $0.64 \pm \text{SEM}$ and thus comparable to *Pde6b^{ST/WT}* mice.

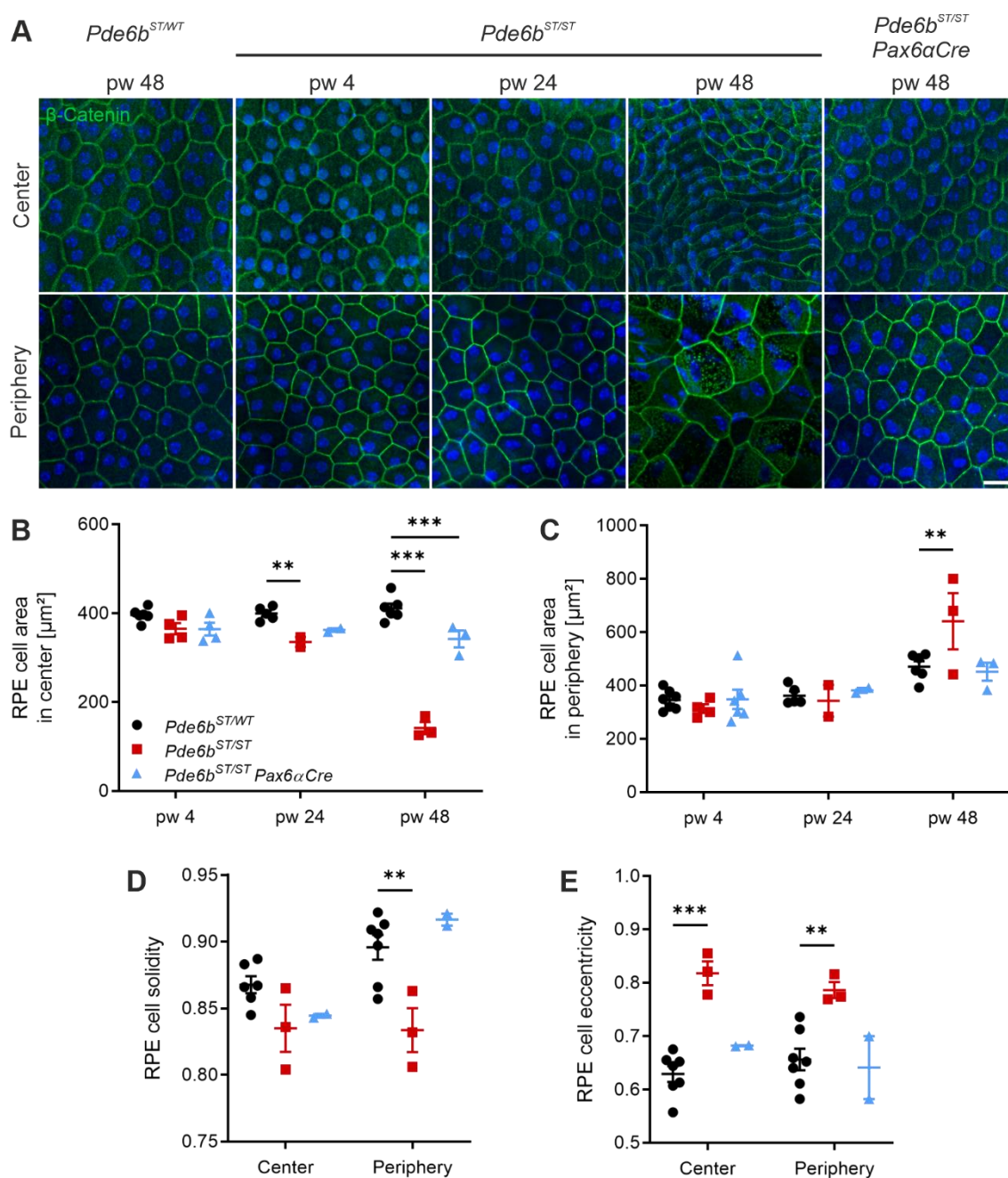


Figure 34: Rescue of morphological abnormalities in the RPE.

(A) *Pde6b*^{ST/WT} and *Pde6b*^{ST/ST} *Pax6αCre* mice were analyzed at 48 weeks of age, *Pde6b*^{ST/ST} mice at 4, 24 or 48 weeks of age. RPE-choroid-sclera flatmounts were bleached and immunolabeled using anti- β -Catenin with Hoechst 33342 counterstaining. Shown are representative images of the RPE in the center or periphery. Scale bar, 50 μm . RPE cell area was quantified in (B) center and (C) periphery using CellProfiler. Analysis of (D) RPE cell solidity and (E) RPE cell eccentricity in 48-weeks-old mice with CellProfiler. Results demonstrate morphological abnormalities in 48-weeks-old *Pde6b*^{ST/ST} RPE, whereas no disparities were found in both regions of *Pde6b*^{ST/ST} *Pax6αCre* mice. Circles, squares and triangles, individual mice. Data are presented as mean \pm SEM. Tukey's test for multiple comparisons. ** $P \leq 0.008$; *** $P < 0.001$.

4.3 Horizontal material transfer via small EVs

As Pax6 α Cre recombinase seems to be not expressed in adult photoreceptors, we assumed horizontal material transfer from recombined photoreceptors to mutant photoreceptors as underlying reason for PDE6B expression in tdTomato-positive cells. To investigate this hypothesis, retinal small EVs were evaluated as they have the ability to transport cargo over longer distances [139].

4.3.1 Characterization of isolated small EVs

For the isolation of small EVs, mice were used at 10 weeks of age. At this timepoint, some tdTomato-positive photoreceptors did already show PDE6B expression, while PDE6B-negative ones were mostly not degenerated yet. To characterize isolated small EVs from *Pde6b*^{ST/WT}, *Pde6b*^{ST/ST} and *Pde6b*^{ST/ST} *Pax6 α Cre* mice, they were analyzed via nanoparticle tracking analysis and immunoblotting. The results revealed that the majority of the isolated particles in all groups had a diameter of less than 180 nm (**Fig. 35A**). As control, it was shown that there was a comparable amount of total small EVs per sample between the three different groups (**Fig. 35B**). Moreover, analysis of the mode size, which is the most common size within the sample, demonstrated a similar size of 95-100 $\mu\text{m} \pm \text{SEM}$ in all groups (**Fig. 35C**). Isolated small EVs were further analyzed via immunoblotting for ALIX, which is part of the exosomal ESCRT machinery. One *Pde6b*^{ST/WT} retinal lysate was used as positive control showing expression of ALIX after low exposure (**Fig. 35D**). Isolated small EVs further demonstrated ALIX expression after longer exposure due to low protein levels.

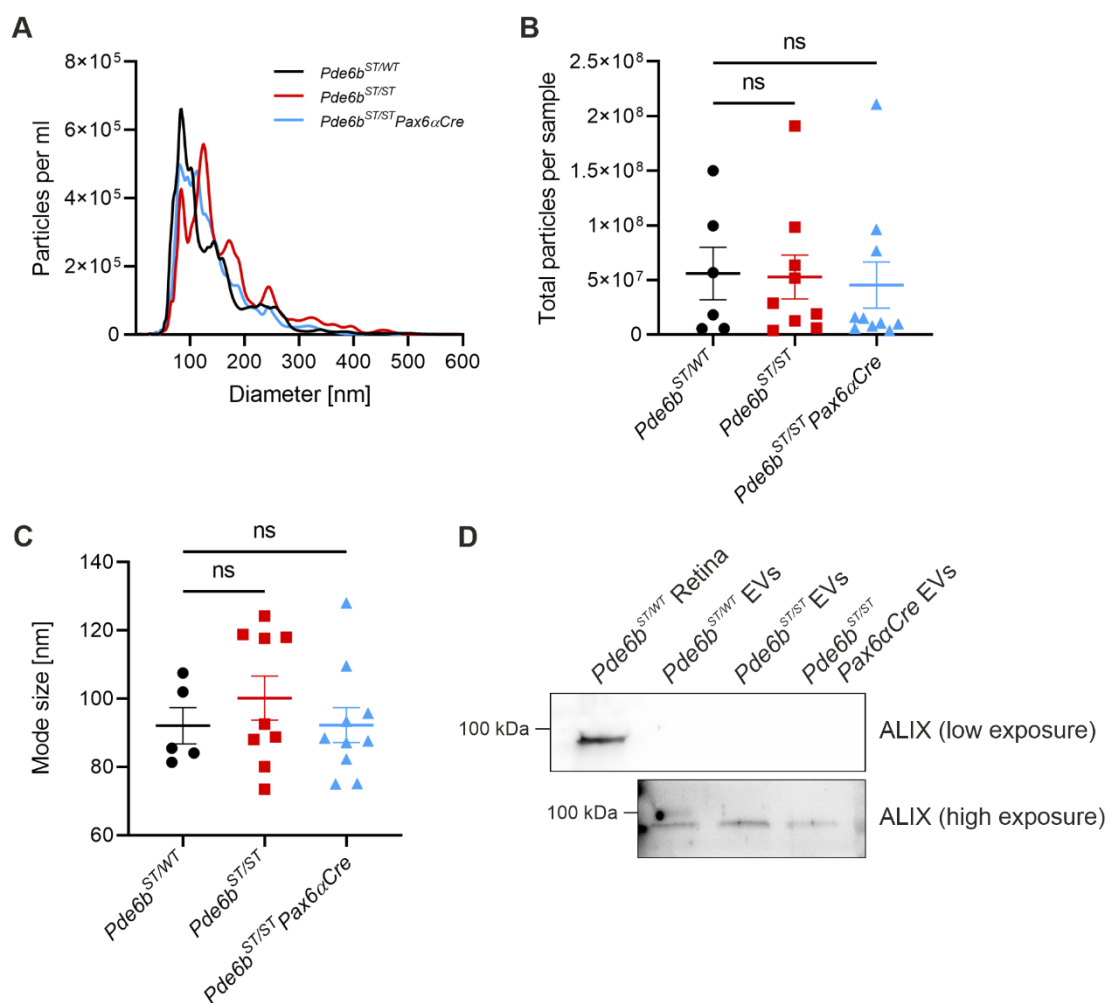


Figure 35: Nanoparticle tracking analysis and immunoblotting of isolated small EVs.

Pde6b^{ST/WT}, *Pde6b*^{ST/ST} and *Pde6b*^{ST/ST} Pax6αCre mice were analyzed at 10 weeks of age. Small extracellular vesicles (EVs) were isolated from both retinas per mouse and analyzed via (A-C) nanoparticle tracking analysis or (D) immunoblotting by pooling samples from three mice of the same genotype. **(A)** Representative graphs showing the number of small EVs with corresponding size per sample. **(B)** Number of total small EVs per sample. **(C)** Mode size (most common size) of isolated small EVs per sample. Results demonstrate no discrepancies in the number of particles and mode size between isolated small EVs from different genotypes. Curves, circles, squares and triangles, individual mice. Data are presented as mean ± SEM. Tukey's test for multiple comparisons. ns, not significant. **(D)** Immunoblotting of one *Pde6b*^{ST/WT} retinal lysate (positive control) and isolated small EVs shows presence of ALIX in all samples.

4.3.2 Indications for transport of PDE6B protein, RNA and DNA

To investigate whether PDE6B protein might be packed into small EVs, biopsy punches of 10-weeks-old *Pde6b^{ST/ST} Pax6αCre* mice were analyzed by correlative light-electron microscopy, whereby PDE6B was labeled with immunogold. Rod outer segments were identified by gold particles in discs, which demonstrated only a few labeled PDE6B proteins (**Fig. 36** left). Inner segments were identified at the lower end of outer segments and basal bodies (**Fig. 36** right, white arrowhead). Compared to outer segments, inner segments did not display any discs or PDE6B immunogold labeling, which confirms specificity of labeling. Gold particles were found in both regions in different exocytosis stages of vesicle-like structures either close to the membrane or in the extracellular space between photoreceptors.

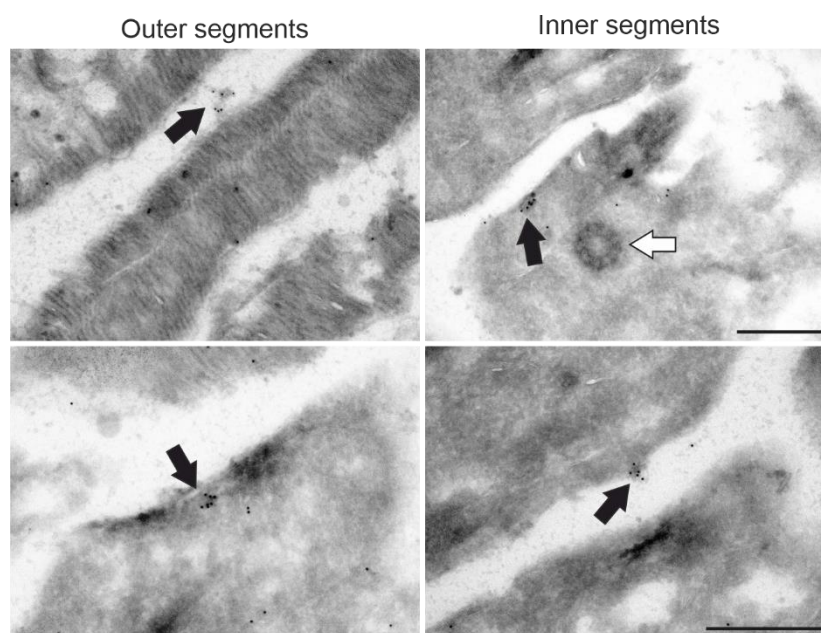


Figure 36: Light-electron microscopy of immunogold-labeled PDE6B in EVs.

Pde6b^{ST/ST} Pax6αCre mice were analyzed at 10 weeks of age. Biopsy punches of the central and temporal periphery of the eye were taken. Correlative light-electron microscopy was conducted with PDE6B immunogold labeling. Shown are representative images of the photoreceptor outer and inner segments. Results demonstrate accumulation of PDE6B in vesicle-like structures. Black arrowheads, PDE6B labeling in vesicle-like structures; white arrowhead, basal body. Scale bars, 500 nm.

For the evaluation of Pde6b RNA in isolated small EVs, vesicles from 10-weeks-old *Pde6b*^{ST/WT}, *Pde6b*^{ST/ST} and *Pde6b*^{ST/ST} *Pax6aCre* mice were directly used for quantitative real-time PCR. Results were normalized to *Pde6b*^{ST/WT} values and U6 non-coding small nuclear RNA (snRNA), which is a common housekeeping marker for small EVs [140]. It was shown that Pde6b RNA was completely absent in small EVs isolated from *Pde6b*^{ST/ST} mice, while its abundance in *Pde6b*^{ST/ST} *Pax6aCre* EVs was 75% ± SEM compared to *Pde6b*^{ST/WT} (Fig. 37).

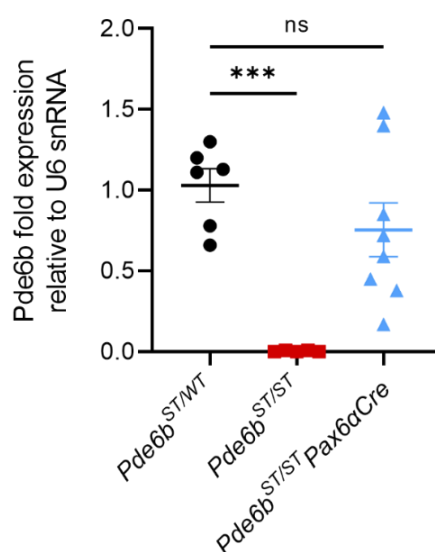


Figure 37: Pde6b RNA in isolated small EVs.

Pde6b^{ST/WT}, *Pde6b*^{ST/ST} and *Pde6b*^{ST/ST} *Pax6aCre* mice were analyzed at 10 weeks of age. Small extracellular vesicles (EVs) were isolated from both pooled retinas per mouse. RNA was purified and subsequently used for quantitative real-time PCR of Pde6b. Results were normalized to U6 non-coding small nuclear RNA (snRNA) and *Pde6b*^{ST/WT} values. Results demonstrate presence of Pde6b RNA in EVs from *Pde6b*^{ST/WT} and *Pde6b*^{ST/ST} *Pax6aCre* mice, but absence in *Pde6b*^{ST/ST} EVs. Circles, squares and triangles, individual mice. Data are presented as mean ± SEM. Tukey's test for multiple comparisons. *** $P < 0.001$. ns, not significant.

In the next step, isolated small EVs from each six pooled 10-weeks-old *Pde6b*^{ST/WT} *Pax6αCre*, *Pde6b*^{ST/ST} and *Pde6b*^{ST/ST} *Pax6αCre* retinas were treated with DNase I to destruct extravesicular DNA. After, samples were analyzed via PCR of *Pde6b*. As positive controls, two ear biopsy samples were used. One of these mice was genotyped as one *Pde6b*^{STr/WT}, showing a recombined and a wildtype band, and the other one as *Pde6b*^{ST/STr}, demonstrating a mutant and a recombined band (**Fig. 38**). Isolated small EVs of *Pde6b*^{ST/WT} *Pax6αCre* and *Pde6b*^{ST/ST} *Pax6αCre* retinas displayed faint *Pde6b* bands, while no *Pde6b* DNA was amplified in *Pde6b*^{ST/ST} EVs. The result from *Pde6b*^{ST/WT} *Pax6αCre* EVs showed the *Pde6b* wildtype band, while the mutant band was almost absent due to overall low material input. The mutant band in small EVs from *Pde6b*^{ST/ST} *Pax6αCre* retinas was also very weak but slightly more apparent. Comparable to FAC-sorted cells (**Fig. 25A**), small EVs from both *Pde6b*^{ST/WT} *Pax6αCre* and *Pde6b*^{ST/ST} *Pax6αCre* retinas contained recombined *Pde6b* DNA at 362 bp additionally (**Fig. 38**).

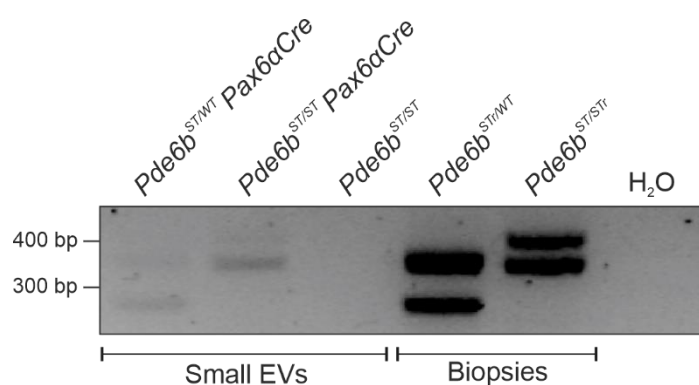


Figure 38: *Pde6b* DNA in isolated small EVs.

Pde6b^{ST/WT}, *Pde6b*^{ST/ST} and *Pde6b*^{ST/ST} *Pax6αCre* mice were analyzed at 10 weeks of age. Small extracellular vesicles (EVs) were isolated from six pooled retinas. For destruction of extravesicular DNA, EV pellets were treated with DNase I. DNA from samples was isolated and used for PCR of *Pde6b*. As positive controls, ear biopsy lysates from one *Pde6b*^{STr/WT} and one *Pde6b*^{ST/STr} mouse were used. Results display presence of *Pde6b* DNA, most interestingly recombined one, in EVs from *Pde6b*^{ST/WT} and *Pde6b*^{ST/ST} *Pax6αCre* mice. PCR products were separated by agarose gel electrophoresis. STr, STOP recombined.

4.3.3 Small EV-mediated transfer could not be confirmed

In order to confirm small EV-mediated transfer, vesicles from six pooled *Pde6b*^{ST/WT} retinas were isolated, labeled with PKH67 and added on 661W cells. Imaging of 661W cells in culture revealed endocytosed small EVs in their cytoplasm already 1 day after addition (**Fig. 39A**). Furthermore, staining was visible at all investigated timepoints indicating recycling of EV membranes rather than degradation. As 661W cells proliferated and divided, absorbed vesicles were passed on to daughter cells, since PKH67 staining was present in the cytoplasm of all cells at every investigated timepoint. On day 2, bigger cytoplasmic blabs were present, indicating MVBs in the EV pathway. On day 4 and 5, EV membranes were further recycled and visible as small dots all over the cytoplasm.

In the next step, 661W cells were harvested on day 5 and used for immunoblotting of PDE6B. As positive control, one retinal lysate of a *Pde6b*^{ST/WT} retina was used. Incubation with β -Actin-Peroxidase was performed as loading control showing an equal protein amount in all used samples (**Fig. 39B**). Incubation with PDE6B antibody revealed expression only in the *Pde6b*^{ST/WT} positive control, while protein was absent in 661W lysates regardless of incubation with small EVs.

As immunoblotting might not be sensitive enough to show low levels of PDE6B expression, *Pde6b* RNA was evaluated via quantitative real-time PCR, whereby one *Pde6b*^{ST/WT} retina was used as positive control. Again, *Pde6b* RNA was absent in both wildtype and 661W cells, that were previously incubated with small EVs for 5 days (**Fig. 39C**).

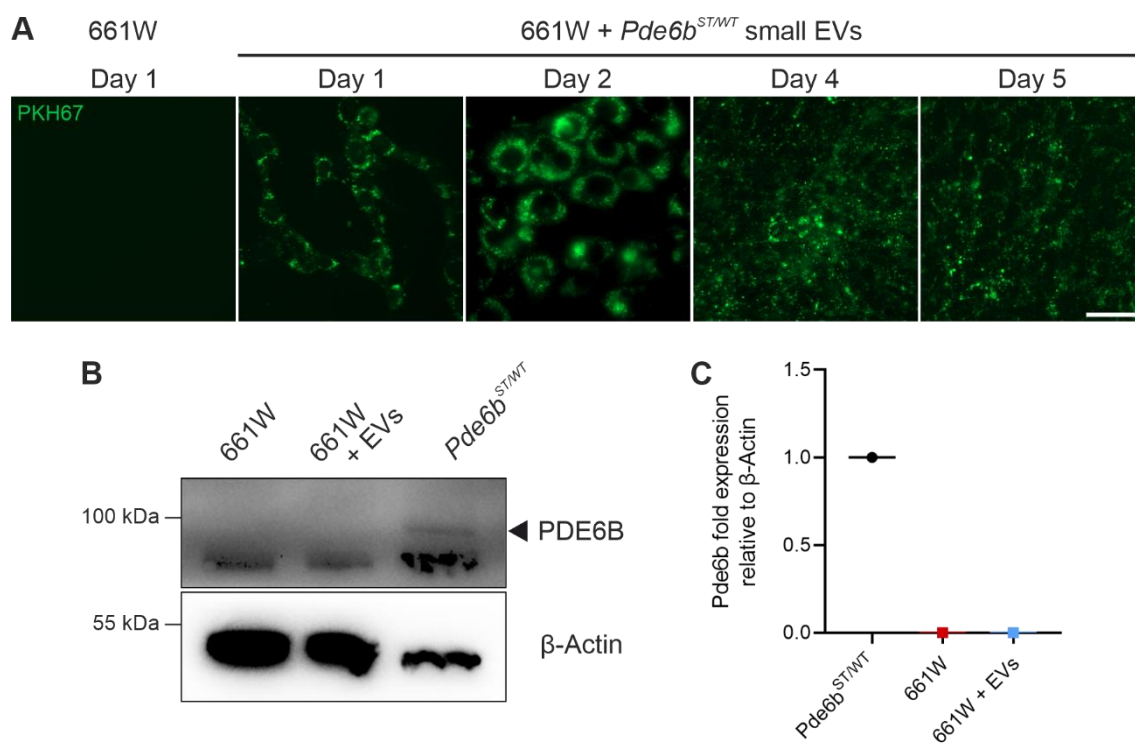


Figure 39: 661W cells show uptake of isolated small EVs but no PDE6B expression.

Small extracellular vesicles (EVs) from six pooled *Pde6b*^{ST/WT} retinas were isolated. **(A)** Membranes of isolated small EVs were labeled with PKH67 and added on 661W cells (Day 0). Shown are the representative cell culture images after addition of labeled small EVs or control cells. PKH67 labeling was found in the cytoplasm of 661W cells. Scale bar, 50 μ m. **(B,C)** Isolated small EVs were added on 661W cells for 5 days. Negative control cells were kept without addition of small EVs. As positive control, one 4-weeks-old *Pde6b*^{ST/WT} mouse was used. **(B)** Samples were lysed and used for immunoblotting with anti-PDE6B antibody, β -Actin-Peroxidase was used as loading control. **(C)** RNA from all samples was isolated and used for quantitative real-time PCR of *Pde6b*. Results were normalized to β -Actin and *Pde6b*^{ST/WT}. Results present absence of PDE6B and *Pde6b* RNA in 661W cells after incubation with small EVs. Circles and squares, individual mice. Data are presented as mean \pm SEM. Tukey's test for multiple comparisons.

As 661W cells do not grow any outer segments [141], transferred Pde6b RNA might be directly destroyed. Therefore, the experiment was repeated with retinal explants of 4-weeks-old *Pde6b^{ST/ST}* mice instead of 661W cells. To do so, isolated small EVs from six pooled *Pde6b^{ST/WT}* retinas were subretinally injected *ex vivo* into flatmounted right eyes. Left eye flatmounts of *Pde6b^{ST/ST}* mice were incubated without injection as negative controls. After 5 days, retinas were separated from the RPE-choroid-sclera tissue and lysed for quantitative real-time PCR. Thereby, one *Pde6b^{ST/WT}* retina from a 4-weeks-old mouse was used as positive control. As in the previous experiment, Pde6b RNA was absent in both the negative control as well as in small EV incubated retinal explants.

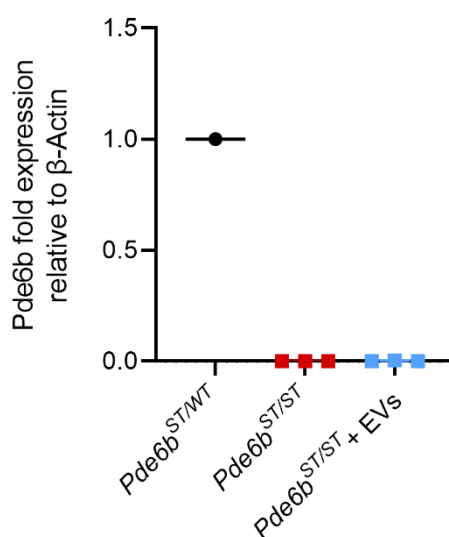


Figure 40: Absence of Pde6b RNA in retinal explants.

Pde6b^{ST/WT} and *Pde6b^{ST/ST}* mice were analyzed at 4 weeks of age. The retina from the *Pde6b^{ST/WT}* mouse was directly frozen. Eyes from *Pde6b^{ST/ST}* mice were used as retinal explants for 5 days. One eye per mouse was used as negative control, the other one was subretinally injected with small extracellular vesicles (EVs) from six pooled *Pde6b^{ST/WT}* retinas. RNA from all retinas was isolated and used for quantitative real-time PCR of Pde6b. Results were normalized to β-Actin and *Pde6b^{ST/WT}*. Results demonstrate Pde6b RNA in the *Pde6b^{ST/WT}* retina, but no expression in *Pde6b^{ST/ST}* retinas after incubation with small EVs. Circles and squares, individual mice. Data are presented as mean ± SEM. Tukey's test for multiple comparisons.

5 Discussion

In early stages of RP, patients experience night blindness but daylight vision is unimpaired and as a result these symptoms are often ignored or stay unnoticed [36,37]. Consequently, the disease is usually diagnosed in late stages when most of the photoreceptors are already impaired. As loss of photoreceptors cannot be reversed and the human retina lacks any regenerative capacity, one investigated therapeutic approach is the transplantation of stem cells or retinal precursors [96]. It has been reported that these cells rather provide trophic support to the damaged cells by cellular communication mechanisms instead of incorporation in the outer nuclear layer as replacement.

In this study, a RP mouse model, *Pde6b*^{STOP/STOP}, was used and partially rescued by Pax6 α Cre recombination. Using this system, the nasal and temporal periphery was sustainably rescued, while the central region around the optic nerve remained mutant. Using this approach, we were able to evaluate the effect of healthy rods on neighboring mutant rods.

5.1 Successful non-invasive rescue of RP mice

This study demonstrated a long-term functional rescue of the temporal and nasal periphery, which was comparable to wildtype mice. In particular, we found expression of PDE6B and its underlying RNA as well as fully recombined DNA in those regions (**Fig. 17,20,25**). These observations were in line with rescue of dendrites from second-order neurons (**Fig. 28**) as well as morphology of retinal vasculature (**Fig. 29,30,31**) and RPE cells (**Fig. 34**). In contrast, the outer nuclear layer thickness and cone length in the nasal and temporal periphery were slightly lower compared to wildtype results (**Fig. 19**). The reason for this might be cellular stress, as dying photoreceptors in the central area release various factors, such as reactive oxygen species (ROS) or proinflammatory cytokines, which are sensed by other retinal cells and might influence their survival or proper development. As the Cre-*LoxP* system cannot be performed in RP patients, viral vectors can be used for treatment, although their efficiency is often not as high as in our model [142]. Here we investigated a non-invasive rescue based on cell-cell communication, which is also applicable for the post-injection period of viral vectors or transplanted cells.

During disease progression after partial rescue, we observed stepwise expression of PDE6B, at a similar intensity as in control mice, and its underlying RNA in central mutant photoreceptors (**Fig. 17,20**). Thereby, the fluorescence *in situ* hybridization probe targeting Pde6b did show very specific labeling, as no staining was found in *Pde6b^{ST/ST}* negative control sections. By combination of the *Pde6b^{ST/ST} Pax6 α Cre* mouse model with either nuclear (*ROSA^{nT-nG}*) or membrane-bound (*ROSA^{mT-mG}*) endogenous two-color fluorescent reporter mice, we could rule out the possibility of peripheral cell movement to the center. In sections from 4-weeks-old rescued mice, both PDE6B and Pde6b RNA labels were mainly present in GFP-positive photoreceptors in the periphery, while tdTomato-positive photoreceptors in the center showed no expression. At 24 weeks of age, the immunolabeling already progressed to the central region bordering GFP-positive cells. Finally, in 48-weeks-old mice PDE6B and Pde6b RNA were expressed in all remaining photoreceptors in the outer nuclear layer regardless of GFP or tdTomato markers. Quantification of the distance from PDE6B-positive cells to the optic nerve confirmed that it became lower in sections from older mice compared to young ones (**Fig. 18**). Membrane and nuclear fusion events were excluded as underlying mechanism as both endogenous markers did not overlay in the same cell. Furthermore, *Pde6b^{ST/ST}* showed absence of spontaneous recombination events due to no occurrence of PDE6B or Pde6b RNA at any investigated timepoint (**Fig. 15,17,20**).

As consequence of slow stepwise PDE6B expression and subsequent rescue of rods, also secondary cone cell death was halted (**Fig. 19**). On the other hand, non-rescued central photoreceptors, which are far away from GFP-positive cells, underwent progressive degeneration comparable to *Pde6b^{ST/ST}* mice. Thus, we observed the evolvement of a gradient in the outer nuclear layer thickness, that decreased in a peripheral to center manner (**Fig. 19**). A similar result was found in the cone length, as cones undergo remodeling displayed by shortening [143]. In accordance, rod bipolar cells, cone bipolar cells and horizontal cells were reported to have a normal morphology if enough connected photoreceptors were rescued (**Fig. 28**). If rods were rescued at late stages of disease progression, they underwent retinal remodeling by progressive retraction or complete loss of dendrites. Therefore, we conclude that late rescue of photoreceptors, when approximately less than two layers of nuclei in the outer nuclear layer are left, does not halt retinal remodeling, which is in accordance with previous studies in our lab where a tamoxifen-induced Cre recombinase was used for late stage treatment [122]. These late rescued photoreceptors close to the optic nerve are thus assumed to be not functional. In this context, it is also possible that retinas are even more rescued but affected photoreceptors still undergo cell death after the threshold timepoint was reached.

After successful rescue, it was shown that visual function was restored as well. In particular, scotopic and mesopic as well as photopic ERG responses were strongly evoked but still slightly reduced compared to control mice (**Fig. 26,27**), which demonstrates that not all photoreceptors were rescued or some rescued photoreceptors might be dysfunctional. For this mouse model, it would be beneficial to measure electrophysiological responses with a multielectrode array (MEA). In contrast to the ERG, which records the overall retinal activity, the MEA measures responses in several smaller locations, which allows the distinction between peripheral and central regions [144]. This would generate a more precise insight about the function of rescued cells, although this procedure requires the isolated retina *ex vivo*, which might not reflect the same physiology as *in vivo*.

It was demonstrated that photoreceptor rescue was more prominent on the temporal side of the sections compared to the nasal side (**Fig. 18**). Although this effect was already observed in 4-weeks-old mice, the difference to 48-weeks-old mice was more significant on the temporal side as well. It has been reported that *Pax6α* is expressed in a spatial manner with high occurrence in the nasal and temporal periphery [117,118]. Anyhow, it is not described why there might be a slightly stronger expression on the temporal side. It can be hypothesized that rescue on the temporal side is progressing faster as there are less degenerating photoreceptors and thus decreased cellular stress. Nevertheless, results displayed a high variance between individual mice, therefore the observed low effect might also be artificial.

5.2 Possibility of low-level postnatal Cre expression

As postnatal *Pax6α*Cre recombinase expression might be the reason for PDE6B expression, Cre levels were evaluated using immunoblotting, quantitative real-time PCR and fluorescence *in situ* hybridization. Cre protein in retinal lysates and Cre RNA in tdTomato/PDE6B double-positive FAC-sorted cells were completely absent (**Fig. 22,24**). Using fluorescence *in situ* hybridization in retinal sections, which enables the detection of one RNA molecule [145], Cre RNA was only detected in nuclei at the inner margin of the inner nuclear layer (**Fig. 23**). These cells are most likely amacrine cells as they express *Pax6* postnatally [146]. In line with the used Cre-reporter, these Cre-positive cells did also express EGFP.

These data indicate that there is no postnatal expression of Cre recombinase in tdTomato-positive photoreceptor cells. Nonetheless, the possibility of low-level postnatal Cre expression in photoreceptors persists. For example, there may be unexpected transient expression of Pax6 α Cre recombinase in photoreceptors, which is not detected in our snapshot of the investigated retinal section. The fact that our double-color Cre reporter indicates no Cre expression (i.e. in tdTomato-positive cells) could be explained by an easier access or a higher sensitivity of the *Pde6b* locus over the *ROSA26* locus for Cre recombination [147], i.e. Cre would only recombine *LoxP* sites of *Pde6b* but not *LoxP* sites of tdTomato. Still, two arguments against this hypothesis remain. First, PDE6B was described to progress closer to the optic nerve over time and secondly, this evolution results in a peripheral to center gradient in the outer nuclear layer thickness due to cell death of non-rescued cells. In case of spontaneous postnatal Cre expression in photoreceptors, this effect is expected to occur randomly in cells of the central tdTomato-positive region independently of their distance to EGFP-expressing photoreceptors and thus without development of a gradient in the outer nuclear layer thickness.

5.3 Potential ongoing central vasculature remodeling after partial rescue

Retinal vasoconstriction and dysfunction have been described as a characteristic clinical finding in RP patients [47,51] and mouse models [122,148,149]. It has already been reported that the underlying mechanism of disease-induced blood vessel altering are elevated oxygen levels due to missing consumption by photoreceptors [150,151]. As a consequence, the affected vessels may sustain to cone photoreceptor degeneration due to inadequate retinal supplementation with oxygen or nutrients.

In partially rescued mice, we observed that the central superficial vascular plexus did not display attenuation but modest morphological abnormalities (**Fig. 30**). As the superficial vascular plexus is located furthest from primarily affected photoreceptors, it is not surprising that it depicts either just weak or late onset morphological changes. In addition, it is crucial for retinal function to maintain these vessels in the center since all underlying plexi derive from the single superficial central retinal artery. Various studies have shown that ganglion cells undergo remodeling and loss after complete degeneration of the outer nuclear layer [152]. Thus, it can be suggested that, concurrent to this inner retinal remodeling, the superficial vascular plexus might continue to alter and then also undergoes vasoconstriction at later timepoints.

In partially rescued mice, the vessel area in the central deep and intermediate vascular plexi slightly decreased over time, while vessels in the periphery were unaffected (**Fig. 29,31**). As RP is associated with microglial activation, which promote retinal inflammation [153,154], it is possible that a subsequent enhanced release of VEGF, primarily from Müller cells [155] and the RPE [27], but also from ganglion cells [156], astrocytes [157] and microglia themselves [158], supports survival of vessels in the center despite photoreceptor degeneration. In addition, surviving endothelial cells in the periphery may contribute to maintain central ones via communication through gap junctions [159], secretion of growth factors or adhesion to the extracellular matrix [160], which activates anti-apoptotic pathways. Similar to the superficial vascular plexus, it can be hypothesized that also the central deep and intermediate vascular plexus may continue to remodel if rescued photoreceptors are not preserved long-term.

Nevertheless, to what extent the central abnormal blood vessels are still functional enough, e.g. in their blood flow capacity, to support the retina long term is still questionable and needs to be investigated in future research, possibly via fluorescein angiography [161].

5.4 Crucial role of the RPE in retinal rescue

Alterations in RPE cells during RP disease progression have been reported in various studies [42-46]. The underlying reason for these changes has been described as accumulation of oxidative stress and inflammation leading to mitochondrial dysfunction and thus metabolic imbalance [162]. Here, we also demonstrated morphological changes in the RPE of *Pde6b^{ST/ST}* mice, that evolved as consequence to photoreceptor degeneration as it has already been shown in other studies [122,149,163]. In particular, we found that cells lost their characteristic hexagonal shape associated with size shrinkage in the center but enlargement in the periphery in far advanced disease stages (**Fig. 32**).

The onset of RPE remodeling was prominent in the central retina at 24 weeks of age, while no changes in the periphery were observed at this timepoint (**Fig. 34**). This observation is in line with the progression of photoreceptor loss in RP mouse models, as it first occurs in the center of the retina and spreads to the periphery [164]. We could further prove that small abnormal cells in the center do not arise from re-onset of mitosis but that they show disruptions in their tubulin cytoskeleton structure (**Fig. 33**). It can be assumed that these changes emerge from a dedifferentiation of RPE cells and following epithelial-mesenchymal transition (EMT), which has been implicated with stress response in several retinal diseases [165–167]. This hypothesis is consistent with the described release of β -Catenin to the cytoplasm both in center and periphery

(**Fig. 34**), that is also accompanied with loss of cell adhesion and cytoskeleton disruption [168,169].

On the other hand, RPE cell expansion in the periphery, which is usually associated with multinucleation, might play a role in homeostasis maintenance as it has been reported during aging [170]. In accordance, size reduction of RPE cells, that is further enhanced by disease-triggered lipofuscin accumulation, has been rather associated with loss of function and subsequent cell death [171,172]. This is consistent with our finding of a circular area of absent RPE cells around the optic nerve in *Pde6b^{ST/ST}* mice, assuming that small abnormal RPE cells next undergo cell death (**Fig. 32**).

After partial rescue, we demonstrated the prevention of RPE morphology changes not only in the periphery but also in the center despite ongoing photoreceptor degeneration (**Fig. 34**). It can be suggested that surrounding peripheral healthy RPE cells are capable to support central ones with nutrients and growth factors as it has been described after transplantation of RPE cells [173]. In addition, RPE cells were shown to induce various stress response pathways, such as the unfolded protein response in the endoplasmatic reticulum [174] or lysosomal autophagy processes [175], in order to promote their survival. Thus, the RPE might be a highly stress resistant tissue with higher tolerance or self-preservation than the vasculature. This hypothesis is in line with the fact that almost no morphological changes were observed in our *Pde6b^{ST/ST}* mice at 24 weeks of age despite far advanced disease stage (**Fig. 34**). It might be possible that RPE cells continue to remodel if rescued photoreceptors are not preserved long-term. Furthermore, is still questionable to what extent those abnormal RPE cells are still functional. This needs to be investigated in future research, e.g. by investigating the phagocytic capacity with a phagocytosis assay [176].

5.5 Small EVs as most likely mediator of horizontal material transport

As the underlying mechanism of horizontal material transfer, two possibilities come into question. The first one are cellular connections like nanotubes, which were reported to be rather exceptional and thus graded as less likely to be responsible since we showed the appearance of high PDE6B protein and *Pde6b* RNA amounts (**Fig. 17,20**). Instead, retinal small EVs were investigated as they are more frequent and have the ability to transport cargo over longer distances [139].

For isolation, differential ultracentrifugation was used to separate small EVs based on their size [177]. Using this method, it is presumed that free floating material, that is not surrounded by a lipid bilayer, is destroyed during the lengthy process. We showed the successful isolation of small

particles, mostly in the size range of exosomes but also partly microvesicles, with equal concentration among different samples (**Fig. 35**). Moreover, isolated small EVs were viable as they were endocytosed by 661W cells in culture (**Fig. 39A**). Although we only separated the smallest particles in our samples, we cannot fully exclude the possibility of low-level contamination e.g. with bigger vesicles or free floating material. To improve the isolation, an additional pulldown with exosome-specific antibodies, e.g. against CD9, CD63 or CD81, is imaginable [177]. Though, the outcome would be even lower concentrations due to insufficient binding to some targets, which is not feasible for our purposes.

Next, we reported accumulation of gold particle labeled PDE6B in vesicle-like structures in inner and outer segment regions in different exo- or endocytosis stages either close to the membrane or in the extracellular space between photoreceptors (**Fig. 36**). Overall PDE6B labeling in outer segment discs was very low, which can be explained by the fact that this method only detects surface antigens. On the other hand, inner segments did not display any PDE6B particles confirming the labeling specificity. It cannot be fully excluded that the shown structures are something else than small EVs since they were only identified by their morphological features. To rule out this possibility, co-labeling with an EV-specific antibody needs to be performed.

Furthermore, we found Pde6b RNA in isolated small EVs from both control and rescued mice, although expression levels were slightly lower in second named ones (**Fig. 37**). It can be suggested that Pde6b RNA is the underlying transferred material for PDE6B expression in rescued cells as this result is in line with previous findings (**Fig. 20,21**) but still in conflict with the presence of recombinant *Pde6b* DNA in FAC-sorted cells (**Fig. 25**). Small EVs carry numerous different nucleic acids, including double-stranded DNA [79,85], which has gained a lot of attention in cancer and cardiovascular disease therapies as they can transfer their cargo to surrounding cells [72,80]. Indeed, we also found Pde6b DNA in isolated small EVs from control and rescued mice (**Fig. 38**). Especially the incidence of recombinant DNA is of special interest and might explain previous findings in FAC-sorted cells (**Fig. 25**). Conversely, only approximately 200 bp DNA fragments were reported in small EVs, while large EVs are capable of carrying DNA with more than 2 million bp length [178]. As the whole *Pde6b* gene has a size of more than 43,000 bp, it is very unlikely that it is completely packed in small EVs. Anyhow, our PCR products have a size of 284 bp for wildtype and 415 bp for mutant, which is already bigger than the mentioned capacity. It might also be feasible that only small *Pde6b* DNA fragments are transported, migrate to the nuclear envelope upon uptake and integrate into the genomes of recipient cells, as it has already been described for other cell types [72,179]. In our mouse model, *Pde6b* was found in small EVs from healthy control mice as well (**Fig. 38**), which suggests that the selection of transported DNA is rather random than

specific to requirements of recipient cells. This is also in line with previous reported transport of fluorophores, that have no function in recipient cells [64–67]. The theory of horizontal DNA transfer in our retinas further arises the question about the origin of exosomal DNA. One proposed mechanism is the derivation from micronuclei, which describe nuclear membrane enclosed structures, that contain DNA fragments from mis- or unrepaired DNA breaks [180]. Micronuclei are reported to be quite instable and were shown to occasionally collapse. After release of their contents, DNA fragments may be shuttled to multivesicular bodies and ultimately packed into extracellular vesicles.

To proof our hypothesis about small EV-mediated material transfer, we first performed the addition of isolated PKH67-labeled small EVs on 661W cells. We could show a successful uptake and maintenance of labeled small EV membranes over time (**Fig. 39**). However, no PDE6B or Pde6b RNA could be detected after incubation for 5 days. The reason for this might be that 661W do not grow any outer segments in culture and thus do not express the other required PDE6 subunits, which has been reported to be essential for survival [181]. Thus, possibly transferred material is not needed and might be directly degraded. To circumvent this problem, the experiment was repeated in *Pde6b^{ST/ST}* retinal explant cultures via subretinal injection. Unfortunately, again no expression of Pde6b RNA could be measured after incubation for 5 days (**Fig. 40**). It can be also hypothesized that 5 days are not long enough to detect low levels of transferred material via immunoblotting or quantitative real-time PCR. Instead, cultured retinas could be prepared as frozen sections and PDE6B or Pde6b RNA immunofluorescently labeled. However, this method also turns out to be difficult due to loss of retinal structure *in vitro*, especially in the region of sensitive photoreceptor outer segments, which becomes more evident with longer incubation [182]. Another feasible approach for the proof of concept could be the subretinal injection *in vivo* with longer incubation.

To sum up, we report a communication mechanism between healthy and mutant rods, possibly via small EVs, leading to retinal rescue. Small EVs were already described as attractive therapeutic vectors due to their reduced immunogenicity, protection from degradation and ability to cross the blood-retinal barrier [95], while the immune-privileged retina represents an ideal target for them [80]. Thus, the treatment of RP patients using EV vectors might open new possibilities in the field of gene-independent therapy.

6 References

1. Warwick R, Williams PL. Gray's anatomy. 35th British ed. Philadelphia: WB Saunder's Company. 1973; 1100–1122.
2. Davson H. The eye. Academic Press; 1984.
3. Oyster CW. The human eye. Sunderland, MA: Sinauer. 1999; 411–445, 708–732.
4. Straatsma BR, Landers MB, Kreiger AE. The Ora Serrata in the Adult Human Eye. Archives of Ophthalmology. 1968;80: 3–20. doi:10.1001/ARCHOPHT.1968.00980050005002
5. Veleri S, Lazar CH, Chang B, Sieving PA, Banin E, Swaroop A. Biology and therapy of inherited retinal degenerative disease: insights from mouse models. Dis Model Mech. 2015;8: 109–129. doi:10.1242/DMM.017913
6. Wilkinson CP, Hinton DR, Sadda SR, Wiedemann P. Ryan's Retina E-Book. Elsevier Health Sciences; 2017.
7. Wensel TG. Molecular Biology of Vision. Basic Neurochemistry: Principles of Molecular, Cellular, and Medical Neurobiology: Eighth Edition. 2011; 889–903. doi:10.1016/B978-0-12-374947-5.00051-1
8. Eggers ED, Lukasiewicz PD. GABAA, GABAC and glycine receptor-mediated inhibition differentially affects light-evoked signalling from mouse retinal rod bipolar cells. Journal of Physiology. 2006;572: 215–225. doi:10.1113/JPHYSIOL.2005.103648
9. Soucy E, Wang Y, Nirenberg S, Nathans J, Meister M. A novel signaling pathway from rod photoreceptors to ganglion cells in mammalian retina. Neuron. 1998;21: 481–493. doi:10.1016/S0896-6273(00)80560-7
10. Bringmann A, Pannicke T, Grosche J, Francke M, Wiedemann P, Skatchkov SN, et al. Müller cells in the healthy and diseased retina. Prog Retin Eye Res. 2006;25: 397–424. doi:10.1016/J.PRETEYERES.2006.05.003
11. Karlstetter M, Scholz R, Rutar M, Wong WT, Provis JM, Langmann T. Retinal microglia: Just bystander or target for therapy? Prog Retin Eye Res. 2015;45: 30–57. doi:10.1016/J.PRETEYERES.2014.11.004
12. Yao H, Wang T, Deng J, Liu D, Li X, Deng J. The development of blood-retinal barrier during the interaction of astrocytes with vascular wall cells. Neural Regen Res. 2014;9: 1047. doi:10.4103/1673-5374.133169
13. Molday RS, Moritz OL. Photoreceptors at a glance. J Cell Sci. 2015. doi:10.1242/jcs.175687

14. Arikawa K, Molday LL, Molday RS, Williams DS. Localization of peripherin/rds in the disk membranes of cone and rod photoreceptors: Relationship to disk membrane morphogenesis and retinal degeneration. *Journal of Cell Biology*. 1992;116: 659–667. doi:10.1083/jcb.116.3.659
15. Peichl L. Diversity of Mammalian Photoreceptor Properties: Adaptations to Habitat and Lifestyle? *Anat Rec*. 2005. doi:10.1002/ar.a.20262
16. Deeb SS. Genetics of variation in human color vision and the retinal cone mosaic. *Curr Opin Genet Dev*. 2006;16: 301–307. doi:10.1016/J.GDE.2006.04.002
17. Szél A, Röhlich P, Mieziowska K, Aguirre G, van Veen T. Spatial and temporal differences between the expression of short- and middle-wave sensitive cone pigments in the mouse retina: A developmental study. *Journal of Comparative Neurology*. 1993;331: 564–577. doi:10.1002/CNE.903310411
18. Chen CK. The vertebrate phototransduction cascade: Amplification and termination mechanisms. *Rev Physiol Biochem Pharmacol*. 2005;154: 101–121. doi:10.1007/S10254-005-0004-5/COVER
19. Burns ME, Arshavsky VY. Beyond Counting Photons: Trials and Trends in Vertebrate Visual Transduction. *Neuron*. 2005;48: 387–401. doi:10.1016/J.NEURON.2005.10.014
20. Grassmeyer JJ, Cahill AL, Hays CL, Barta C, Quadros RM, Gurusurthy CB, et al. Ca²⁺ sensor synaptotagmin-1 mediates exocytosis in mammalian photoreceptors. *Elife*. 2019. doi:10.7554/eLife.45946.001
21. Martemyanov KA, Sampath AP. The Transduction Cascade in Retinal ON-Bipolar Cells: Signal Processing and Disease. *Annu Rev Vis Sci*. 2017;3: 25–51. doi:10.1146/ANNUREV-VISION-102016-061338
22. Demb JB, Singer JH. Functional Circuitry of the Retina. *Annu Rev Vis Sci*. 2015;1: 263–289. doi:10.1146/ANNUREV-VISION-082114-035334
23. Cote RH. Characteristics of Photoreceptor PDE (PDE6): similarities and differences to PDE5. *International Journal of Impotence Research* 2004 16:1. 2004;16: S28–S33. doi:10.1038/sj.ijir.3901212
24. Hargrave PA, McDowell JH. Rhodopsin and phototransduction: a model system for G protein-linked receptors. *The FASEB Journal*. 1992;6: 2323–2331. doi:10.1096/FASEBJ.6.6.1544542
25. Bill A, Sperber G, Ujiie K. Physiology of the choroidal vascular bed. *Int Ophthalmol*. 1983. doi:10.1007/BF00127638

-
26. Kur J, Newman EA, Chan-Ling T. Cellular and physiological mechanisms underlying blood flow regulation in the retina and choroid in health and disease. *Prog Retin Eye Res.* 2012;31: 377–406. doi:10.1016/J.PRETEYERES.2012.04.004
 27. Strauss O. The retinal pigment epithelium in visual function. *Physiol Rev.* 2005;85: 845–881. doi:10.1152/physrev.00021.2004
 28. Stahl A, Connor KM, Sapieha P, Chen J, Dennison RJ, Krah NM, et al. The Mouse Retina as an Angiogenesis Model. *Invest Ophthalmol Vis Sci.* 2010;51: 2813–2826. doi:10.1167/IOVS.10-5176
 29. Paques M, Tadayoni R, Sercombe R, Laurent P, Genevois O, Gaudric A, et al. Structural and Hemodynamic Analysis of the Mouse Retinal Microcirculation. *Invest Ophthalmol Vis Sci.* 2003;44: 4960–4967. doi:10.1167/IOVS.02-0738
 30. Bok D. The retinal pigment epithelium: a versatile partner in vision. *J Cell Sci.* 1993;17: 189–195. doi:10.1242/jcs.1993.supplement_17.27
 31. Baehr W, Wu SM, Bird AC, Palczewski K. The retinoid cycle and retina disease. *Vision Res.* 2003;43: 2957–2958. doi:10.1016/J.VISRES.2003.10.001
 32. Dornonville de la Cour M. Ion transport in the retinal pigment epithelium. A study with double barrelled ion-selective microelectrodes. *Acta Ophthalmol Suppl (Oxf).* 1993; 1–32.
 33. Hamann S. Molecular mechanisms of water transport in the eye. *Int Rev Cytol.* 2002;215: 395–431. doi:10.1016/s0074-7696(02)15016-9
 34. Finnemann SC. Focal adhesion kinase signaling promotes phagocytosis of integrin-bound photoreceptors. *EMBO J.* 2003;22: 4143–4154. doi:10.1093/EMBOJ/CDG416
 35. Menghini M, Cehajic-Kapetanovic J, MacLaren RE. Monitoring progression of retinitis pigmentosa: current recommendations and recent advances. *Expert Opin Orphan Drugs.* 2020;8: 67. doi:10.1080/21678707.2020.1735352
 36. Hamel C. Retinitis pigmentosa. *Orphanet J Rare Dis.* 2006;1: 1–12. doi:10.1186/1750-1172-1-40
 37. Hartong DT, Berson EL, Dryja TP. Retinitis pigmentosa. *Lancet.* 2006;368: 1795–1809. doi:10.1016/S0140-6736(06)69740-7
 38. Tsang SH, Sharma T. Retinitis Pigmentosa (Non-syndromic). *Adv Exp Med Biol.* 2018;1085: 125–130. doi:10.1007/978-3-319-95046-4_25
 39. Bunker CH, Berson EL, Bromley WC, Hayes RP, Roderick TH. Prevalence of Retinitis Pigmentosa in Maine. *Am J Ophthalmol.* 1984;97: 357–365. doi:10.1016/0002-9394(84)90636-6

40. Novak-Lauš K, Kukulj S, Zorić-Geber M, Bastaić O. Primary tapetoretinal dystrophies as the cause of blindness and impaired vision in the republic of Croatia. *Acta Clin Croat.* 2002;41: 23–25.
41. Dvir L, Srour G, Abu-Ras R, Miller B, Shalev SA, Ben-Yosef T. Autosomal-Recessive Early-Onset Retinitis Pigmentosa Caused by a Mutation in PDE6G, the Gene Encoding the Gamma Subunit of Rod cGMP Phosphodiesterase. *The American Journal of Human Genetics.* 2010;87: 258–264. doi:10.1016/j.ajhg.2010.06.016
42. Marc RE, Jones BW, Watt CB, Strettoi E. Neural remodeling in retinal degeneration. *Prog Retin Eye Res.* 2003;22: 607–655. doi:10.1016/S1350-9462(03)00039-9
43. Jones BW, Marc RE. Retinal remodeling during retinal degeneration. *Exp Eye Res.* 2005;81: 123–137.
44. Marc RE, Jones BW. Retinal Remodeling in Inherited Photoreceptor Degenerations. *Mol Neurobiol.* 2003;28: 139–147. doi:10.1385/MN:28:2:139/METRICS
45. Jones BW, Watt CB, Frederick JM, Baehr W, Chen CK, Levine EM, et al. Retinal remodeling triggered by photoreceptor degenerations. *Journal of Comparative Neurology.* 2003;464: 1–16. doi:10.1002/CNE.10703
46. Li ZY, Possin DE, Milam AH. Histopathology of bone spicule pigmentation in retinitis pigmentosa. *Ophthalmology.* 1995;102: 805–816. doi:10.1016/S0161-6420(95)30953-0
47. Corazza P, Cirafici P, Testa V, Orleans HO, Berisso M, Traverso CE, et al. Vascular Density and Retinal Function in Patients with Retinitis Pigmentosa Evaluated by Swept-Source OCT Angiography and Microperimetry. *Ophthalmologica.* 2021;244: 27–33. doi:10.1159/000507961
48. Ayton LN, Guymer RH, Luu CD. Choroidal thickness profiles in retinitis pigmentosa. *Clin Exp Ophthalmol.* 2013;41: 396–403. doi:10.1111/J.1442-9071.2012.02867.X
49. Zhang Y, Harrison JM, San O, Nateras E, Chalfin S, Duong TQ. Decreased retinal-choroidal blood flow in retinitis pigmentosa as measured by MRI. *Documenta Ophthalmologica.* 2013. doi:10.1007/s10633-013-9374-1
50. Beutelspacher SC, Serbecic N, Barash H, Burgansky-Eliash Z, Grinvald A, Krastel H, et al. Retinal blood flow velocity measured by retinal function imaging in retinitis pigmentosa. *Graefe's Archive for Clinical and Experimental Ophthalmology.* 2011. doi:10.1007/s00417-011-1757-y
51. Jauregui R, Park KS, Duong JK, Mahajan VB, Tsang SH. Quantitative progression of retinitis pigmentosa by optical coherence tomography angiography. *Sci Rep.* 2018. doi:10.1038/s41598-018-31488-1

-
52. Türksever C, Valmaggia C, Orgül S, Schorderet DF, Flammer J, Todorova MG. Retinal vessel oxygen saturation and its correlation with structural changes in retinitis pigmentosa. *Acta Ophthalmol.* 2014;92: 454–460. doi:10.1111/AOS.12379
 53. Grunwald JE, Maguire AM, Dupont J. Retinal hemodynamics in retinitis pigmentosa. *Am J Ophthalmol.* 1996;122: 502–508. doi:10.1016/S0002-9394(14)72109-9
 54. Dorn JD, Ahuja AK, Caspi A, Da Cruz L, Dagnelie G, Sahel J-A, et al. The Detection of Motion by Blind Subjects With the Epiretinal 60-Electrode (Argus II) Retinal Prosthesis. *JAMA Ophthalmol.* 2013;131: 183–189. doi:10.1001/2013.jamaophthalmol.221
 55. Stingl K, Bartz-Schmidt KU, Besch D, Chee CK, Cottrill CL, Gekeler F, et al. Subretinal Visual Implant Alpha IMS - Clinical trial interim report. *Vision Res.* 2015;111: 149–160. doi:10.1016/J.VISRES.2015.03.001
 56. Kingma H, Borton D, Yagi T, Stingl K, Schippert R, Bartz-Schmidt KU, et al. Interim Results of a Multicenter Trial with the New Electronic Subretinal Implant Alpha AMS in 15 Patients Blind from Inherited Retinal Degenerations. *Front Neurosci.* 2017;1: 445. doi:10.3389/fnins.2017.00445
 57. Ong T, Pennesi ME, Birch DG, Lam BL, Tsang SH. Adeno-Associated Viral Gene Therapy for Inherited Retinal Disease. *Pharm Res.* 2019. doi:10.1007/s11095-018-2564-5
 58. Riedmayr LM, Hinrichsmeyer KS, Thalhammer SB, Karguth N, Böhm S, Mittas DM, et al. mRNA trans-splicing dual AAV vectors for (epi)genome editing and gene therapy. *bioRxiv.* 2023 [cited 9 Mar 2023]. doi:10.1101/2023.02.07.527504
 59. Tezel TH, Ruff A. Retinal cell transplantation in retinitis pigmentosa. *Taiwan J Ophthalmol.* 2021;11: 336. doi:10.4103/TJO.TJO_48_21
 60. Irigoyen C, Amenabar Alonso A, Sanchez-Molina J, Rodríguez-Hidalgo M, Lara-López A, Ruiz-Ederra J. Subretinal Injection Techniques for Retinal Disease: A Review. *J Clin Med.* 2022;11: 4717. doi:10.3390/JCM11164717/S1
 61. Gasparini SJ, Tessmer K, Reh M, Wieneke S, Carido M, Völkner M, et al. Transplanted human cones incorporate into the retina and function in a murine cone degeneration model. *J Clin Invest.* 2022. doi:10.1172/JCI154619
 62. Kalargyrou AA, Basche M, Hare A, West EL, Smith AJ, Ali RR, et al. Nanotube-like processes facilitate material transfer between photoreceptors. *EMBO Rep.* 2021;22. doi:10.15252/EMBR.202153732
 63. Ortin-Martinez A, Yan NE, Leh E, Tsai S, Comanita L, Gurdita A, et al. Photoreceptor nanotubes mediate the in vivo exchange of intracellular material. *EMBO J.* 2021;40: e107264. doi:10.15252/EMBJ.2020107264

-
64. Santos-Ferreira T, Llonch S, Borsch O, Postel K, Haas J, Ader M. Retinal transplantation of photoreceptors results in donor-host cytoplasmic exchange. *Nat Commun.* 2016;7. doi:10.1038/NCOMMS13028
 65. Singh MS, Balmer J, Barnard AR, Aslam SA, Moralli D, Green CM, et al. Transplanted photoreceptor precursors transfer proteins to host photoreceptors by a mechanism of cytoplasmic fusion. *Nat Commun.* 2016;7: 1–5. doi:10.1038/ncomms13537
 66. Ortin-Martinez A, Tsai ELS, Nickerson PE, Bergeret M, Lu Y, Smiley S, et al. A Reinterpretation of Cell Transplantation: GFP Transfer From Donor to Host Photoreceptors. *Stem Cells.* 2017;35: 932–939. doi:10.1002/stem.2552
 67. Pearson RA, Gonzalez-Cordero A, West EL, Ribeiro JR, Aghaizu N, Goh D, et al. Donor and host photoreceptors engage in material transfer following transplantation of post-mitotic photoreceptor precursors. *Nat Commun.* 2016;7: 1–15. doi:10.1038/ncomms13029
 68. Decembrini S, Martin C, Sennlaub F, Chemtob S, Biel M, Samardzija M, et al. Cone Genesis Tracing by the Chrn4-EGFP Mouse Line: Evidences of Cellular Material Fusion after Cone Precursor Transplantation. *Molecular Therapy.* 2017;25: 634–653. doi:10.1016/J.YMTHE.2016.12.015
 69. MacLaren RE, Pearson RA, MacNeil A, Douglas RH, Salt TE, Akimoto M, et al. Retinal repair by transplantation of photoreceptor precursors. *Nature.* 2006;444: 203–207. doi:10.1038/nature05161
 70. Heisterkamp P, Borsch O, Lezama ND, Gasparini S, Fathima A, Carvalho LS, et al. Evidence for endogenous exchange of cytoplasmic material between a subset of cone and rod photoreceptors within the adult mammalian retina via direct cell-cell connections. *Exp Eye Res.* 2022;219: 109033. doi:10.1016/J.EXER.2022.109033
 71. Colombo M, Raposo G, Théry C. Biogenesis, secretion, and intercellular interactions of exosomes and other extracellular vesicles. *Annu Rev Cell Dev Biol.* 2014;30: 255–289. doi:10.1146/annurev-cellbio-101512-122326
 72. Bor Valcz G, tá BU, ri jvá, Buzá EI, Krená cs T, ndor Spisá S, et al. Small extracellular vesicle DNA-mediated horizontal gene transfer as a driving force for tumor evolution: Facts and riddles. *Front Oncol.* 2022. doi:10.3389/fonc.2022.945376
 73. Shah N, Ishii M, Brandon C, Ablonczy Z, Cai J, Liu Y, et al. Extracellular vesicle-mediated long-range communication in stressed retinal pigment epithelial cell monolayers. *Biochim Biophys Acta Mol Basis Dis.* 2018;1864: 2610–2622. doi:10.1016/J.BBADIS.2018.04.016

-
74. Mighty J, Zhou J, Benito-Martin A, Sauma S, Hanna S, Onwumere O, et al. Analysis of Adult Neural Retina Extracellular Vesicle Release, RNA Transport and Proteomic Cargo. *Invest Ophthalmol Vis Sci.* 2020;61. doi:10.1167/IOVS.61.2.30
 75. Knickelbein JE, Liu B, Arakelyan A, Zicari S, Hannes S, Chen P, et al. Modulation of Immune Responses by Extracellular Vesicles From Retinal Pigment Epithelium. *Immunology and Microbiology.* 2016;57: 4101–4107. doi:10.1167/iovs.15-18353
 76. Kalargyrou AA, Guilfoyle SE, Smith AJ, Ali RR, Pearson RA. Extracellular vesicles in the retina - putative roles in physiology and disease. *Front Mol Neurosci.* 2023. doi:10.3389/fnmol.2022.1042469
 77. Flores-Bellver M, Mighty J, Aparicio-Domingo S, Li K V., Shi C, Zhou J, et al. Extracellular vesicles released by human retinal pigment epithelium mediate increased polarised secretion of drusen proteins in response to AMD stressors. *J Extracell Vesicles.* 2021;10. doi:10.1002/JEV2.12165
 78. Battistelli M, Falcieri E. Apoptotic Bodies: Particular Extracellular Vesicles Involved in Intercellular Communication. *Biology (Basel).* 2020. doi:10.3390/biology9010021
 79. Gurung S, Perocheau D, Touramanidou L, Baruteau J. The exosome journey: from biogenesis to uptake and intracellular signalling. *Cell Communication and Signaling* 2021 19:1. 2021;19: 1–19. doi:10.1186/S12964-021-00730-1
 80. Dupont S, Sundstrom J, Beatriz Calcaterra N, Xie P, Hu Z, Zhang Z, et al. Emerging Role of Exosomes in Retinal Diseases. *Front Cell Dev Biol.* 2021;9: 643680. doi:10.3389/fcell.2021.643680
 81. Rana S, Yue S, Stadel D, Zöller M. Toward tailored exosomes: The exosomal tetraspanin web contributes to target cell selection. *International Journal of Biochemistry and Cell Biology.* 2012;44: 1574–1584. doi:10.1016/j.biocel.2012.06.018
 82. Larios J, Mercier V, Roux A, Gruenberg J. ALIX- And ESCRT-III-dependent sorting of tetraspanins to exosomes. *Journal of Cell Biology.* 2020;219. doi:10.1083/jcb.201904113
 83. Phuyal S, Hessvik NP, Skotland T, Sandvig K, Llorente A. Regulation of exosome release by glycosphingolipids and flotillins. *FEBS J.* 2014. doi:10.1111/febs.12775
 84. Mashouri L, Yousefi H, Aref AR, Ahadi AM, Molaei F, Alahari SK. Exosomes: composition, biogenesis, and mechanisms in cancer metastasis and drug resistance. *Molecular Cancer* 2019 18:1. 2019;18: 1–14. doi:10.1186/S12943-019-0991-5
 85. Kumar Thakur B, Zhang H, Becker A, Matei I, Huang Y, Costa-Silva B, et al. Double-stranded DNA in exosomes: a novel biomarker in cancer detection. *Nature Publishing Group.* 2014. doi:10.1038/cr.2014.44

-
86. Valadi H, Ekström K, Bossios A, Sjöstrand M, Lee JJ, Lötvall JO. Exosome-mediated transfer of mRNAs and microRNAs is a novel mechanism of genetic exchange between cells. *Nat Cell Biol.* 2007;9: 654–659. doi:10.1038/NCB1596
 87. Zhou J, Flores-Bellver M, Pan J, Benito-Martin A, Shi C, Onwumere O, et al. Human retinal organoids release extracellular vesicles that regulate gene expression in target human retinal progenitor cells. *Sci Rep.* 2021;11: 21128. doi:10.1038/s41598-021-00542-w
 88. Zhou J, Benito-Martin A, Mighty J, Chang L, Ghoroghi S, Wu H, et al. Retinal progenitor cells release extracellular vesicles containing developmental transcription factors, microRNA and membrane proteins. *Sci Rep.* 2018;8: 2823. doi:10.1038/s41598-018-20421-1
 89. Eastlake K, Lamb WDB, Luis J, Khaw PT, Jayaram H, Limb GA. Prospects for the application of Müller glia and their derivatives in retinal regenerative therapies. *Prog Retin Eye Res.* 2021;85. doi:10.1016/J.PRETEYERES.2021.100970
 90. Liu Y, Yang Q, Fu H, Wang J, Yuan S, Li X, et al. Müller glia-derived exosomal miR-9-3p promotes angiogenesis by restricting sphingosine-1-phosphate receptor S1P1 in diabetic retinopathy. *Mol Ther Nucleic Acids.* 2022;27: 491. doi:10.1016/J.OMTN.2021.12.019
 91. Demais V, Pohl A, Wunderlich KA, Pfaller AM, Kaplan L, Barthélémy A, et al. Release of VAMP5-positive extracellular vesicles by retinal Müller glia in vivo. *J Extracell Vesicles.* 2022;11. doi:10.1002/JEV2.12254
 92. Salinas RY, Pearing JN, Ding JD, Spencer WJ, Hao Y, Arshavsky VY. Photoreceptor discs form through peripherin-dependent suppression of ciliary ectosome release. *J Cell Biol.* 2017;216: 1489. doi:10.1083/JCB.201608081
 93. Molday RS, Goldberg AFX. Peripherin diverts ciliary ectosome release to photoreceptor disc morphogenesis. *J Cell Biol.* 2017;216: 1227. doi:10.1083/JCB.201703020
 94. Vidal-Gil L, Sancho-Pelluz J, Zrenner E, Oltra M, Sahaboglu A. Poly ADP ribosylation and extracellular vesicle activity in rod photoreceptor degeneration. *Sci Rep.* 2019;9: 1–10. doi:10.1038/s41598-019-40215-3
 95. Bunggulawa EJ, Wang W, Yin T, Wang N, Durkan C, Wang Y, et al. Recent advancements in the use of exosomes as drug delivery systems. *J Nanobiotechnology.* 2018;16: 1–13. doi:10.1186/S12951-018-0403-9/FIGURES/7
 96. Mead B, Berry M, Logan A, Scott RAH, Leadbeater W, Scheven BA. Stem cell treatment of degenerative eye disease. *Stem Cell Res.* 2015;14: 243. doi:10.1016/J.SCR.2015.02.003

-
97. Bian B, Zhao C, He X, Gong Y, Ren C, Ge L, et al. Exosomes derived from neural progenitor cells preserve photoreceptors during retinal degeneration by inactivating microglia; Exosomes derived from neural progenitor cells preserve photoreceptors during retinal degeneration by inactivating microglia. *The Journal of Extracellular Vesicles*. 2020. doi:10.1080/20013078.2020.1748931
 98. Wang Y, Zhang Q, Yang G, Wei Y, Li M, Du E, et al. RPE-derived exosomes rescue the photoreceptors during retina degeneration: an intraocular approach to deliver exosomes into the subretinal space. *Drug Deliv*. 2021;28: 218–228. doi:10.1080/10717544.2020.1870584
 99. György B, Fitzpatrick Z, Crommentuijn MHW, Mu D, Maguire CA. Naturally enveloped AAV vectors for shielding neutralizing antibodies and robust gene delivery in vivo. *Biomaterials*. 2014;35: 7598. doi:10.1016/J.BIOMATERIALS.2014.05.032
 100. Fitzpatrick Z, György B, Skog J, Maguire CA. Extracellular Vesicles as Enhancers of Virus Vector-Mediated Gene Delivery. *Hum Gene Ther*. 2014;25: 785. doi:10.1089/HUM.2014.082
 101. Maguire CA, Balaj L, Sivaraman S, Crommentuijn MHW, Ericsson M, Mincheva-Nilsson L, et al. Microvesicle-associated AAV Vector as a Novel Gene Delivery System. *Molecular Therapy*. 2012;20: 960–971. doi:10.1038/MT.2011.303
 102. Wassmer SJ, Carvalho LS, György B, Vandenberghe LH, Maguire CA. Exosome-associated AAV2 vector mediates robust gene delivery into the murine retina upon intravitreal injection. *Sci Rep*. 2017. doi:10.1038/srep45329
 103. Hudry E, Martin C, Gandhi S, György B, Scheffer DI, Mu D, et al. Exosome-associated AAV vector as a robust and convenient neuroscience tool HHS Public Access Author manuscript. *Gene Ther*. 2016;23: 380–392. doi:10.1038/gt.2016.11
 104. Kovács OT, Soltész-katona E, Marton N, Baricza E, Hunyady L, Turu G, et al. Impact of Medium-Sized Extracellular Vesicles on the Transduction Efficiency of Adeno-Associated Viruses in Neuronal and Primary Astrocyte Cell Cultures. *Int J Mol Sci*. 2021;22: 22. doi:10.3390/IJMS22084221
 105. van Niel G, Gazeau F, Wilhelm C, Silva AKA. Technological and translational challenges for extracellular vesicle in therapy and diagnosis. *Adv Drug Deliv Rev*. 2021;179: 114026. doi:10.1016/J.ADDR.2021.114026
 106. Keeler CE. The Inheritance of a Retinal Abnormality in White Mice. *Proc Natl Acad Sci U S A*. 1924;10: 329–333. doi:10.1073/pnas.10.7.329

-
107. Chang B, Hawes NL, Pardue MT, German AM, Hurd RE, Davisson MT, et al. Two mouse retinal degenerations caused by missense mutations in the β -subunit of rod cGMP phosphodiesterase gene. *Vision Res.* 2007;47: 624–633. doi:10.1016/J.VISRES.2006.11.020
 108. Chang B, Hawes NL, Hurd RE, Davisson MT, Nusinowitz S, Heckenlively JR. Retinal degeneration mutants in the mouse. *Vision Res.* 2002;42: 517–525. doi:10.1016/S0042-6989(01)00146-8
 109. Pennesi ME, Michaels K V., Magee SS, Maricle A, Davin SP, Garg AK, et al. Long-term characterization of retinal degeneration in rd1 and rd10 mice using spectral domain optical coherence tomography. *Invest Ophthalmol Vis Sci.* 2012;53: 4644–4656. doi:10.1167/iovs.12-9611
 110. Davis RJ, Hsu C-W, Tsai Y-T, Wert KJ, Sancho-Pelluz J, Lin C-S, et al. Neurobiology of Disease Therapeutic Margins in a Novel Preclinical Model of Retinitis Pigmentosa. *The Journal of Neuroscience.* 2013. doi:10.1523/JNEUROSCI.0419-13.2013
 111. Sauer B, Henderson N. Site-specific DNA recombination in mammalian cells by the Cre recombinase of bacteriophage P1. *Proc Natl Acad Sci U S A.* 1988;85: 5166. doi:10.1073/PNAS.85.14.5166
 112. Sternberg N, Sauer B, Hoess R, Abremski K. Bacteriophage P1 cre gene and its regulatory region: Evidence for multiple promoters and for regulation by DNA methylation. *J Mol Biol.* 1986;187: 197–212. doi:10.1016/0022-2836(86)90228-7
 113. Kim H, Kim M, Im S-K, Fang S. Mouse Cre-LoxP system: general principles to determine tissue-specific roles of target genes. *Lab Anim Res.* 2018;34: 147. doi:10.5625/LAR.2018.34.4.147
 114. Brocard J, Warot X, Wendling O, Messaddeq N, Vonesch JL, Chambon P, et al. Spatio-temporally controlled site-specific somatic mutagenesis in the mouse. *Proc Natl Acad Sci U S A.* 1997;94: 14559–14563. doi:10.1073/PNAS.94.26.14559
 115. Kistner A, Gossen M, Zimmermann F, Jurecic J, Ullmer C, Lübbert H, et al. Doxycycline-mediated quantitative and tissue-specific control of gene expression in transgenic mice. *Proc Natl Acad Sci U S A.* 1996;93: 10933–10938. doi:10.1073/PNAS.93.20.10933
 116. Marquardt T, Ashery-Padan R, Andrejewski N, Scardigli R, Guillemot F, Gruss P. Pax6 is required for the multipotent state of retinal progenitor cells. *Cell.* 2001;105: 43–55. doi:10.1016/S0092-8674(01)00295-1

-
117. Bäumer N, Marquardt T, Stoykova A, Ashery-Padan R, Chowdhury K, Gruss P. Pax6 is required for establishing naso-temporal and dorsal characteristics of the optic vesicle. *Development*. 2002;129: 4535–4545. doi:10.1242/dev.129.19.4535
 118. Kammandel B, Chowdhury K, Stoykova A, Aparicio S, Brenner S, Gruss P. Distinct cis-essential modules direct the time-space pattern of the Pax6 gene activity. *Dev Biol*. 1999;205: 79–97. doi:10.1006/DBIO.1998.9128
 119. Soriano P. Generalized lacZ expression with the ROSA26 Cre reporter strain . *Nat Genet*. 1999;21: 70–71. doi:10.1038/5007
 120. Muzumdar MD, Tasic B, Miyamichi K, Li N, Luo L. A global double-fluorescent cre reporter mouse. *Genesis*. 2007;45: 593–605. doi:10.1002/DVG.20335
 121. Prigge JR, Wiley JA, Talago EA, Young EM, Johns LL, Kundert JA, et al. Nuclear double-fluorescent reporter for in vivo and ex vivo analyses of biological transitions in mouse nuclei. *Mammalian Genome*. 2013;24: 389–399. doi:10.1007/s00335-013-9469-8
 122. Kajtna J, Tsang SH, Koch SF. Late-stage rescue of visually guided behavior in the context of a significantly remodeled retinitis pigmentosa mouse model. *Cell Mol Life Sci*. 2022;79: 148. doi:10.1007/s00018-022-04161-0
 123. Koch SF, Duong JK, Hsu CW, Tsai YT, Lin CS, Wahl-Schott CA, et al. Genetic rescue models refute nonautonomous rod cell death in retinitis pigmentosa. *Proc Natl Acad Sci U S A*. 2017;114: 5259–5264. doi:10.1073/pnas.1615394114
 124. Koch SF, Tsai YT, Duong JK, Wu WH, Hsu CW, Wu WP, et al. Halting progressive neurodegeneration in advanced retinitis pigmentosa. *Journal of Clinical Investigation*. 2015;125: 3704–3713. doi:10.1172/JCI82462
 125. Winkler BS. The electroretinogram of the isolated rat retina. *Vision Res*. 1972;12: 1183–1198. doi:10.1016/0042-6989(72)90106-X
 126. Chou JC, Rollins SD, Fawzi AA. Trypsin Digest Protocol to Analyze the Retinal Vasculature of a Mouse Model. *J Vis Exp*. 2013; 50489. doi:10.3791/50489
 127. Zudaire E, Gambardella L, Kurcz C, Vermeren S. A Computational Tool for Quantitative Analysis of Vascular Networks. *PLoS One*. 2011;6. doi:10.1371/JOURNAL.PONE.0027385
 128. Lamprecht MR, Sabatini DM, Carpenter AE. CellProfiler: free, versatile software for automated biological image analysis. *Biotechniques*. 2007;42: 71–75. doi:10.2144/000112257
 129. Tokuyasu KT. Immunocytochemistry on ultrathin frozen sections. *Histochem J*. 1980;12: 381–403. doi:10.1007/BF01011956/METRICS

-
130. Slot JW, Geuze HJ. Cryosectioning and immunolabeling. *Nat Protoc.* 2007;2: 2480–2491. doi:10.1038/nprot.2007.365
 131. Pinto LH, Invergo B, Shimomura K, Takahashi JS, Troy JB. Interpretation of the mouse electroretinogram. *Documenta Ophthalmologica.* 2007;115: 127–136. doi:10.1007/s10633-007-9064-y
 132. Tanimoto N, Sothilingam V, Kondo M, Biel M, Humphries P, Seeliger MW. Electroretinographic assessment of rod- and cone-mediated bipolar cell pathways using flicker stimuli in mice. *Sci Rep.* 2015;5: 1–7. doi:10.1038/srep10731
 133. Ruether K, Feigenspan A, Pirngruber J, Leitges M, Baehr W, Strauss O. PKC α is essential for the proper activation and termination of rod bipolar cell response. *Invest Ophthalmol Vis Sci.* 2010;51: 6051–6058. doi:10.1167/IOVS.09-4704
 134. Wässle H, Peichl L, Airaksinen MS, Meyer M. Calcium-binding proteins in the retina of a calbindin-null mutant mouse. *Cell Tissue Res.* 1998;292: 211–218. doi:10.1007/S004410051052/METRICS
 135. Puthussery T, Gayet-Primo J, Taylor WR. Localization of the Calcium-binding Protein Secretagogin in Cone Bipolar Cells of the Mammalian Retina. *J Comp Neurol.* 2010;518: 513–525. doi:10.1002/CNE.22234
 136. Brown WR. A Review of String Vessels or Collapsed, Empty Basement Membrane Tubes. *Journal of Alzheimer's Disease.* 2010;21: 725–739. doi:10.3233/JAD-2010-100219
 137. Kemler R. From cadherins to catenins: cytoplasmic protein interactions and regulation of cell adhesion. *Trends in Genetics.* 1993;9: 317–321. doi:10.1016/0168-9525(93)90250-L
 138. Bodenstein L, Sidman RL. Growth and development of the mouse retinal pigment epithelium. I. Cell and tissue morphometrics and topography of mitotic activity. *Dev Biol.* 1987;121: 192–204. doi:10.1016/0012-1606(87)90152-7
 139. Joshi BS, de Beer MA, Giepmans BNG, Zuhorn IS. Endocytosis of Extracellular Vesicles and Release of Their Cargo from Endosomes. *ACS Nano.* 2020;14: 4444–4455. doi:10.1021/acsnano.9b10033
 140. Jones K, Nourse JP, Keane C, Bhatnagar A, Gandhi MK. Plasma microRNA are disease response biomarkers in classical hodgkin lymphoma. *Clinical Cancer Research.* 2014;20: 253–264. doi:10.1158/1078-0432.CCR-13-1024
 141. Tan E, Ding XQ, Saadi A, Agarwal N, Naash MI, Al-Ubaidi MR. Expression of Cone-Photoreceptor-Specific Antigens in a Cell Line Derived from Retinal Tumors in Transgenic Mice. *Invest Ophthalmol Vis Sci.* 2004;45: 764–768. doi:10.1167/IOVS.03-1114

142. Gallego C, Gonçalves MAFV, Wijnholds J. Novel Therapeutic Approaches for the Treatment of Retinal Degenerative Diseases: Focus on CRISPR/Cas-Based Gene Editing. *Front Neurosci.* 2020;14. doi:10.3389/FNINS.2020.00838
143. Lin B, Masland RH, Strettoi E. Remodeling of cone photoreceptor cells after rod degeneration in rd mice. *Exp Eye Res.* 2009;88: 589. doi:10.1016/J.EXER.2008.11.022
144. Obien MEJ, Deligkaris K, Bullmann T, Bakkum DJ, Frey U. Revealing neuronal function through microelectrode array recordings. *Front Neurosci.* 2015;9: 423. doi:10.3389/fnins.2014.00423
145. Wang F, Flanagan J, Su N, Wang LC, Bui S, Nielson A, et al. RNAscope: A Novel in Situ RNA Analysis Platform for Formalin-Fixed, Paraffin-Embedded Tissues. *J Mol Diagn.* 2012;14: 22. doi:10.1016/J.JMOLDX.2011.08.002
146. Remez LA, Onishi A, Menuchin-Lasowski Y, Biran A, Blackshaw S, Wahlin KJ, et al. Pax6 is essential for the generation of late-born retinal neurons and for inhibition of photoreceptor-fate during late stages of retinogenesis. *Dev Biol.* 2017;432: 140. doi:10.1016/J.YDBIO.2017.09.030
147. Becher B, Waisman A, Lu LF. Conditional Gene-Targeting in Mice: Problems and Solutions. *Immunity.* 2018;48: 835. doi:10.1016/J.IMMUNI.2018.05.002
148. Liu H, Tang J, Du Y, Saadane A, Tonade D, Samuels I, et al. Photoreceptor Cells Influence Retinal Vascular Degeneration in Mouse Models of Retinal Degeneration and Diabetes. *Invest Ophthalmol Vis Sci.* 2016;57: 4272–4281. doi:10.1167/IOVS.16-19415
149. Jentzsch MC, Tsang SH, Koch SF. A new preclinical model of retinitis pigmentosa due to Pde6g deficiency. *Ophthalmology Science.* 2023;0: 100332. doi:10.1016/J.XOPS.2023.100332
150. De Gooyer TE, Stevenson KA, Humphries P, Simpson DAC, Curtis TM, Gardiner TA, et al. Rod Photoreceptor Loss in Rho^{-/-} Mice Reduces Retinal Hypoxia and Hypoxia-Regulated Gene Expression. *Invest Ophthalmol Vis Sci.* 2006;47: 5553–5560. doi:10.1167/IOVS.06-0646
151. Matthes MT, Bok D. Blood vascular abnormalities in the degenerative mouse retina (C57BL/6J-rd le). *Invest Ophthalmol Vis Sci.* 1984;25: 364–369.
152. García-Ayuso D, Di Pierdomenico J, Vidal-Sanz M, Villegas-Pérez MP. Retinal Ganglion Cell Death as a Late Remodeling Effect of Photoreceptor Degeneration. *Int J Mol Sci.* 2019;20: 4649. doi:10.3390/IJMS20184649
153. Gupta N, Brown KE, Milam AH. Activated microglia in human retinitis pigmentosa, late-onset retinal degeneration, and age-related macular degeneration. *Exp Eye Res.* 2003;76: 463–471. doi:10.1016/S0014-4835(02)00332-9

-
154. Zhao L, Zabel MK, Wang X, Ma W, Shah P, Fariss RN, et al. Microglial phagocytosis of living photoreceptors contributes to inherited retinal degeneration. *EMBO Mol Med.* 2015;7: 1179–1197. doi:10.15252/EMMM.201505298
 155. Mitra S, Devi S, Lee MS, Jui J, Sahu A, Goldman D. Vegf signaling between Müller glia and vascular endothelial cells is regulated by immune cells and stimulates retina regeneration. *Proc Natl Acad Sci U S A.* 2022;119. doi:10.1073/pnas.2211690119
 156. Froger N, Matonti F, Roubex C, Forster V, Ivkovic I, Brunel N, et al. VEGF is an autocrine/paracrine neuroprotective factor for injured retinal ganglion neurons. *Sci Rep.* 2020;10: 1–11. doi:10.1038/s41598-020-68488-z
 157. Scott A, Powner MB, Gandhi P, Clarkin C, Gutmann DH, Johnson RS, et al. Astrocyte-Derived Vascular Endothelial Growth Factor Stabilizes Vessels in the Developing Retinal Vasculature. *PLoS One.* 2010;5. doi:10.1371/journal.pone.0011863
 158. Ding X, Gu R, Zhang M, Ren H, Shu Q, Xu G, et al. Microglia enhanced the angiogenesis, migration and proliferation of co-cultured RMECs. *BMC Ophthalmol.* 2018;18. doi:10.1186/S12886-018-0886-Z
 159. Dejana E, Tournier-Lasserre E, Weinstein BM. The Control of Vascular Integrity by Endothelial Cell Junctions: Molecular Basis and Pathological Implications. *Dev Cell.* 2009;16: 209–221. doi:10.1016/J.DEVCEL.2009.01.004
 160. Chavakis E, Dimmeler S. Regulation of Endothelial Cell Survival and Apoptosis During Angiogenesis. *Arterioscler Thromb Vasc Biol.* 2002;22: 887–893. doi:10.1161/01.ATV.0000017728.55907.A9
 161. Marmor MF, Ravin JG. Fluorescein angiography: insight and serendipity a half century ago. *Arch Ophthalmol.* 2011;129: 943–948. doi:10.1001/ARCHOPHTHALMOL.2011.160
 162. Datta S, Cano M, Ebrahimi K, Wang L, Handa JT. The Impact of Oxidative Stress and Inflammation on RPE Degeneration in Non-neovascular AMD. *Prog Retin Eye Res.* 2017;60: 201. doi:10.1016/J.PRETEYERES.2017.03.002
 163. Napoli D, Biagioni M, Billeri F, Marco B Di, Orsini N, Novelli E, et al. Retinal pigment epithelium remodeling in mouse models of retinitis pigmentosa. *Int J Mol Sci.* 2021;22. doi:10.3390/IJMS22105381/S1
 164. Jiménez AJ, García-Fernández JM, González B, Foster RG. The spatio-temporal pattern of photoreceptor degeneration in the aged rd/rd mouse retina. *Cell Tissue Res.* 1996;284: 193–202. doi:10.1007/S004410050579/METRICS

165. Radeke MJ, Radeke CM, Shih YH, Hu J, Bok D, Johnson L V., et al. Restoration of mesenchymal retinal pigmented epithelial cells by TGF β pathway inhibitors: implications for age-related macular degeneration. *Genome Med.* 2015;7. doi:10.1186/S13073-015-0183-X
166. Tamiya S, Kaplan HJ. Role of epithelial–mesenchymal transition in proliferative vitreoretinopathy. *Exp Eye Res.* 2016;142: 26–31. doi:10.1016/J.EXER.2015.02.008
167. Saika S, Yamanaka O, Okada Y, Tanaka S-I, Miyamoto T, Sumioka T, et al. TGF beta in fibroproliferative diseases in the eye. *Frontiers in Bioscience-Scholar.* 2009;1: 376–390. doi:10.2741/S32
168. Zhou M, Geathers JS, Grillo SL, Weber SR, Wang W, Zhao Y, et al. Role of Epithelial-Mesenchymal Transition in Retinal Pigment Epithelium Dysfunction. *Front Cell Dev Biol.* 2020;8: 501. doi:10.3389/fcell.2020.00501
169. Han JW, Lyu J, Park YJ, Jang SY, Park TK. Wnt/ β -Catenin Signaling Mediates Regeneration of Retinal Pigment Epithelium After Laser Photocoagulation in Mouse Eye. *Invest Ophthalmol Vis Sci.* 2015;56: 8314–8324. doi:10.1167/IOVS.15-18359
170. Chen M, Rajapakse D, Fraczek M, Luo C, Forrester J V., Xu H. Retinal pigment epithelial cell multinucleation in the aging eye - a mechanism to repair damage and maintain homeostasis. *Aging Cell.* 2016;15: 436–445. doi:10.1111/accel.12447
171. Zarbin MA. Current Concepts in the Pathogenesis of Age-Related Macular Degeneration. *Archives of Ophthalmology.* 2004;122: 598–614. doi:10.1001/ARCHOPHT.122.4.598
172. R. Sparrow J, Hicks D, P. Hamel C. The Retinal Pigment Epithelium in Health and Disease. *Curr Mol Med.* 2010;10: 802. doi:10.2174/156652410793937813
173. Raimondi R, Zollet P, De Rosa FP, Tsoutsanis P, Stravalaci M, Paulis M, et al. Where Are We with RPE Replacement Therapy? A Translational Review from the Ophthalmologist Perspective. *Int J Mol Sci.* 2022;23: 682. doi:10.3390/IJMS23020682
174. Chen C, Cano M, Wang JJ, Li J, Huang C, Yu Q, et al. Role of Unfolded Protein Response Dysregulation in Oxidative Injury of Retinal Pigment Epithelial Cells. *Antioxid Redox Signal.* 2014;20: 2091. doi:10.1089/ARS.2013.5240
175. Intartaglia D, Giamundo G, Conte I. Autophagy in the retinal pigment epithelium: a new vision and future challenges. *FEBS J.* 2022;289: 7199. doi:10.1111/FEBS.16018
176. Mazzoni F, Mao Y, Finnemann SC. Advanced Analysis of Photoreceptor Outer Segment Phagocytosis by RPE Cells in Culture. *Methods Mol Biol.* 2019;1834: 95. doi:10.1007/978-1-4939-8669-9_7
177. Sidhom K, Obi PO, Saleem A. A Review of Exosomal Isolation Methods: Is Size Exclusion Chromatography the Best Option? *Int J Mol Sci.* 2020. doi:10.3390/ijms21186466

-
178. Malkin EZ, Bratman S V. Bioactive DNA from extracellular vesicles and particles. *Cell Death Dis.* 2020;11: 1–13. doi:10.1038/s41419-020-02803-4
 179. Elzanowska J, Semira C, Costa-Silva B. DNA in extracellular vesicles: biological and clinical aspects. *Mol Oncol.* 2020. doi:10.1002/1878-0261.12777
 180. Yokoi A, Villar-Prados A, Oliphint PA, Zhang J, Song X, De Hoff P, et al. Mechanisms of nuclear content loading to exosomes. *Sci Adv.* 2019;5. doi:10.1126/sciadv.aax8849
 181. Tsang SH, Gouras P, Yamashita CK, Kjeldbye H, Fisher J, Farber DB, et al. Retinal Degeneration in Mice Lacking the γ Subunit of the Rod cGMP Phosphodiesterase. *Science* (1979). 1996;272: 1026–1029. doi:10.1126/SCIENCE.272.5264.1026
 182. Müller B, Wagner F, Lorenz B, Stieger K. Organotypic Cultures of Adult Mouse Retina: Morphologic Changes and Gene Expression. *Invest Ophthalmol Vis Sci.* 2017;58: 1930–1940. doi:10.1167/IOVS.16-20718

7 Publication

Jentsch MC, Tsang SH, Koch SF. A new preclinical model of retinitis pigmentosa due to *Pde6g* deficiency. *Ophthalmology Science*. 2023;0: 100332. doi:10.1016/J.XOPS.2023.100332

8 Acknowledgements

First of all, I would like to express my sincere gratitude to my supervisor Prof. Susanne Koch for giving me the opportunity to learn and work on my PhD thesis in her laboratory. Her encouragement and guidance have been valuable in shaping my research. I am deeply grateful for her dedication and mentorship.

Additionally, I thank Prof. Martin Biel for accepting to be the second examiner of my PhD thesis and always giving me insightful feedback as well as constructive criticism, which have been instrumental in improving the quality of my work.

I also want to thank my dissertation committee for the critical evaluation of my thesis.

Particularly, I thank my research group colleagues Jacqueline, Moni, Felia, Hanaa, and Nundi for their great commitment and advice. All of you contributed to an enjoyable working atmosphere in the lab, which facilitated me to stay motivated and focused. I also want to thank Antje, Lew, Oli, Josef, and Anna for their help in the lab during my first year and their supportive feedback in our meetings. Further, I am very grateful to all the members from AK Biel for the close cooperation. Thank you all for your recommendations in the lab and for all the fun in between. It was a very pleasant time for me.

I also wish to thank all my friends who were always there for me, either close to me in Munich or from all over the country. Specifically, I would like to thank Kimia for our deep friendship, which has now lasted for almost 25 years, as well as Karo for our countless long voice messages and for sharing her contagious enthusiasm for plants with me.

Especially I thank my parents Carmen and Guido, my brother Daniel as well as my grandparents Doris, Klaus and Gisela for their continuous great encouragement and believing in me. Your support has sustained me through my whole journey and I could not have done this without you. The greatest gratitude belongs to my boyfriend German. Thank you for your endless love and for being my support in so many different ways. Your faith in me has been a constant source of inspiration and I am thankful for your patience during all the time I spent working on my thesis.